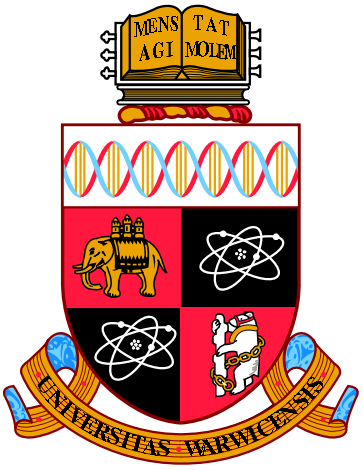

Electron Microscopy Study of Plastically Deformed Natural Brown Diamond and Surface Processing of Boron Doped Diamond Electrodes

by

Fraser Harrison James Laidlaw

Thesis

Submitted to the University of Warwick

for the degree of

Doctor of Philosophy

Department of Physics

July 2021

Contents

List of Tables

List of Figures

Acknowledgments

This thesis wouldn't be what it is without the help of a great number of people.

Firstly, I'd like to thank my supervisor Prof. Richard Beanland for his supervision, support and guidance throughout the project. Getting your head around dislocations is not easy and his insight here was invaluable.

My thanks also go to other academics in the microscopy group, Prof. Ana Sanchez, Dr. Jeremy Sloan and Prof. Neil Wilson for making the group an enjoyable place to work, and the electron microscopy RTP staff, Steve York, Steve Hindmarsh, Yisong Han and Houari Amari, for their help using the microscopes and fixing any problems I have encountered with them.

My thanks go to De Beers Technology UK, for financial and technical support, and providing interesting samples to work on. Special thanks to Dr. David Fisher and Dr. Phil Diggle for their support, feedback experimental suggestions, and sharing their knowledge of diamond. Phil has been extremely helpful in recent months in bettering my understanding of optical imaging and spectroscopic techniques, which I feel has added greatly to the thesis.

Thanks also go to all those involved in the Diamond Science and Technology CDT. The DST Masters year was a brilliant foundation from which to do the PhD. It also provided the opportunity to meet and work alongside some great people, and on a variety of interesting projects, and for that I am thankful. Sam Cobb and Georgia Wood are thanked for teaching me some of the basics of electrochemistry.

My thanks go to the members of the Warwick Microscopy group past and present, especially James, Jon, Charlie, Natalie and Abi, and DST cohort 3, namely Bruno, Dan, Georgia, Luke, Jack and Jamie, for help, support, encouragement and

coffee/drinks.

Finally, I am grateful to my Mum, Dad and sister, Gillian, for their love and support over the last four years.

Declarations

I declare that this thesis contains an account of my research work carried out at the Department of Physics, University of Warwick, between October 2017 and February 2021 under the supervision of Prof. Richard Beanland. The research reported here has not been previously submitted, wholly or in part, at this or any other academic institution for admission to a higher degree. Some parts of the work reported and other work not reported in this thesis have been published, as listed below.

Published papers

- F.H.J. Laidlaw, R. Beanland, D. Fisher, P.L. Diggle, *"Point defects and interstitial climb of 90° partial dislocations in brown type IIa natural diamond"*, *Acta Materialia*, 201 (2020) 494 - 503

- S.J. Cobb, F.H.J. Laidlaw, G. West, G. Wood, M.E. Newton, R. Beanland, J.V. Macpherson, *Assessment of acid and thermal oxidation treatments for removing sp^2 bonded carbon from the surface of boron doped diamond*, *Carbon*, 167 (2020) 1 - 10

Papers in preparation

- F.H.J. Laidlaw, R. Beanland, B.G. Breeze, M.W. Dale, P.L. Diggle, D. Fisher, *"Spatial distribution of defects in a plastically deformed natural brown diamond"*

All of the work presented here was completed by the author with the exception of:

- Collection of PL and Raman map data in Chapter 5 was acquired by B.G. Breeze.
- Fitting of the Raman datasets in Chapter 5 was carried out by P.L. Diggle
- Electrochemistry and white light interferometry, and associated analysis, in Chapter 6 was carried out by S.J. Cobb.

Abstract

Plastic deformation of diamond can be seen as a naturally occurring event, often resulting in broad spectral absorption bands that give rise to either a pink or brown colour to the crystal. In this thesis, the effect of plastic deformation on the dislocation and point defect micro-structures in brown type IIa diamond is investigated by electron and optical microscopy techniques. In addition to investigating plastic deformation processes in natural brown diamond, TEM was also utilised to investigate the surface of boron-doped diamond (BDD) after various surface processing stages.

Firstly, the generation and behaviour of intrinsic point defects during plastic deformation is investigated. Vacancy clusters are considered to be the origin of the brown colouration in diamond and it is thought that vacancies generated during the plastic deformation aggregate together into the vacancy clusters. Interestingly, rather than finding direct evidence of vacancy generation, it is found that a large concentration of interstitials are generated, in addition to the vacancies, during plastic deformation. These interstitials condense onto the 90° partial dislocations leaving an excess of vacancies behind to cluster. Estimates of the interstitial concentrations generated are similar to vacancy concentrations measured in similar brown type IIa diamond, suggesting equal numbers of interstitials and vacancies are generated by plastic deformation. Atomically resolved Z-type faulted dipoles, also showing interstitial absorption, have been imaged allowing the stacking fault energy of diamond to be calculated, with a value of 472 mJm^{-2} $\pm$ 38 mJm^{-2} being determined.

The effect of plastic deformation, on the distribution of point defects and dislocation microstructure, is then investigated using correlative electron and optical microscopy techniques. The type IIa diamond observed here shows alternating brown and colourless banding, allowing the differences between pristine and deformed material to be examined. Brown bands show dislocation structures that clearly indicate intrinsic point defect generation has occurred while PL and Raman mapping showing increased concentrations of point defects and stresses associated with plastic deformation within the brown bands.

Lastly, utilising the techniques developed during this PhD work, the results of a collaboration, using electrochemistry and electron microscopy to characterise the surface of boron-doped diamond (BDD) after various surface treatments coverage are presented. For use as an elctrode material, the ability to control the surface

sp^2 content of the electrodes is necessary, and both electrochemistry and electron microscopy were used to assess the sp^2 content at after each processing stage. Laser ablation of the surface was used to generate sp^2 on the surface, while the effectiveness of acid and thermal oxidation treatments for removing sp^2 carbon was investigated. Laser ablation of the surface forms a layer of highly ordered graphite immediately adjacent to the diamond which is topped by a layer of amorphous carbon, caused by the redeposition of sublimated carbon. Acid treatment removes the majority of the graphite and amorphous carbon layer leaving behind clusters of graphite with basal planes perpendicular to the surface, encapsulated with a thin amorphous layer. These graphite clusters are robust enough to survive any subsequent acid treatments. Finally, thermal oxidation treatment was able to remove all clusters leaving behind a surface with very low sp^2 coverage. Characterisation of the surface treatments gives confidence that consistent and reliable BDD electrodes can be manufactured and tailored for specific applications.

Chapter 1

Introduction

Diamond has been valued for its extreme mechanical and optical properties for millenia, since its first discovery in India. The hardness of diamond appears to have been apparent for thousands of years, where it may have been used for drilling in the lapidary arts. Beads found in Yemen, originating from the 5 - 7th century BC, provide the earliest evidence of diamond being used for drilling [1], with score marks on the drilled walls being consistent with the use of diamond. Although evidence of diamond drills being used by the Indus valley civilisation in western India [2,3] only dates back to the 1st century BC, trade routes passed through Yemen, connecting India, Africa and the Mediterranean [1], suggesting either diamond or beads were being traded as far back as the 5 - 7 th century BC.

As well as its hardness, the unique optical properties of diamond first made it a symbol of power and status, before it became the symbol of love it is known for now. According to the Garuda Purana, an ancient Sanskrit book dating back to the 4 - 5th century AD, diamonds distinctive "sparkle", which was described as the diamond having a "fire" [4,5], gave it almost mystical powers: "A diamond scintillating with flashes of rainbow colored hues at the center ... blesses its wearer with a prosperous family and well-filled granaries. A king wearing a diamond dazzling with lightning flashes, is sure to subdue the prowess of his neighbouring monarchs and to exercise an unbounded control upon his vassals and liege subjects" [4,5].

As far back as the 4 - 5th century, and possibly earlier, it appears that the value of diamonds were established by judging on the "shape, colour, defects and excellence" of each stone [4]. Nowadays, the value of diamond is established by roughly the same criteria - called the 4Cs of diamond: colour, clarity, cut and carat weight [6]. Of these 4Cs, the colour is likely to be one of the biggest factors that gives a particular diamond its desirability, which can have a large effect on the

value of the stone. In recent years, the price of diamonds with rare colourations have achieved record values at auction, with price per carat far exceeding that of colourless stones[7–9].

Colouration in diamond can be enhanced by the use of various treatments, increasing the value of the stones. To maintain consumer confidence in the diamond market, diamond graders must be able to differentiate between naturally coloured diamond and natural diamond which has been treated in a laboratory setting to produce a particular colouration. As the colour of diamond is derived by the defects within the lattice and the optical absorption they give rise to, the behaviour of these defects need to be well understood when subjected to a treatment (for example by high pressure, high temperature (HPHT) annealing) so that methods for detecting treated stones can be developed. There are still aspects of the colouration in diamond that are not well understood. Plastic deformation has been attributed to the brown, pink, purple and red colourations in diamond[10–14], of which brown is the most commonly attributed colouration. Plastic deformation can produce a variety of effects on the crystal structure, type of point defect present and their distribution. The motivation behind this work is to better understand some of the processes occurring to the diamond microstructure during the plastic deformation process. This understanding can assist in determining the origin of various point defects and deformation induced colouration.

1.1 Colouration of Diamond

Pure diamond, containing no impurities, is an indirect band gap semiconductor with a wide band gap energy of 5.5 eV[15,16], the energy gap between the top of the valence band and bottom of the conduction band, Figure 1.1. This large band gap makes diamond transparent over the entire range of the visible wavelength spectrum, 380 - 700nm, giving rise to diamonds well-known colourless appearance. Yet defects in the diamond lattice and the presence of impurities can allow the diamond to exhibit a wide range of colours across the visible spectrum[9–11,17,18].

Colour can be introduced into the diamond by the presence of defects and impurities. These defects produce energy levels within the large band gap leading to the emission or absorption of certain wavelengths depending on the position of the energy levels within the band gap. For example, nitrogen is the most common impurity in diamond; found as a single impurity atom (C-centre) it introduces a defect state 1.7 eV below the conduction band resulting in a sharp absorption continuum extending from approx. 560 nm towards shorter wavelengths (bluer wave-

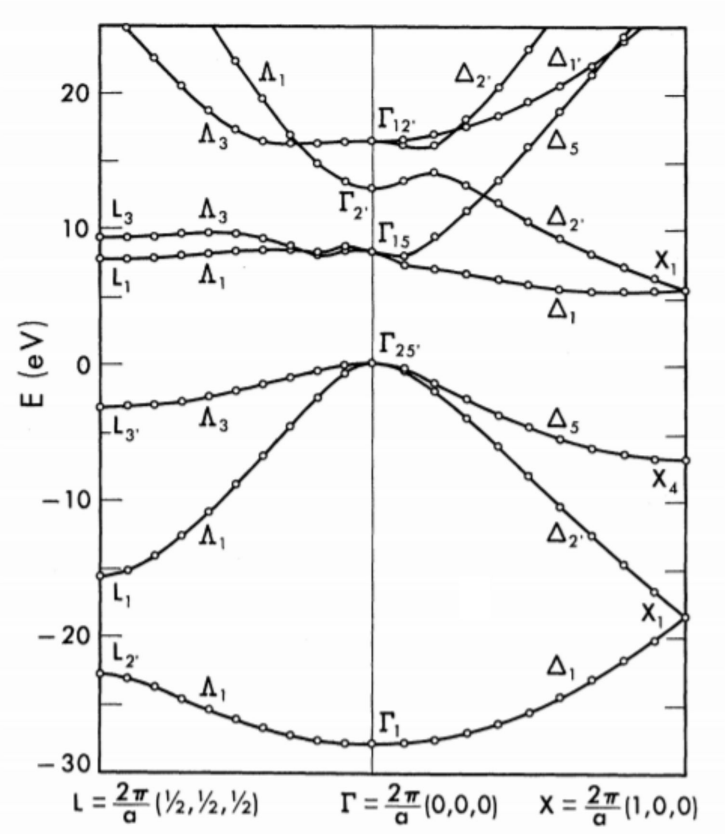

Figure 1.1: Band Structure of Diamond. Indirect band gap corresponds to $\Gamma_{25'}$ to Δ_1 transition. Image from Saslow et al. (1966) [15]

lengths) [19–21], Figure 1.2. This absorption of bluer wavelengths typically causes the diamond to have a strong yellow colouration, although the colour can changed depending on where the absorption continuum begins, Figure 1.2.

The neutral vacancy centre (also known as the GR1 centre) is commonly associated with green colouration in diamond. The GR1 centre produces an absorption band stretching from 550 - 750 nm causing the absorption of redder wavelengths [17]. This green colour only appears to be produced if the diamond contains a significant quantity of nitrogen, which is often the case in natural diamonds, which leads to the additional absorption of bluer wavelengths. In diamond lacking significant nitrogen content, the GR1 centre can give the diamond a blue colour [9]. The GR1 centre can be produced by irradiation naturally in the mantle, from alpha, beta and gamma radiation [17], or in a laboratory, using electrons or neutrons [22].

Boron is a common impurity added to chemical vapour deposition (CVD) diamond to make diamond electrically conductive, for possible use in electronic

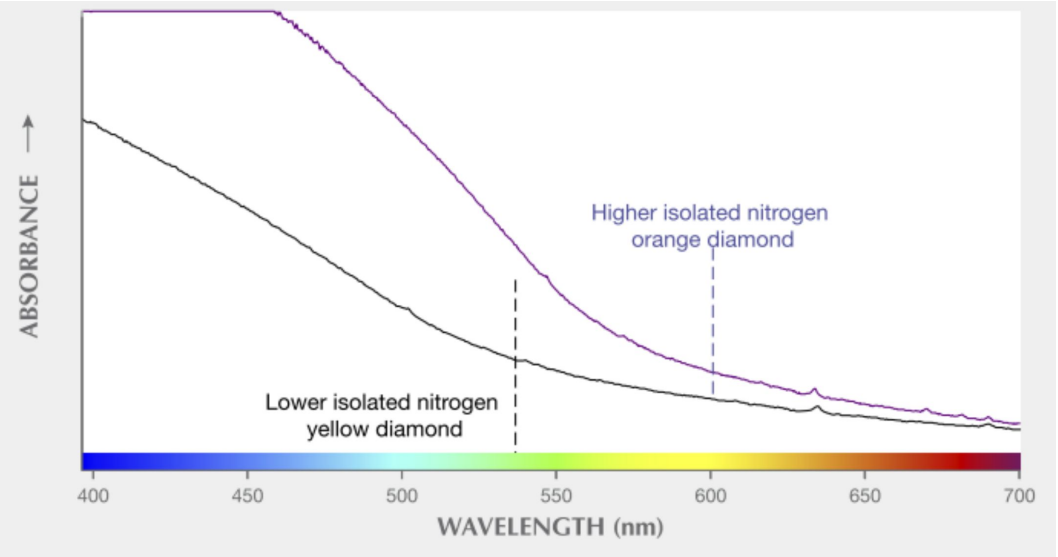

Figure 1.2: Absorption spectra of type Ib diamond containing different concentrations of single isolated nitrogen atoms. The edge of the absorption continuum dictates the colouration produced, as seen by the dashed vertical lines. Different concentrations of the single isolated nitrogen atoms can generate yellow or orange color. Image from Breeding et al. (2020) [21]

devices [16] or in electrochemical applications [23]. Boron introduces an energy level into the diamond 0.37 eV above the valence band and imparts a blue colouration to the diamond [9]. Boron can also be naturally incorporated into the diamond lattice, through various geological process, however naturally blue diamonds are one of the rarest types [9].

In addition to simple singular point defects, several point defects can aggregate to form point-defect complexes, which can also produce colouration. As an example, the well-known nitrogen-vacancy (NV) centre can produce a pink/red colouration [10,24]. Hundreds of electronic optical centres have been discovered in diamond and each can contribute in some way to colouration [25]. The vast majority of natural diamonds will contain several types of defect, some of which can contribute to the colouration, leading to a wide range of different possible hues.

Impurities can be introduced into diamond during growth, either from the melt material in which the diamond is located in the mantle, or from their presence in the precursor materials/gases in the case of high pressure high temperature (HPHT) and CVD synthetic diamond. In natural diamond, over the course of billions of years and at large temperatures of the mantle, this nitrogen can migrate forming larger

nitrogen complexes. Most natural diamonds will contain large nitrogen point defect complexes, such as the H3 centre (N-V-N), N3 centre (N_3V) and B-centre (N_4V). In HPHT and CVD synthetic diamond, the shorter time-scales over which growth occurs means that the nitrogen tends to be found as isolated centres (C-centre) rather than the larger nitrogen complexes seen in natural diamond. Similarly, other impurities, such as boron and silicon, can also be incorporated into the diamond by similar means.

1.1.1 Diamond Treatments

Treatments are available to enhance or remove particular colourations in diamond. The two most commonly used treatments are electron irradiation and HPHT treatment [22]. Irradiation of diamond can be carried out by neutron bombardment or high-energy electron irradiation [22]. Collisions knock carbon atoms out of their lattice position, generating both interstitials and vacancies in the diamond. This type of treatment usually causes a blue-to-green colouration, due to the presence of neutral vacancies, GR1 centre, but intense irradiations can cause graphitisation of the diamond producing a black colouration. Irradiation is typically followed by HPHT treatment causing the interstitials and vacancies to migrate and combine with any nitrogen impurities that may be present. Depending on the type of nitrogen defects initially present in the diamond, this can change the colour from blue-green to lighter colours, such as yellow, orange, pink, red, etc [22].

HPHT treatment alone can also be used to change the colour of diamond by changing the aggregation state of nitrogen in the untreated stones [22]. Depending on the initial defects present in the diamond and HPHT conditions used, treatment can be used to remove or enhance colouration, creating fancy colour diamond [22]. For example, the strong yellow colouration of type Ib diamond (see Section 1.6), containing predominantly C-centres, can be removed after HPHT treatment by causing the nitrogen to aggregate into large nitrogen containing complexes, which don't produce the absorption responsible for the yellow colouration. The brown colouration in diamond can be removed by HPHT treatments turning the diamond colourless or pink/blue (in some type II diamonds) or yellow/ yellow-green/orangey-yellow in type I diamond [22,26]. The brown colouration is discussed in more detail in Section 1.2.

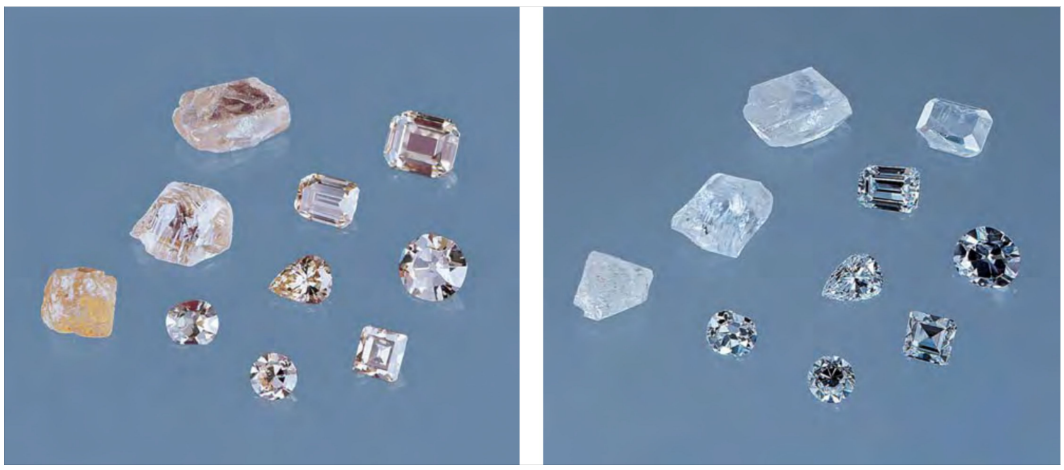

Figure 1.3: Example of 10 brown diamonds before HPHT treatment (left) and after HPHT treatment (right). After treatment all diamonds had their colour improved. Image from Smith et al. (2000) [27].

1.2 Brown Colouration in Diamond

The brown colouration of diamond has been the subject of much investigation over the past few decades [18,26,28–36]. About 98% of all mined diamonds worldwide contain some brown component [37], which has typically been seen as a less desirable colouration leading to reduced values for these stones. The main driving force behind the investigation into the origin of the brown colour came after the commercialisation of a HPHT treatment by Lazare Kaplin International, co-developed with General Electric, to remove the brown colouration, thereby increasing the value of the stone [22,26,27]. Methods to detect natural brown-to-colourless treated diamonds were required in order to maintain consumer confidence in the gemmological industry.

The brown colouration is caused by a gradually increasing absorption coefficient towards shorter (bluer) wavelengths. The gradual change in absorption coefficient and lack of any sharp absorption features indicated that an extended defect was responsible for the colouration [26,29]. Additionally, the brown colour is observed in both type I (nitrogen containing) and type II (no or low nitrogen content), see section 1.6, indicating that nitrogen plays no part in the colouration - the defect is intrinsic to diamond. Since all brown diamonds are found to be plastically deformed, dislocations were considered as an early candidate for the origin of the brown colour [26,29]. However even in the early stages of research, there were indications that put the dislocation theory in doubt. For example, although all brown

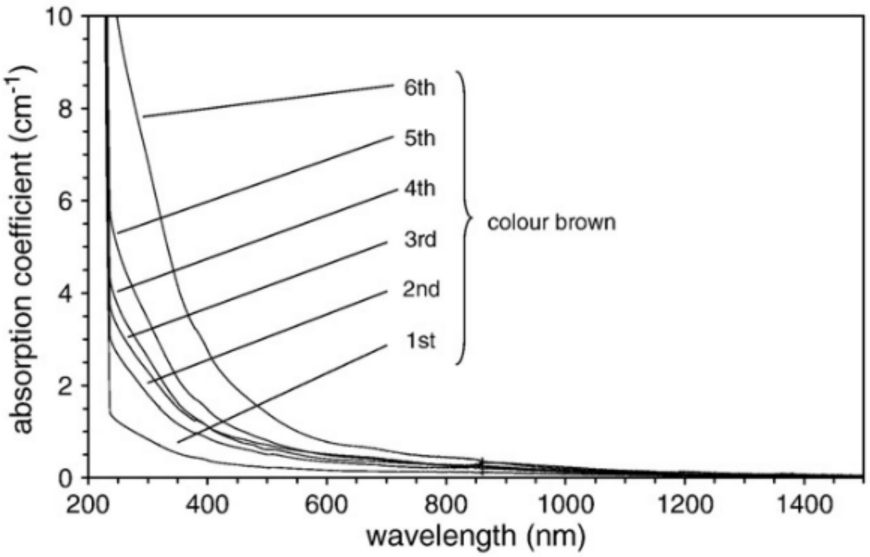

Figure 1.4: Absorption spectra of different colour grades of type IIa brown diamond, ranging from lightest brown grade (1^{st}) to darkest brown grade (6^{th}). Image from Fisher et al. (2006) [38].

diamonds are plastically deformed, not all plastically deformed diamonds are brown.

Density functional theory (DFT) studies into the structure of dislocations in diamond found that the most stable, and therefore most common, dislocation is the optically inactive 60° glide dislocation, see Section 2.2.3. While the 60° shuffle dislocation is optically active and can produce absorption features, it only produces a narrow band of states in the band gap and not the broad continuum of states that would be consistent with the absorption seen in brown diamond [29,39]. Additionally, in the unlikely case that every dislocation is of the higher energy shuffle type, the dislocation densities measured (10^9 cm^{-3}) [31] are also too low to account for the absorption observed in brown diamonds [26,29]. The DFT studies into the brown colouration were also backed-up by TEM imaging of the dislocations in naturally brown and post-treatment brown-turned-colourless diamond, which found no significant change in the dislocation distribution or dislocation line densities [18,31], suggesting that the dislocations were not responsible and the changes which removed the brown colouration were occurring on a smaller length scale.

Positron annihilation spectroscopy (PAS) has detected the presence of vacancy clusters in brown diamond, which are not seen in colourless diamond, and that anneal out with the colouration [30,36]. Positron lifetimes of 115 - 132 ps and 420 ± 20 ps were measured in brown diamond, which refer to a monovacancy type defect and vacancy cluster respectively [36]. Estimates of the vacancy cluster size

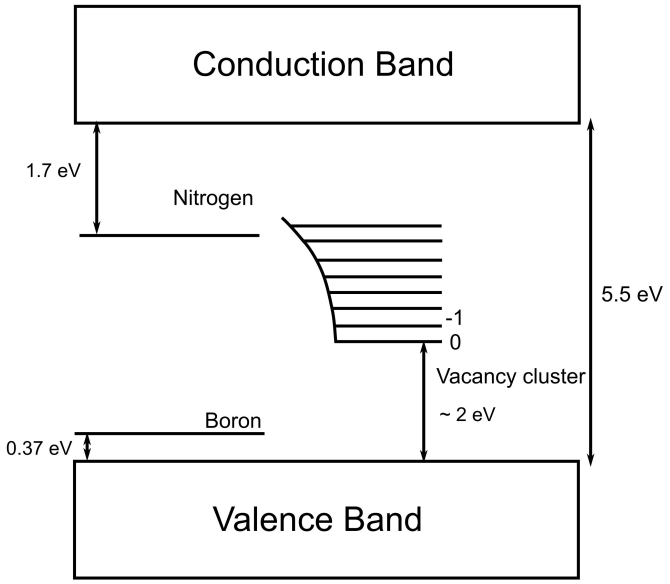

Figure 1.5: Schematic diagram showing the band structure of the vacancy clusters. The continuum of bands introduced by the vacancy clusters is approx 2 eV above the valence band. The vacancy cluster becomes negatively charged under illumination. Bands introduced by single nitrogen and boron atoms also shown. Not to scale. Based on Godfrey (2013) [32] and Maki et al. (2012) [36]

from PAS, puts the clusters at 30 - 60 vacancies in size with a roughly spherical shape [34]. DFT modelling indicates that vacancy clusters of this size do produce absorption that is well matched with that seen in brown diamond. Reconstruction of the carbon atoms on the inner surface of the vacancy clusters form π-bonded carbon atoms, introducing a continuum of states into the band gap of the diamond, and leading to the absorption seen in brown diamond [26,29,40]. PAS carried out under optical excitation shows that the vacancy clusters are optically active, being of neutral charge in the dark and becoming negatively charged under illumination, due to photo-excitation of electrons from the valence band to the vacancy clusters [34–36]. The concentration of vacancy clusters and monovacancy type defects are estimated at approx. 10^{15} cm^{-3} and 10^{18} cm^{-3} in type IIa brown diamond respectively [30,35]. Using high defocus conditions, high resolution transmission electron microscopy (HRTEM or HREM) and STEM was able to find features in brown diamond, not visible in colourless diamond, that matched the expected size of the vacancy clusters, indicating they could be imaged in the TEM [32,41,42]. Electron Energy Loss Spectroscopy (EELS) measured an increase in sp^2 carbon in brown diamond consistent with π-bonds on the inner surface of vacancy clusters [43,44]. This sp^2 signal was not present in HPHT treated brown or colourless diamond [43,44].

Although not directly responsible for the brown colouration, the dislocations are thought to play a secondary role in the colouration by generating vacancies during plastic deformation, which then aggregate into the vacancy clusters. The movement of jogged dislocations or annihilation of dislocation dipoles are two such ways in which point defects can be generated during the plastic deformation.

Plastic deformation has also been linked to the pink, purple and violet colourations observed in diamond [12–14]. Although the origin of the pink colouration is still not known, it has been attributed to twinning and is closely linked with the brown colour. The pink colour in diamond is caused by the 550 nm and 390 nm absorption bands. Pink diamond exhibits photochromism, changing colour from pink to brown after intense UV excitation and reverting back to pink after an anneal at 800 °C [45]. Charge transfer between the "pink" defect and other defects may be the cause of the photochromism in pink diamond, with vacancy clusters likely being one of these defects [46–48]. Absorption spectra of purple and violet colourations appear to share similarities to both brown and pink colourations, which could suggest the presence of both vacancy clusters and the "pink" colour centre, although, the exact origin is equally as undetermined as the pink/brown centres.

1.3 Geology of Diamond

Natural diamonds are thought to be formed within the peridotitic and eclogitic rocks that make up the Earth's upper mantle, where the high pressures and temperatures lie within the diamonds stability field [49]. Most diamonds are grown at depths of 150 - 250 km, where pressures of 40 - 60 kbar and temperatures between 900 - 1400°C are achieved [49,50]. Diamond growth occurs over the course of billions of years, with radiometric ageing putting the age of peridotitic diamond at 3 - 3.3 billion years and eclogitic diamond at 0.9 - 1.6 billion years old [49]. The majority of diamonds are mined from kimberlite pipes located within cratons. Cratons are old sections of the crust, which are relatively unchanged for billions of years. The crust is thicker at the cratons with a "keel" that extends deeper into the upper mantle than surrounding areas [50]. The keel extends below the depth at which the diamond-graphite transition occurs allowing the diamond containing mantle to be sampled by the kimberlite upon eruption [50].

From the depths of the mantle, the diamonds are carried rapidly to the surface embedded in volcanic rocks called kimberlites, during a kimberlite eruption. Studies of inclusions found within diamond show that the diamonds form long before their emplacement in the mantle by the kimberlite. The kimberlite plays no part in

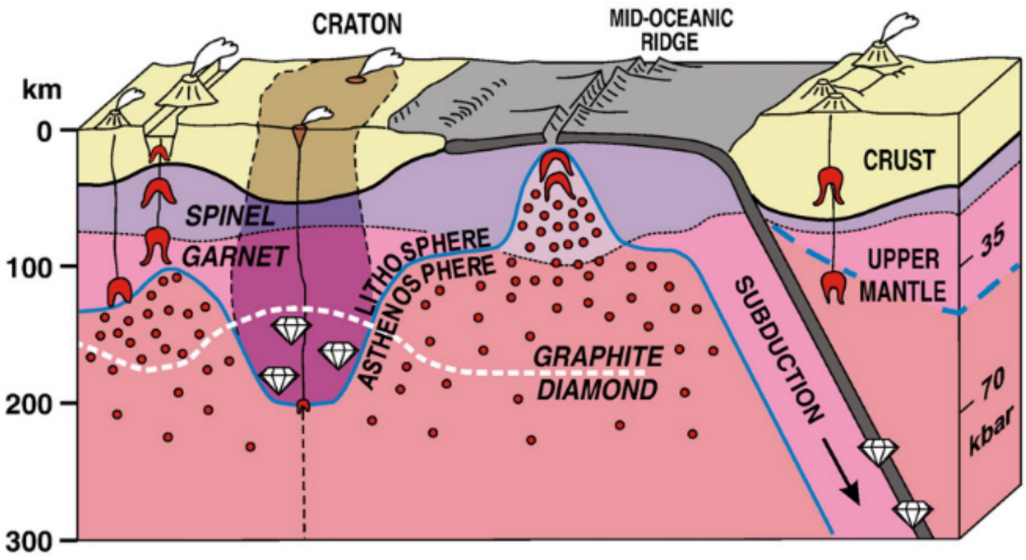

Figure 1.6: Schematic of Earth's crust. The craton is highlighted by the dark shaded region, the crust is thicker at cratons, extending deeper into the mantle. Lower temperatures located in the subcratonic lithosphere raises the depth of the diamond stability field, allowing the keel of the craton to sample material from the diamond stability field [50]. Diamonds can also be located at extreme depths due to subduction of the mantle - superdeep diamonds. Image from Stachel and Harris [50]

the crystallisation and growth of the diamond [50], only taking a role in the transport of the diamond to the surface. The reason for kimberlites being the most common source of diamond is two-fold. Kimberlite magmas originate from deep in the mantle, $>$ 150 km [51], and erupts violently and rapidly to the surface over durations of several hours to months [52]. This rapid eruption and cooling prevents graphitisation of the diamond, since conditions are no longer in the diamond stability field, or its dissolution in the magma [51]. Kimberlite eruptions are extremely violent events, due to the large amount of volatile materials, such as CO_2 or water, contained within the kimberlite [51–54]. As the kimberlite magma approaches the surface, the pressure decrease causes these volatile gases to degas from the magma, leading to increased magma velocities [52,54]. The kimberlite magmas are thought to flow in a turbulent manner with rise velocities of between 4 - 20 ms^{-1} [52], although velocities as high as 50 ms^{-1} have been estimated [54].

There is evidence to suggest that plastic deformation occurs late in the diamonds history [55]. The billions of years that diamond sits in the mantle, means that even at lower temperatures the brown colouration might be expected to anneal

out. It is during the rapid ascent to the surface, in a kimberlite eruption, that impacts between the rising kimberlite and surrounding rock are believed to exert shear stresses on the diamond, resulting in plastic deformation of the diamond and producing the brown colouration [26].

The theory that the brown colouration is a late stage event in the diamonds history is up for debate though. The temperatures and pressures in the upper mantle are also suitable for the plastic deformation of diamond, and the brown colouration could be formed earlier in the diamonds history than previously thought [56]. Despite the lower pressures and temperatures of the mantle, compared to lab-based HPHT treatments, it was thought that any brown colour formed earlier in the diamonds history would be annealed out over the millions of years that the diamond is in the mantle. Smith et al. (2010) have found that at temperature below 1000°C, brown colouration can survive in the mantle for up to 10^8 years [56].

1.4 Plastic Deformation of Diamond

For significant ductile deformation of diamond to take place, temperatures > 900°C are generally required [57], although temperatures as low as 750°C can be achieved with the use of soft indenters [58] and some deformation has been reported at room temperatures [59]. Confining pressures, in combination with high temperatures, can inhibit the brittle fracture of diamond [57]. DeVries (1975) [57] found diamond could be plastically deformed at temperatures as low as 900 - 1100°C over pressures ranging from 10 - 60 kbar (1 - 6 GPa), conditions easily achievable at the depths diamond is grown at in the mantle, Section 1.3. DeVries (1975) found no difference in the deformation conditions required for type I and II diamond, however Evans (1965) found that platelets in type I diamond were efficient barriers to deformation and higher stresses were generally required to deform type I diamond compared to type II [60]. Platelets are interstitial aggregations, typically found in type I diamond (see Section 1.6), which lie on {100} planes with typical dimensions of a few μm [61]. Their structure has been under investigation for decades and has only recently been determined using atomic resolution scanning transmission electron microscopy (STEM) [62].

The most obvious sign plastic deformation has occurred is the observation of slip lines oriented on {111} planes, along with brown colouration. Brown colouration has been induced in diamond by deforming under HPHT conditions, and can also result in the formation of twins [63].

1.5 Crystallography of Diamond

Diamond is a metastable allotrope of carbon with a face-centred cubic (fcc) unit cell and two atom basis, at (0,0,0) and $(\frac{1}{4}, \frac{1}{4}, \frac{1}{4})$. The unit cell of diamond has space group $Fd\bar{3}m$ and a lattice parameter of 3.56Å, with 8 atoms per unit cell. The unstrained carbon-carbon bond length is 1.541Å. The unit cell of diamond can be seen in Figure 1.7.

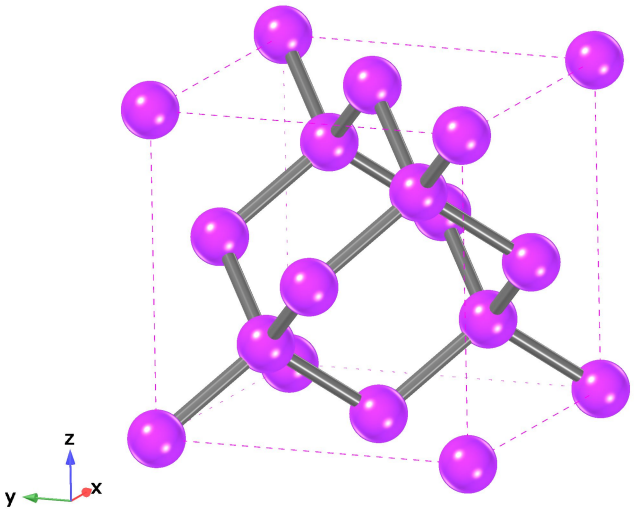

Figure 1.7: Diamond unit cell showing the tetrahedral bonding configuration.

The exceptional properties of diamond are a result of the strength of carbon-carbon bonds and the tetrahedral bonding arrangement.

When carrying out atomic resolution imaging of materials in transmission electron microscopy (TEM) or scanning TEM, microscopists tend to look down low index crystal zone axes. The atomic structure of diamond viewed down the ⟨100⟩, ⟨110⟩ and ⟨111⟩ zone axis and associated diffraction patterns are shown below in Figure 1.8. The {004}, {220} and {111} planes are shown in the diffraction patterns and trace onto the crystal structure.

Dislocations in diamond lie on {111} planes and often have line directions along ⟨110⟩ or ⟨112⟩ directions. To view the atomic structure of dislocation cores, the diamond is prepared to be viewed looking along a ⟨110⟩ zone axis. Dislocations in diamond are discussed in more detail in Section 2.2. Viewed down the ⟨110⟩ zone axis, the carbon 'dumbbell' structure can be seen. The carbon "dumbbell"

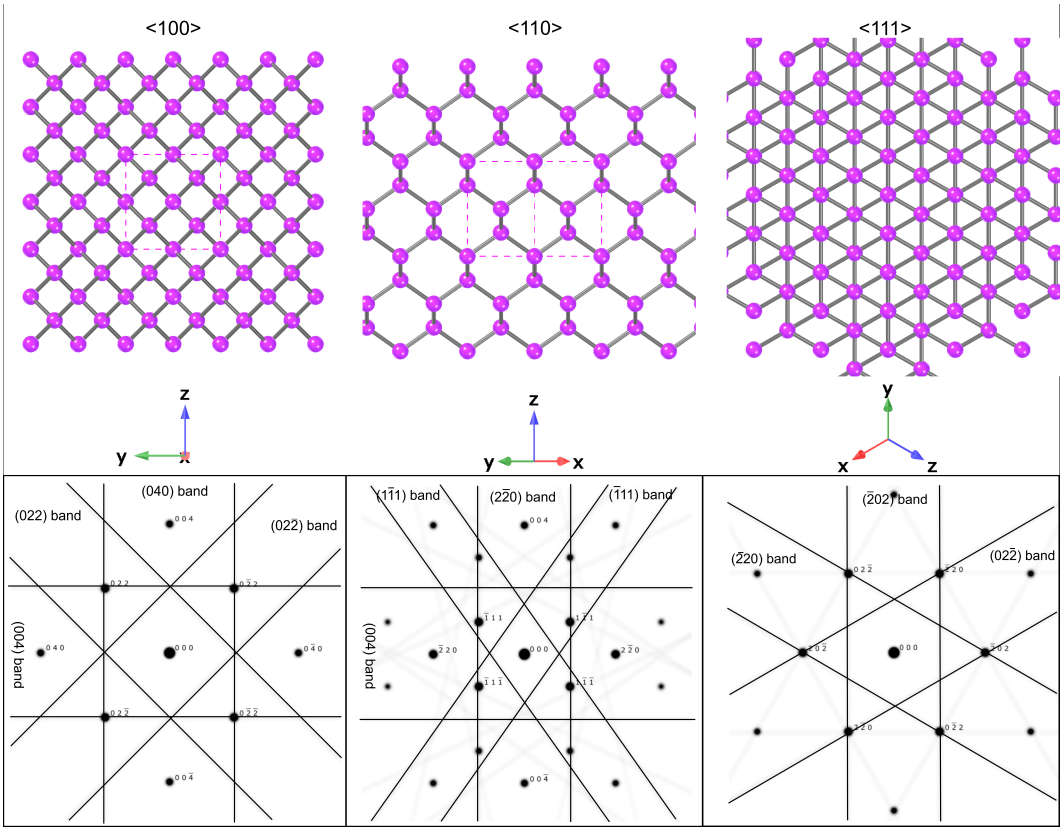

Figure 1.8: Diamond viewed along different directions. The diffraction pattern and low index Kikuchi bands are shown below.

is the name given to the two carbon atoms that appear very close together, when viewed down the $\langle 110 \rangle$ zone axis, for its resemblance to a dumbbell. The appearance of the dumbbells is due to the projection of the three-dimensional structure of the diamond lattice onto a two-dimensional plane. In Figure 1.8 (middle), the dumbbells are lined up along a $\langle 100 \rangle$ direction. The carbon atoms in the dumbbell appear to be separated by 89 pm, so aberration-corrected STEM is required in order to resolve these atoms separately.

1.6 Types of Diamond

Diamond can be classified into different categories depending on the concentration and type of defects present in the diamond. The diamond "type" is dependent on the concentration of nitrogen within the diamond detected using FTIR spectroscopy; type I diamond is that which contains detectable amounts of nitrogen (typically >

1 ppm) while type II diamond contains no or undetectable amounts of nitrogen (< 1 ppm). These types can then be further sub-categorised depending on the level of nitrogen aggregation that has occurred. The diamond classifications are summarised below.

- **Type I**: Type I diamonds are those which contain detectable quantities of nitrogen using FTIR spectroscopy. Typically concentrations are > 1 ppm of nitrogen. This category makes up a large fraction of all mined diamond. Type I can be sub-categorised further depending on the form the nitrogen impurities take:
  - **Type Ia**: Makes up 95% of all mined diamonds. Nitrogen is mainly found in aggregated form. Type Ia can be further sub-categories as:
    - **Type IaA**: Nitrogen is found largely in pairs (A - centres).
    - **Type IaB**: Nitrogen is found in larger aggregates, this can be in the form of B, H3 or N3 centres, etc.
  - **Type Ib**: Makes up less than 0.1% of mined diamonds. Nitrogen is found as isolated impurities (C - centres). This type of diamond is most common in CVD and HPHT grown diamond.
- **Type II**: No detectable nitrogen using FTIR spectroscopy. Nitrogen concentrations < 1 ppm. Type II further categorised:
  - **Type IIa**: No detectable nitrogen or boron impurities. Make up 1 - 2 % of all mined diamonds worldwide.
  - **Type IIb**: Significant quantities of boron impurities. Make up 0.1% of mined diamonds and are one of the rarest types of natural diamond.

These diamond types are only a rough guide to categorise diamonds based on their nitrogen content and aggregation state. Most natural diamonds are found to have the characteristics of several types. During growth nitrogen is thought to be incorporated as single atoms (C-centres), which over the years migrate and aggregate into larger nitrogen complexes (H3, N3, B-centres, etc). Different growth zones within natural diamond can be found with different aggregation states [64,65], while it has been suggested that plastic deformation events can disrupt nitrogen aggregation, reverting some areas to a lower aggregation state and generating single isolated nitrogen atoms [20,46].

1.7 Thesis Outline

In this thesis, the effect of plastic deformation on the dislocation microstructure and point defect distributions in type IIa brown natural diamond have been investigated using electron and optical microscopy techniques.

Chapter 2 reviews several point defects commonly seen in diamond, namely the interstitial, vacancy and some nitrogen vacancy complexes. This chapter also discusses relevant aspects of dislocation theory in fcc materials, which applies equally to diamond.

Chapter 3 will briefly discuss the many electron and optical microscopy techniques employed in the investigation of the diamond. Sample preparation techniques are also discussed.

Chapter 4 reviews how intrinsic point defects can be generated during plastic deformation, investigates the atomic structure of dislocations in plastically deformed diamond, and forms the link between the plastic deformation and the brown colouration in diamond.

Chapter 5 expands upon Chapter 4 by looking at a "zebra" diamond, containing both brown and colourless bands. Using both electron and optical microscopy techniques, the effect of the plastic deformation on the dislocation microstructure and the point defect distributions between the two bands is investigated.

Chapter 6 departs from the investigation of plastically deformed natural diamond and details the results of a collaboration with the Warwick Electrochemistry and Interface Group. Here, the surface of boron doped diamond (BDD) is investigated using the developed techniques in electron microscopy following different material processing stages for use within electrochemical applications.

Chapter 2

Point Defects in Natural Diamond and Dislocation Theory

To better understand some of the processes and results in later chapters it is necessary to review some of the defects that can be present in diamond. Defects in diamond (and materials in general) can be categorised as either intrinsic or extrinsic. Intrinsic defects are those that can be found in the pure material (in diamond these are interstitials, vacancies, dislocations, grain boundaries, stacking faults, twins, etc.) while extrinsic defects are those which contain impurities (nitrogen, boron, silicon, vacancy-impurity centres, etc.). A brief review of fundamental concepts relating to Burgers vectors and dislocations is also given, based on Hirth and Lothe *"Theory of Dislocations"* [66].

2.1 Point Defects in Diamond

2.1.1 The Carbon Interstitial and Vacancy

The carbon interstitial and vacancy in diamond have been extensively studied over the years, mainly via irradiation experiments and DFT modelling. Point defects can be generated easily by irradiation, creating Frenkel pairs (interstitial-vacancy pairs), and so most point defect studies are carried out in irradiated material using high energy electrons, neutrons or ions. Subsequent annealing of irradiated samples causes the migration of interstitials and vacancies, and their distribution can be measured in experiment. The migration properties of interstitials and vacancies, and the types of defect produced from their migration, have been studied in diamond

using experiments of this type[67].

The neutral vacancy centre (GR1), V^0, is commonly observed in irradiated diamond and can be identified by a zero phonon line (ZPL) in absorption and luminescence at 741.1 nm (1.673 eV)[38,68]. Uniaxial stress measurements on the GR1 centre shows the neutral vacancy exhibits tetrahedral (T_d) symmetry. DFT modelling of GR1 shows that neighbouring carbon atoms relax outwards[69,70], rather than inwards, forming a cube shaped volume of side 1.89Å[69]. The volume expansion caused by the vacancy is approximately 0.2 times the volume of a carbon atom in diamond[69]. This outwards relaxation differs from the relaxation seen in vacancies in silicon[71,72] and is due to the surrounding atoms trying to move into the {111} plane formed by nearest neighbours (NN) to form a more graphite-like sp^2 structure. DFT modelling for the formation energy, $E_v{}^f$, of the vacancy gives values of 6 - 7 eV[70,73]. Irradiation of diamond carried out at different temperatures finds the migration energy, $E_v{}^m$, of vacancies $\approx$ 2.3 eV[74]. Significant vacancy migration occurs at temperature over 600 °C. Negatively charged vacancies, V^-, can also be generated during irradiation of nitrogen rich diamond. The negative charge state of GR1 is known colloquially as ND1, where charge transfer is facilitated by nearby nitrogen donors, and identifiable by the ZPL at 393.7 nm[75,76]. Negatively charged vacancies are converted to neutrally charged vacancies before migrating, also with the same migration energy as the GR1 centre[77].

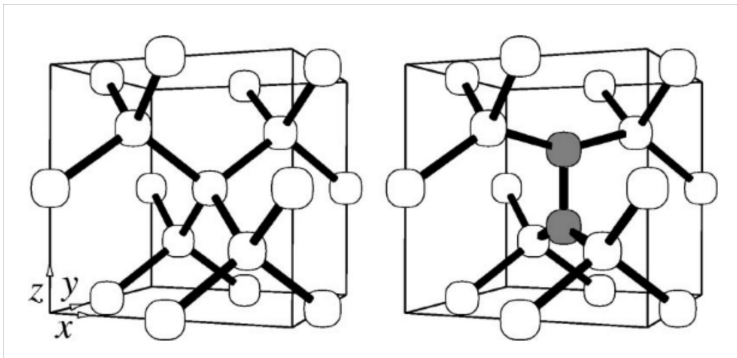

Figure 2.1: Schematic of a unit cell of perfect diamond material (left). T structure of the ⟨100⟩ split interstitial is shown (right). The interstitial is shown as darker atoms. Image from Goss et al. (2001)[78]

The R2 defect in irradiated diamond has been identified as a ⟨100⟩ split interstitial[79]. The structure of the ⟨100⟩ split interstitial has D_{2d} symmetry and can be seen in Figure 2.1. Computational modelling is in agreement and determines the split interstitial is the most stable configuration of a single interstitial in diamond[78,80]. The R2 defect has been attributed to optical transitions with ZPL

at 735.8 nm (1.68 eV) and 666.9 nm (1.859 eV)[81]. The 735.8 nm transition is a forbidden transition[81] and as such is a weak line. The formation energy of the interstitial in diamond is large, about double that of the vacancy at $E_i{}^f \approx 12$ eV[69,78]. The interstitial is far more mobile than the vacancy with a migration energy, $E_i{}^m \approx 1.6$ eV, with significant migration occurring at temperature $> 330°C$[81]. The volume change associated with the single interstitial in diamond is roughly 2 times the volume of a carbon atom in diamond[69].

2.1.2 Nitrogen Defect Complexes in Natural Diamond

As stated in Chapter 1, nitrogen is the dominant impurity in diamond and, even in highly pure type IIa diamond, it can be present in very small concentrations. Nitrogen in natural diamond is commonly seen in large defect aggregates, usually containing a mixture of nitrogen and vacancies. Commonly seen nitrogen complexes in natural diamond are the A and B centres as well as nitrogen-vacancy aggregates like the H3 and N3 centres. Three mechanisms have been proposed for the migration of nitrogen: direct interchange with neighbouring carbon atoms ($E_N{}^m \approx 6.3$ eV), as an interstitial atom ($E_{N_i}{}^m \approx 1$ eV), or via vacancy-assisted migration ($E_N{}^m \approx 4.5$ eV)[82]. Experimental evidence suggests the migration energy of nitrogen in diamond is ~ 5 eV[83]. The migration of nitrogen is therefore slower than interstitial and vacancy migration. Vacancies can be trapped at nitrogen atoms forming complexes such as the NV, H3, N3, A and B centres, so examining the distribution of these complexes can be useful for determining where vacancies are being generated and how they have migrated.

The H3 centre in diamond has structure N-V-N, Figure 2.2 (b), with a neutral charge. It can be identified in photoluminescence (PL) by a ZPL at 503.2 nm[25] and is often accompanied by the N3 centre. The H3 centre is thought to be formed by the capture of a vacancy at an A-centre (N-N), giving a structure of N-N-V before rearrangement of the atoms to the N-V-N structure[82]. The H3 centre has rhombic symmetry, C_{2v}[84]. The H3 centre can be formed by the irradiation of type I diamond followed by a subsequent anneal at over 500°C or in type II diamond by nitrogen implantation followed with by anneal above 800°C[25]. An increase in H3 centre concentration is also observed in areas of diamond that have undergone plastic deformation, surrounding indentation marks, at slip planes and around dislocation lines[85–87].

The N3 centre in diamond has a structure composed of three nitrogen atoms surrounding a vacancy (N_3V), Figure 2.2 (c). The N3 centre can be identified by a ZPL at 415.2 nm[25]. The N3 centre is common in natural diamond but can also be

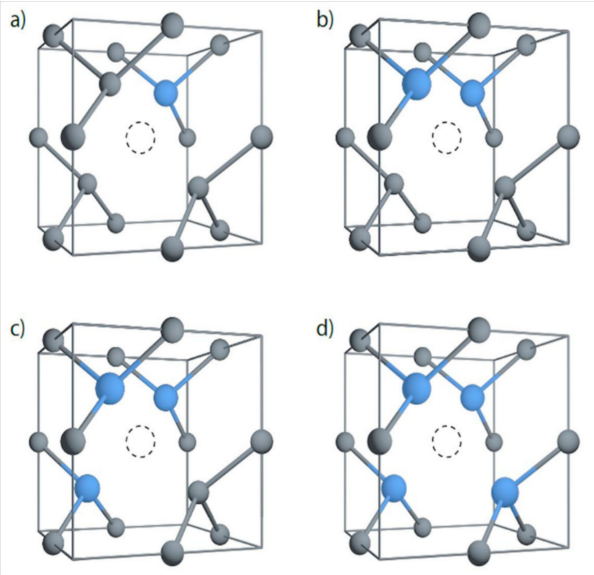

Figure 2.2: Atomic structure of the (a) Nitrogen Vacancy (NV) centre. (b) N_2V (H3) centre. (c) N_3V (N3) centre. (d) N_4V (B) centre. Image from Ashfold et al. (2020) [90]

produced in synthetic diamond following nitrogen implantation and annealing [25]. In natural diamond, the N3 centre has been found in {111} stacking faults [88], and can be found localised in regions of plastic deformation [89].

The B-centre is composed of a vacancy surrounded by 4 nitrogen atoms (N_4-V), Figure 2.2 (d). B-centres are identified using Fourier Transform Infrared (FTIR) spectroscopy by an absorption feature at 1175 cm^{-1} [25].

The exact mechanism behind the formation of the N3 and B centres are still not exactly known and several mechanisms have been proposed [90]. Kiflawi et al. (2000) [91] suggest the N3 centre is an intermediate step in the formation of the B-centre, caused by the capture of a C centre by an A-centre, with the production of an interstitial atom. Other mechanisms proposed are the capture of an N-V centre by an H3 centre, with the emission of a vacancy, or the capture of an NV centre by an A-centre [90].

The formation of the B-centre is thought to be caused by the break-up of A-centres into single substitutional nitrogen atoms which are then trapped at A-centres or N3 centres. Diamond containing the B-centre also tends to contain the B' centre (or {100} platelet) and the formation of the two defects may be linked [92,93]. The platelet is an aggregation of carbon interstitials, lying on a {100} plane [61,62,94,95]. Carbon interstitials are thought to be generated by the formation of the B-centre, allowing for the formation of the platelet.

A summary of the proposed mechanisms of nitrogen aggregation can be found in a review paper by Ashfold et al. (2020) [90].

2.2 Dislocations in Diamond

2.2.1 The Burgers Vector and Dislocation Types

Dislocations are 1-dimensional line defects of irregular crystal structure, most commonly associated with the plastic deformation of crystals. Dislocations are most easily described by their Burgers vector, line direction and the glide plane that they lie on. The Burgers vector is a vector which describes the lattice displacement caused by the presence of the dislocation line. In general, there are three types of dislocation possible: edge, screw and mixed type. An edge dislocation is one in which the Burgers vector is perpendicular to the line direction, screw where the Burgers vector is parallel to the line direction and mixed, where the Burgers vector has both parallel and perpendicular components of the Burgers vector to the line direction [66]. Schematic diagrams of edge and screw type dislocations in a simple cubic lattice are shown in Figure 2.3.

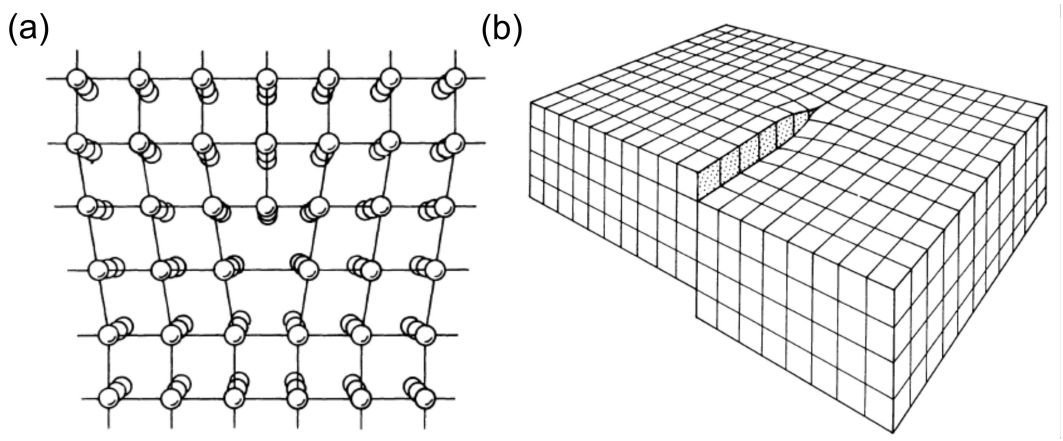

Figure 2.3: Schematic diagrams of an (a) edge dislocation and (b) a screw dislocation in a simple cubic lattice [66].

The Burgers vector can be calculated by comparing a vector circuit around the dislocation with the equivalent circuit in perfect material, Figure 2.4 [66]. Using the Finish-Start Right Hand convention (FS-RH), a circuit is drawn around a dislocation that is in "good" crystal, far from the core of the dislocation. An equivalent circuit is then drawn in a perfect lattice and the vector which closes the circuit in

the perfect crystal is the Burgers vector of the dislocation.

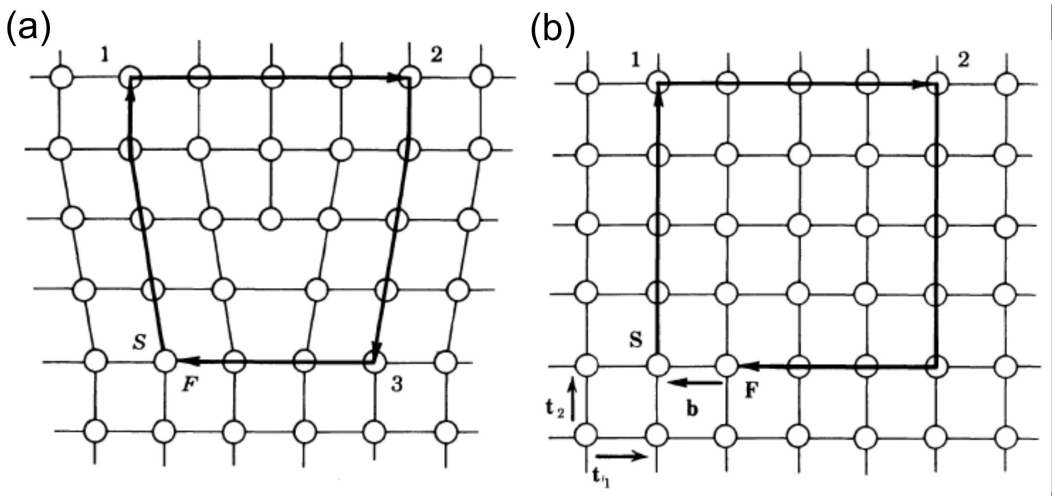

Figure 2.4: (a) Burgers circuit drawn around an edge dislocation in a simple cubic structure, circuit drawn in a clockwise direction. (b) Equivalent circuit drawn in a perfect cubic structure. The Burgers vector is the vector which closes the circuit going from the Finish to the Start [66].

Perfect dislocations in diamond are of the $\{111\}\langle 110\rangle$ type, meaning they lie on $\{111\}$ glide planes and have Burgers vector along $\langle 110\rangle$ directions [66,96]. The Burgers vector of these dislocations is $\frac{1}{2}\langle 110\rangle$, which is the smallest possible perfect dislocation Burgers vector. The low energy line directions are also $\langle 110\rangle$, which correspond to valleys in the lattice potential in the Peierls-Nabarro model. The Peierls-Nabarro model describes the effect of lattice periodicity on the atomic configuration of dislocations. The Peierls-Nabarro model will not be discused in detail here but more information can be found in Hirth and Lothe *"Theory of Dislocations"* [66]. These $\{111\}\langle 110\rangle$ dislocations are mixed type dislocations, with the Burgers vector making an angle of 60° to the line direction, and are commonly called 60° (perfect) dislocations. The glide plane is usually the most closely packed crystal plane. These planes are those with the largest spacing d, given by the equation:

$$d = \frac{a_0}{\sqrt{h^2 + k^2 + l^2}} \tag{2.1}$$

where h, k and l are the usual Miller indices. For fcc materials the closest packed planes are the $\{111\}$ planes, with a d spacing of $\frac{a_0}{\sqrt{3}}$.

Perfect dislocations can dissociate into partial dislocations if the energy of the dissociated configuration is lower in energy than the perfect dislocation. The

line energy of a dislocation is proportional to the square of the Burgers vector [66], b^2. It is possible for a perfect dislocation with Burgers vector, b_1, to dissociate into 2 partial dislocations, b_2 and b_3, if it satisfies Frank's energy criterion [66]:

$$b_1^2 > b_2^2 + b_3^2 \tag{2.2}$$

Additionally, the sum of the Burgers vector of the dissociation products must add up to the original Burgers vector:

$$b_1 = b_2 + b_3 \tag{2.3}$$

The partial dislocations produced by the dissociation of a dislocation are separated by an intrinsic stacking fault. The separation distance of the two partials is dependent on the stacking fault energy. As the separation distance of the partials increases the energy of the stacking fault increases, putting a limit to how far these partials can be separated [66]. The partials formed by the dissociation of a perfect dislocation are Shockley partial dislocations. Shockley partials have Burgers vector of the form $\frac{a}{6}\langle 112\rangle$ and lie on the same glide plane as the original dislocation, meaning they are glissile. In diamond, the two most common Shockley partial dislocations are the 30° and 90° partials, with Burgers vector forming an angle of 30° and 90° to the dislocation line direction respectively. In diamond, the 60° and screw dislocations can dissociate by the following reactions:

$$60^\circ\ dislocation \rightarrow 30^\circ\ partial + 90^\circ\ partial + ISF \tag{2.4}$$

$$[110]\ screw \rightarrow 30^\circ\ partial + 30^\circ\ partial + ISF \tag{2.5}$$

where ISF is an intrinsic stacking fault. Schematics of the dissociation can be seen in Figure 2.5, alongside a STEM image of a dissociated screw dislocation in diamond. The stacking fault energy of materials can be determined by measuring the separation width of a dissociated dislocation. In diamond, Pirouz et al. [97] measured the separation width of 30° and 90° partials to be between 2.5 - 4.3 nm, giving a stacking fault energy for diamond of 279 ± 41 mJ m^{-2}.

There are several other types of partial dislocation possible in fcc materials, including the Frank partial and the stair-rod (or Lomer-Cotrell) partial.

A Frank partial is formed by the insertion or removal of a layer of atoms on a {111} plane. The dislocation bounding the inserted or removed material is a Frank partial. Frank partials have Burgers vector of the form $\frac{a}{3}\langle 111\rangle$ that is directed out

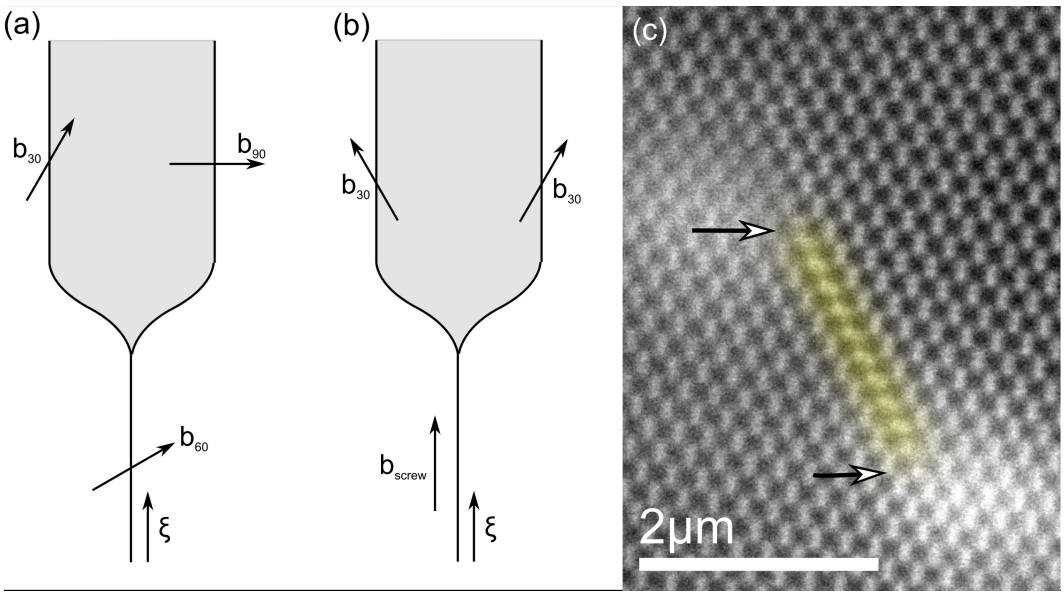

Figure 2.5: (a) Schematic of a dissociated 60° perfect dislocation into a 30° and 90° partial dislocation connect by an ISF. (b) Schematic of a dissociated screw dislocation into two 30° partial dislocations connected by an ISF. ISF shown by shaded grey region. 60° 30° and 90° Burgers vectors are denoted by the vectors $\mathbf{b_{60}}, \mathbf{b_{30}}, \mathbf{b_{90}}$ respectively. Line direction denoted by the vector ξ. Image based on Hirth and Loethe[66]. (c) Dissociated screw dislocation in diamond viewed along the line direction. Intrinsic stacking fault highlight by yellow shading. 30° partial dislocations located by the arrows at either end of the stacking fault. Separation width is approx. 2.33 nm.

of the glide plane. Frank partials are sessile (immobile to glide), but can move by the diffusion of atoms. Frank loops can grow or shrink by the absorption or emission of point defects. Frank partials tend to be higher energy partials and are able to dissociate further[66].

Another type of partial dislocation is a stair-rod (or Lomer-Cotrell) partial dislocation[66]. Stair-rod dislocations have Burgers vector of $\frac{a}{6}\langle 110\rangle$ type. They are formed by the intersection of two dissociated dislocations that lie on different glide planes. Stair-rod dislocations have Burgers vector that lie out of the glide plane and, as such, are completely immobile. Stair-rod partial dislocations can lead to significant work hardening of a material[66]. Stair-rod partial dislocations in diamond are shown in chapter 4.

2.2.2 Thompson's Tetrahedron

Thompson's tetrahedron is a useful notation to easily visualise the possible Burgers vectors and line directions for perfect and partial dislocations[66], Figure 2.6. The tetrahedron is composed of the 4 {111} glide planes, denoted by the triangles with vertices ABD, ABC, ADC and BCD, and the edges of the tetrahedron are aligned along the ⟨110⟩ directions. The vertices of the tetrahedron are denoted by the letters A, B, C and D, while the midpoint of the opposite face is denoted by α, β, γ, and δ.

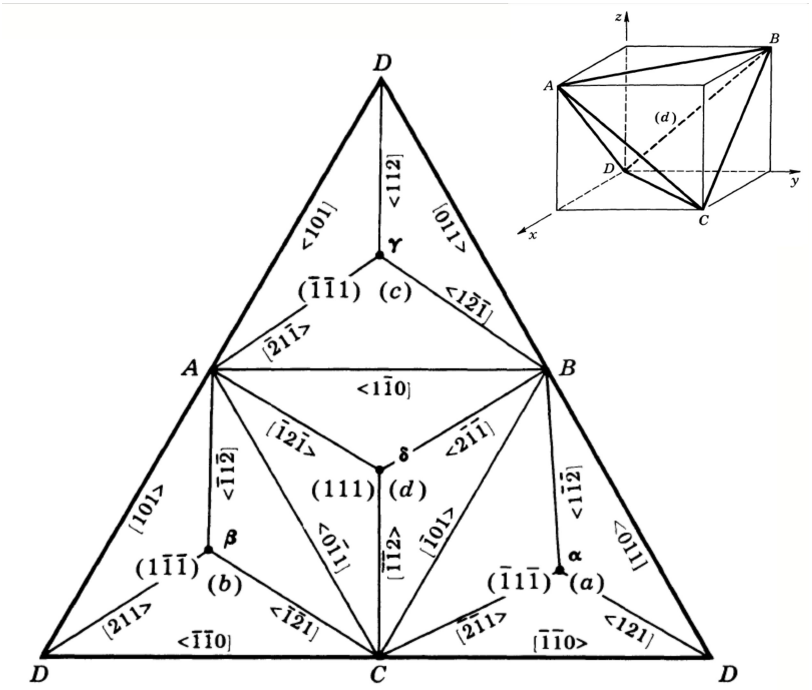

Figure 2.6: Thompson tetrahedron for dislocations in an fcc crystal, tetrahedron has been unfolded at the vertex D. Image from Hirth and Loethe[66].

⟨110⟩ line directions and Burgers vectors are given by the edges of the tetrahedron, described by the vectors denoted with Roman-Roman characters (AB, BC, CD, etc.). Shockley partial dislocations are described by the vectors denoted by Roman-Greek characters that lie on the same glide plane ($A\delta$, $A\beta$, $B\delta$, $B\alpha$, $C\alpha$, $D\beta$ etc.). Frank partial dislocations are described by the vectors of Roman-Greek character that lie between a vertex and the opposite glide plane ($A\alpha$, $B\beta$, $C\gamma$, $D\delta$). Stair-rod partial dislocations are given by Greek-Greek vectors between two glide planes ($\delta\beta$, $\delta\gamma$, $\delta\alpha$, $\alpha\gamma$, $\alpha\beta$, $\beta\gamma$). Dislocation reactions can be more easily visualised using Thompson's tetrahedron, for example, the dissociation of a dislocation AB

can be denoted by:

$$AB = A\delta + \delta B \ (on\ the\ (111)\ slip\ plane)$$
$$AB = A\gamma + \gamma B \ (on\ the\ (\bar{1}\bar{1}1)\ slip\ plane)$$

2.2.3 Atomic Structure of Dislocations in Diamond

Due to the two atom basis of the diamond structure, the dislocations with the same Burgers vector can have two different configurations, the glide and shuffle set, depending on the termination of the extra half plane. The cores of perfect and partial dislocations in diamond have been extensively modelled using DFT [96]. The atomic structure of the screw, glide and shuffle perfect 60° dislocation, and glide 30° and 90° partial dislocations are shown in Figure 2.7.

As can be seen from Figure 2.7, the core structure differs greatly between the glide and shuffle set 60° dislocation which leads to different properties of the dislocation. Bond reconstruction occurs in the core of the glide 60° dislocation so that all atoms are fully bonded. The terminating atoms reconstruct to bond along the dislocation line leading to a double periodic structure, Figure 2.7 b. In the 60° glide dislocation no dangling bonds are present, and the dislocation is optically inactive. Bond reconstruction doesn't occur in the shuffle 60° dislocation with the terminating atoms being sp^2 bonded, the extra dangling bond is directed into the dislocation core. The effect of this dangling bond is to introduce energy levels into the diamond band gap, making the shuffle set optically active. The shuffle 60° dislocation is found to be higher in energy than the 60° glide dislocation, and therefore the glide type dislocations are likely to be favoured in diamond [96].

DFT modelling also predicts that dislocation dissociation is favoured over perfect dislocations [96]. Both the dissociation of the 60° glide dislocation into a 30° and 90° partial, and the screw into two 30° partials are found to be favoured. The core structures of the 30° and 90° partial dislocations have also been modelled, Figure 2.7 (d, e, f). Similar to silicon, the 90° partial dislocation has been found to reconstruct in two possible configurations, a single-periodic (SP) or double-periodic (DP) structure, Figure 2.7 (e, f). Both structures are close in energy so it is thought that both types should be present in diamond.

For both the perfect and partial dislocations the glide set of dislocations was lower in energy than the shuffle set [96]. Perfect and partial dislocations mentioned throughout this thesis should be assumed to be of the glide type, rather than the shuffle type.

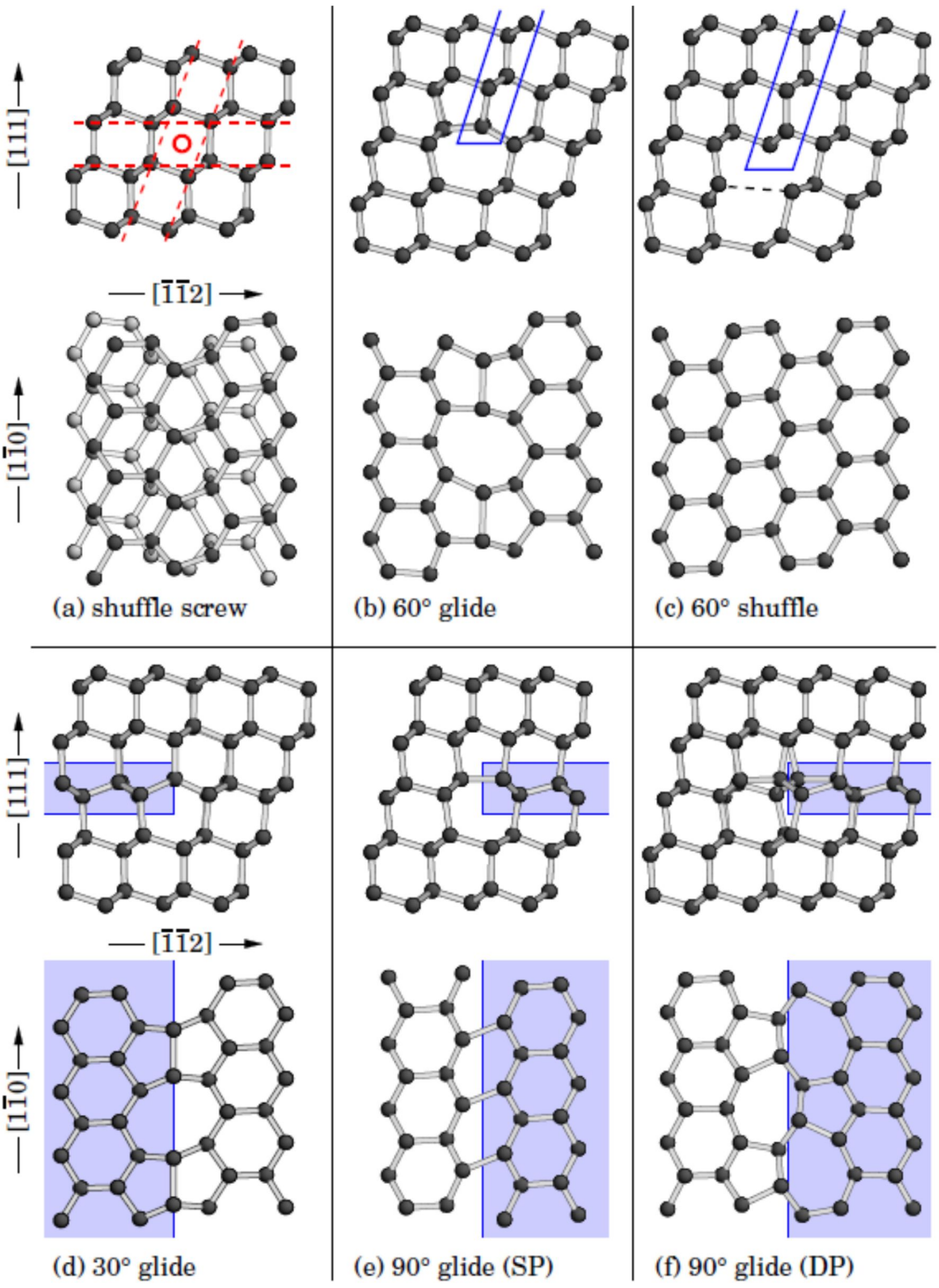

Figure 2.7: DFT optimised models showing the atomic structure of the (a) shuffle screw dislocation, (b) 60° glide dislocation, (c) 60° shuffle dislocation, (d) 30° glide partial dislocation, (e) 90° glide partial dislocation with single periodic (SP) reconstruction, and (f) 90° glide partial dislocation with double periodic (DP) reconstruction. Dislocation cores are viewed along the [110] and [111] directions. Image from Blumenau et al.[96].

2.2.4 Dislocation Kinks and Jogs

Dislocations aren't completely straight within materials and can have segments that change direction along the dislocation line. These segments are the result of the periodic nature of the lattice and are called kinks or jogs depending on the nature of the segment. In the Peierls-Nabarro model, the dislocations in a low energy configuration lie along the valleys of minimal displacement potential, from the atoms on the glide plane. These valleys are separated by "hills" of displacement potential [66].

Dislocation kinks are sections of the dislocation line that lie over a Peierls hill and connect the dislocation between two neighbouring Peierls valleys, Figure 2.8 (a). Dislocation kinks lie on the same glide plane as the dislocation. Kink pairs, like A and B in Figure 2.8 (a), can be formed when a section of dislocation jumps over the Peierls hill into a neighbouring valley. The formation of kink pairs can be thermally activated and is thought to play an important role in the low temperature glide motion of dislocations [66,96], discussed further in Section 2.2.5. Kinks can move along the dislocation line by thermal motion but must overcome Peierls hills perpendicular to the dislocation line.

A dislocation can propagate on two different glide planes, and is joined by a section known as the dislocation jog, Figure 2.8 (b). The jog has line direction normal to the glide plane of the dislocation. A jog or unit jog is defined as segments of the dislocation line which is only one glide plane in height, with plane spacing d, while a jog which spans more than one glide plane is termed a superjog. Jogs can be formed as a result of the climb of a dislocation section and, similarly to kink, can appear as a jog-pair. While kinks are associated with the glide motion of a dislocation, jogs are associated with the climb [66], see Section 2.2.5. Jogs are sessile but are able to move however by the emission or absorption of intrinsic point defects.

2.2.5 Dislocation Movement

Dislocations can move throughout the crystal in two different ways, either by glide or climb.

Glide movement is the movement of the dislocation, upon the application of external forces or stresses, involving only the breaking and forming of new bonds at the dislocation core, Figure 2.9. This movement is easily reversible, applying stress in the opposite direction causes the dislocation to move in the opposite direction. The dislocation is restricted to only move on the glide plane of the dislocation. Dislocation movement occurs in the direction perpendicular to the line direction of

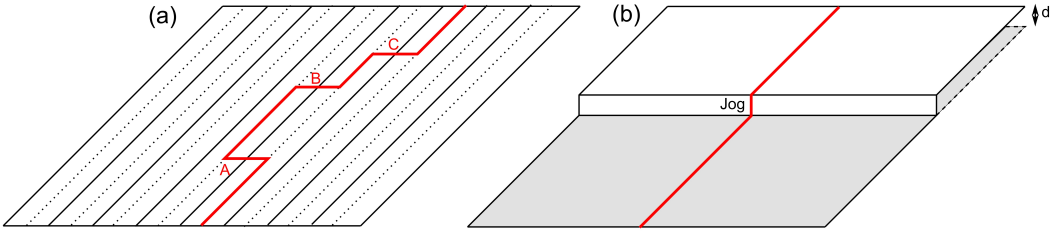

Figure 2.8: (a) Dislocation lying on a single glide plane containing dislocation kinks. Dislocation shown as red line with dislocation kinks denoted by A, B and C. Peierls valleys denoted by dotted black lines and Peierls hills by solid black lines. (b) Dislocation with jog connecting dislocation sections on neighbouring glide planes, with plane separation d. The jog connects the dislocation between the original glide plane (shaded grey) and a new glide plane (white).

the dislocation. Dislocation glide does not occur by every point along the length of the dislocation moving at the same time, instead glide is thought to occur by the nucleation of kink pairs and subsequent movement of the kinks along the dislocation line. The dislocation completes a translation into the next Peierls valley once the kinks reach the surface or have merged with neighbouring kink pairs.

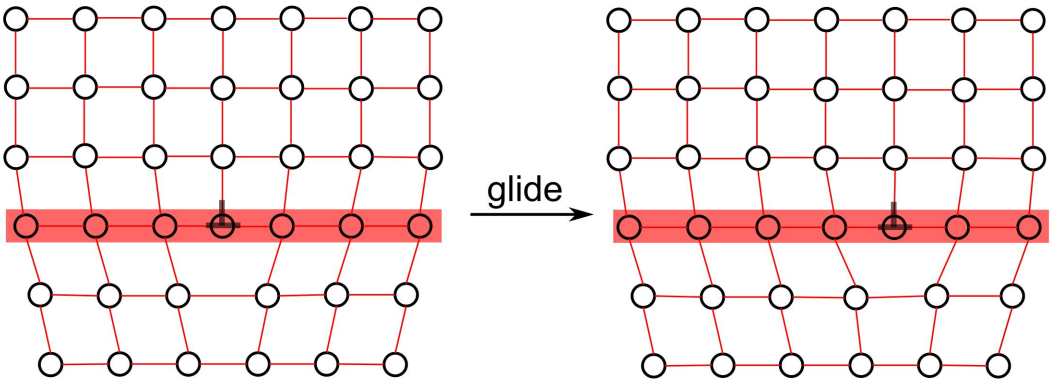

Figure 2.9: Schematic of dislocation glide motion in a simple cubic lattice. Based on Blumenau (2002) [96]. Atoms shown by empty circles. Glide plane highlighted by red colour. The dislocation line is denoted by the upside-down T.

Edge and mixed type dislocations only lie on one glide plane, defined by the Burgers vector and line direction of the dislocation. Screw type dislocations don't have a singular glide plane and can move along any of the glide planes the dislocation lies on. Since screw dislocations don't have a singular glide plane, they can undergo

cross slip and move between different glide planes. Dissociated dislocations can also move by glide but are restricted to lie on the plane of the stacking fault, which is the same glide plane the perfect dislocation lies on. Dislocation glide is a conservative movement, not requiring the absorption or emission of point defects to produce movement.

Dislocation climb is the non-conservative movement of dislocations which "climb" to different glide planes by the absorption or emission of either interstitials or vacancies, Figure 2.10. This movement is not easily reversible, requiring point defects to be generated to facilitate the movement.

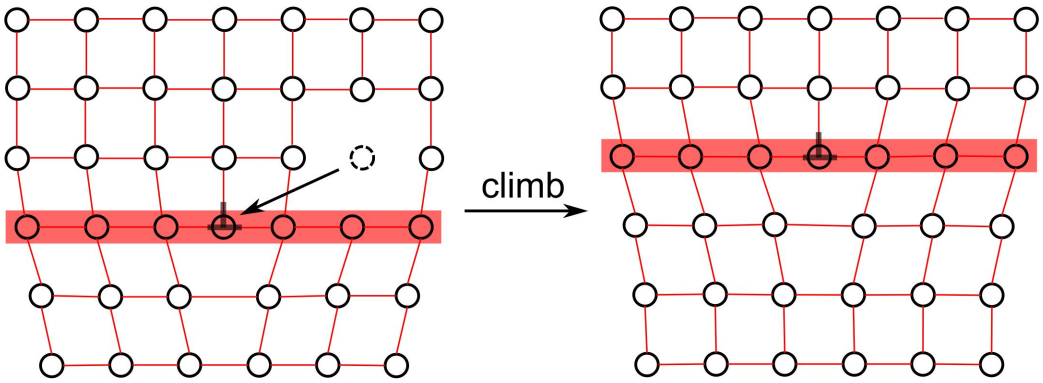

Figure 2.10: Schematic of dislocation climb motion in a simple cubic lattice. A nearby vacancy (dashed circle) is absorbed onto the dislocation causing climb. Based on Blumenau (2002) [96]. Atoms shown by empty circles. Glide plane highlighted by red colour.

2.2.6 Dislocation Reactions in FCC Materials

During plastic deformation, moving dislocations will interact with other dislocations. Depending on the Burgers vector, line direction and glide plane of the two dislocations, the dislocations can undergo several different reactions. The reaction products produced by dislocation interactions in fcc materials has been examined by Hirth (1961) [98]. The reaction products produced by the interaction of dislocation with Burgers vector BA can be seen below in Figure 2.11.

The mixed character of the 60° dislocations produce a variety of dislocation reaction products. Dislocations reacting on different glide planes tend to form jog-kinks or jog-jogs on the two dislocations involved, while dislocation reacting on the same glide plane will annihilate, combine or repel each other. The jogs formed will produce point defects upon dragging during plastic deformation. Of the 24

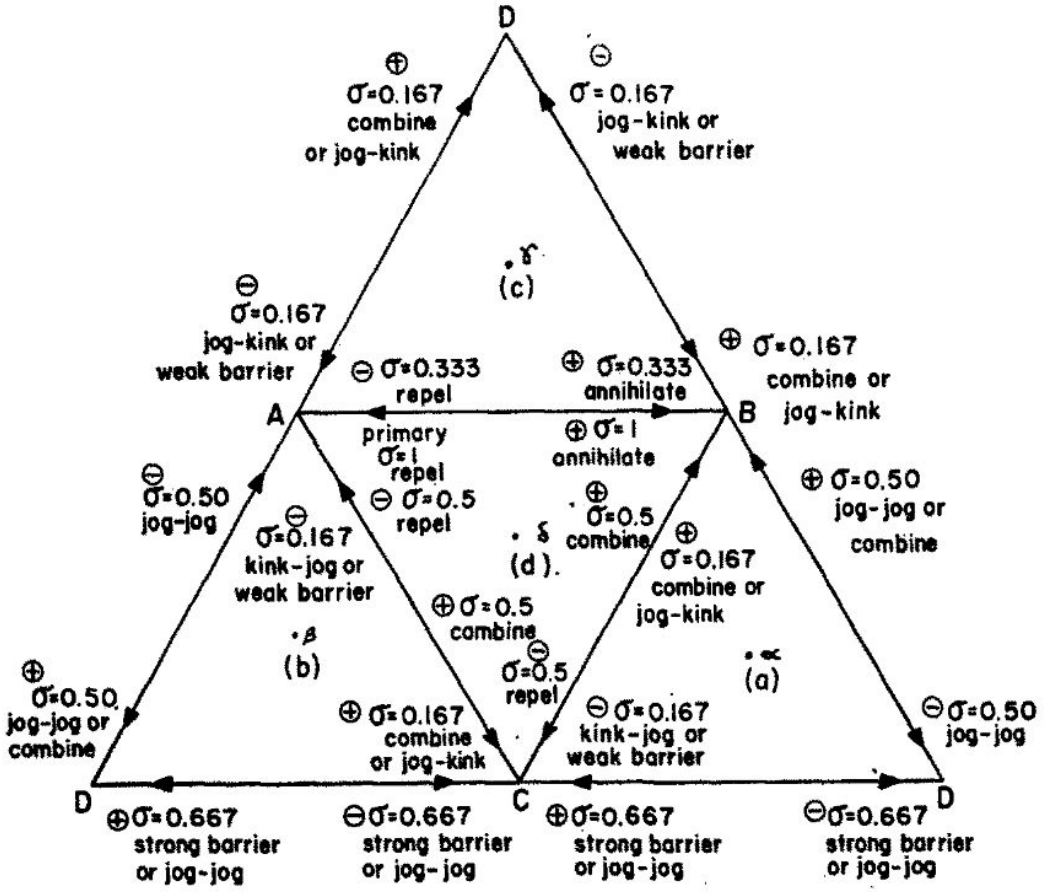

Figure 2.11: Dislocation reaction products for a dislocation with Burgers vector BA on glide plane γ. $\oplus$ and $\ominus$ correspond to the either positive or negative long range attractive force. Image from Hirth [98].

reactions a single dislocation can be involved in, two-thirds of the reactions have the possibility of producing a jog in one of the dislocations. Of these jogs produced half will generate vacancies upon dragging and the other half will produced interstitials. 12 of the possible reactions provide barriers to dislocation movement and so will contribute to work hardening of the material [98]. Similar tetrahedra can be produced for dislocations on other glide planes and with different Burgers vectors.

Chapter 3

Methods and Materials

3.1 Scanning Electron Microscopy (SEM)

Scanning electron microscopy (SEM) is a valuable technique for imaging bulk samples, able to produce a multitude of different signals for material characterisation, Figure 3.1. Images are formed by rastering a focussed beam of electrons across the sample surface and, at each point on the sample/image, measuring the intensity of the various signals generated on an appropriate detector. SEM differs from Transmission Electron Microscopy (TEM) by primarily detecting the electrons/signals emitted from the surface, rather than the forward scattered electrons. As such, SEM is more suited towards surface imaging rather than "bulk" sample imaging. Both Electron Backscatter Diffraction (EBSD) and Cathodoluminescence (CL), used in this study, will be discussed in the next few sections.

3.1.1 Electron BackScatter Diffraction (EBSD)

A significant number of primary electrons incident on the sample are elastically backscattered, leaving the sample from the same surface they entered with an energy of the order of the beam electrons. These electrons are termed Backscattered Electrons (BSE) and are one of the most commonly used signals to image materials[100]. Due to their large energy, the mean free path of BSE within the material can be large, able to travel large distances both laterally and in depth before leaving the surface. The trajectories of 15kV electrons in diamond can be simulated using Monte Carlo methodology, Figure 3.2, showing the path of the BSE within the sample, red trajectories.

The main mechanism producing contrast in a BSE image is atomic number contrast (Z-contrast), where heavier atoms produce a greater BSE signal due to

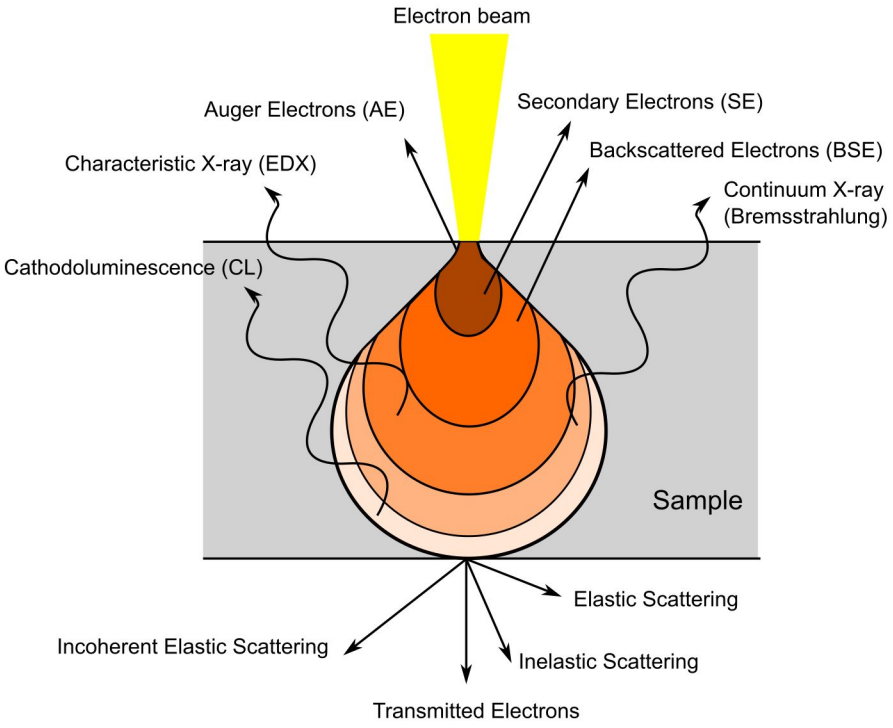

Figure 3.1: Schematic showing the various different signals generated by the interaction of the beam electron with the sample. Image based on Nanakoudis [99].

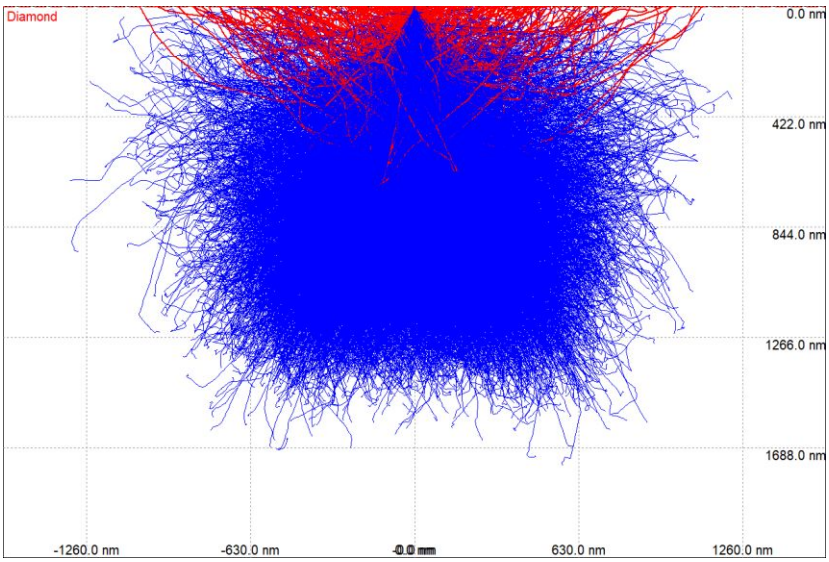

Figure 3.2: Electron Trajectories in diamond calculated by Monte Carlo simulation of 15kV electron beam. Red trajectories show BSE which have exited the sample from the incident surface.

their larger backscatter coefficient, and topographical contrast, where the topography of the surface can affect the number of BSE leaving the surface[100]. For flat, single atom, crystalline materials the effects of atomic number and surface topography are effectively removed, and crystal orientation effects becomes the dominant contrast mechanism. Electron Channelling Contrast Imaging (ECCI) and Electron Backscatter Diffraction (EBSD) are two techniques which both use diffraction to obtain structural information about the material under investigation.

In ECCI, image contrast is produced by variations in the local diffraction conditions at the surface between the bulk perfect crystal and defects, such as dislocations, at the surface. In contrast, EBSD utilises diffraction of the BSE, producing an EBSD pattern, which contains crystallographic information about the sample.

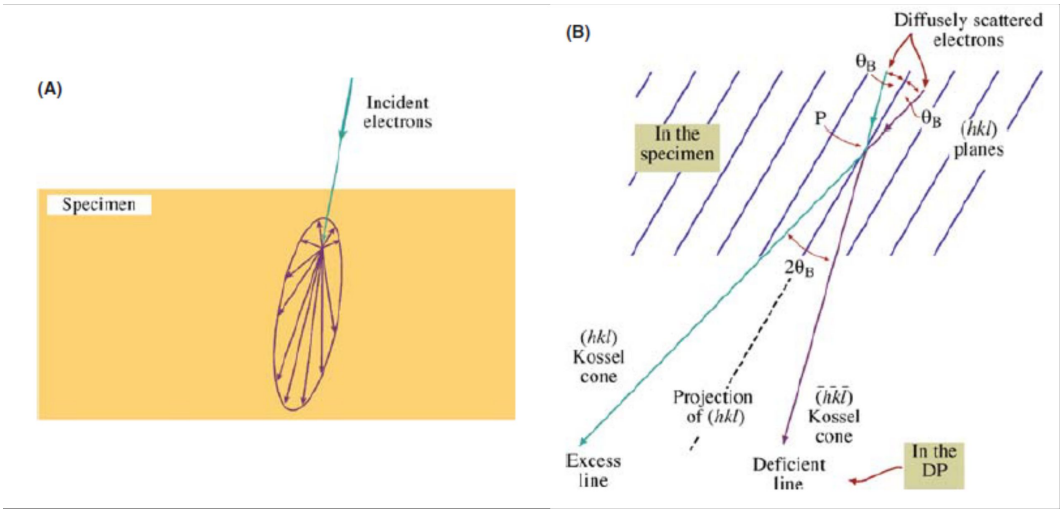

Figure 3.3: (a) Schematic of electrons incident on sample undergoing scattering at a point. Electrons can scatter in any direction but are mainly forward scattered. (b) Formation of Kossel cone due to inelastically scattered electrons satisfying the Bragg condition, θ_B. Each cone produces a line in the diffraction pattern (DP) of the crystal. Image from Williams & Carter *"Transmission Electron Microscopy: A Textbook for Materials Science"* [101].

The EBSD technique relies on incident electrons which have been inelastically scattered, losing a small amount of energy and changing direction, before being elastically backscattered towards the surface. The BSEs can be scattered in any direction, but some of them will end up satisfying the Bragg conditions for diffraction from the crystal planes ($+\theta_B$ and $-\theta_B$). The electrons which satisfy this condition will lie on Kossel cones, Figure 3.3, which define all possible k-vectors, in 3D, that satisfy the Bragg condition for a particular diffraction plane.

EBSD patterns are typically formed using a forward scattering geometry with high sample tilt, approx. 70°, where the BSEs are detected on a phosphor screen. The Kossel cones will appear as two parallel lines on the detector, due to the intersection of the detector plane with the Kossel cones. These two parallel lines, separated by $2\theta_B$ and tracing the diffraction plane, are termed Kikuchi bands. Including all the Kikuchi bands from other diffracting planes, results in the formation of a Kikuchi/EBSD pattern. An example of a diamond Kikuchi pattern can be seen in Figure 3.4.

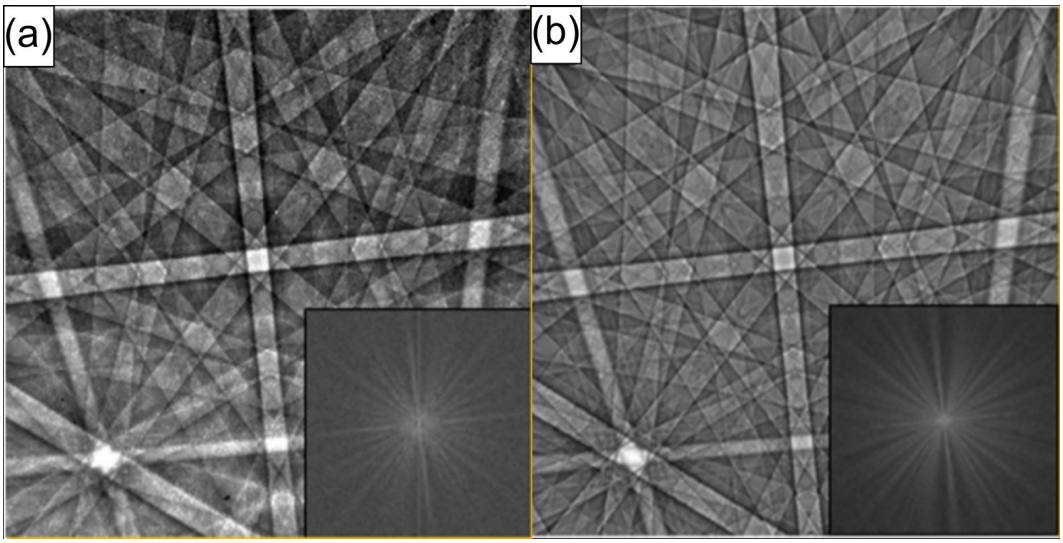

Figure 3.4: (a) EBSD pattern of Diamond using a high pass filter. (b) Simulated Image of Diamond EBSD pattern. The insets are 2D Fourier transforms of the Kikuchi patterns. Image reproduced from Vespucci et al.[102]

The Kikuchi pattern formed by EBSD can be used to accurately determine the crystal structure, orientation and phase of materials[100,103]. The Kikuchi (EBSD) pattern is fixed with respect to the crystal, meaning that rotation of the crystal results in an equivalent rotation of the Kikuchi pattern. Zone axes can be observed at the intersection of two or more Kikuchi bands, and the orientation of the crystal can be determined by measuring the angles at which several zone axis are located. Specialist software is used to automate the analysis, measuring the positions of the zone axis and Kikuchi bands to determine the crystal orientation. In the SEM, the orientation at each point in the image can be determined, forming a map of crystal orientation at the sample surface. Kikuchi patterns are formed by the same mechanism in the TEM, although in the forward scattered geometry, and are extremely useful in orientating the sample.

EBSD studies within this thesis were carried out on a FEI (Field Electron and Ion Company) Versa using an Oxford Instruments Symmetry EBSD detector with an accelerating voltage of 20 kV. EBSD patterns were analysed in Oxford Instruments AZtecHKL EBSD software. The sample was tilted at 70° to the beam with a working distance of 14.1 mm and probe current of 14 μA for low magnification mapping.

3.1.2 Cathodoluminescence (CL)

Cathodoluminescence is the emission of light due to excitation from incident primary electrons. The technique is mainly used in the study of semiconducting and insulating materials, which contain a band gap between the conduction and valence band. Within the sample, the primary electrons lose energy through a series of inelastic interactions, generating a large numbers of electron-hole (e-h) pairs along their trajectory. The volume in which the beams electrons have sufficient energy to generate e-h pairs is commonly referred to as the generation volume. The generation volume can be pear-shaped, near spherical or hemispherical, depending on the atomic number of the material and the accelerating voltage used. The energy require to generate an electron-hole pair, E_i, is approximately three times larger than the band gap energy, E_g, Eq. 3.1.

$$E_i = 2.8E_g + M \tag{3.1}$$

where M is $0 < M < 1$ eV, which is dependent on the material. A beam electron, with energy 10 - 20 kV, can therefore produce several thousand e-h pairs along its trajectory. Photons are emitted when the e-h pairs recombine, either across the band-gap or from energy levels within the band gap, caused by defects in the material (such as intrinsic point defects, impurities, dislocations, etc.), Figure 3.5. Point defects/impurities can produce energy levels within the band gap of the bulk material and will typically produce sharp spectral features in the CL spectrum [100].

Defects can have a variety of different CL behaviours, either being CL emitters, sensitizers (boosting the CL emission of other defects), or quenchers (reducing CL emission in their vicinity) [104,105]. Point defects in diamond, such as the N-V, H3 and N3 centres, are CL emitters while dislocations quench CL emission, acting as non-radiative recombination centres, as seen later.

CL shares some similarities to Photoluminescence (PL), discussed in Section 3.2, and the two techniques have been found to be comparable [106]. However there are some differences which can influence the choice of which technique to use. The

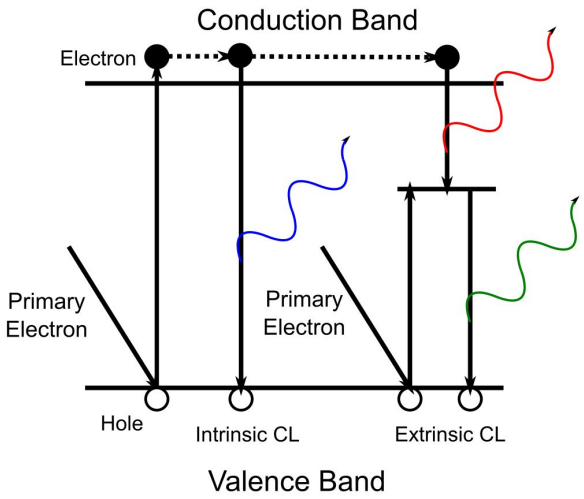

Figure 3.5: Band structure showing CL emission and generation. Emission across the band gap or from intrinsic defects is termed intrinsic CL. Emission generated by impurities is termed extrinsic CL.[100]

main advantage of carrying out CL in the SEM is the much higher spatial resolution that can be achieved compared to PL, able to examine the emission from areas a few nm's to μm's in greater detail. However, the incident electrons provide a continuum of excitation energies meaning every defect transition will be excited, preventing the selective excitation of certain defect transitions.

CL spectroscopy here was carried out in a Zeiss Supra 55VP equipped with a Gatan MonoCL3 system using beam energies of 20 - 30 kV. For optimal light collection with the hyperbolic mirror, a working distance of $\sim$ 11 mm was used. Panchromatic imaging was carried out at 5 kV using a variable pressure secondary electron (VPSE) detector. The choice of accelerating voltage will be discussed in section 3.1.3. The VPSE detector detects the photons emitted from ionised gas in the chamber, due to secondary electrons from the sample, during operation in Variable Pressure mode[100]. By operating the SEM in High Vacuum mode, only photons generated by CL have been detected. The use of the VPSE detector for panchromatic imaging negates the need for a parabolic mirror to collect the photons, which only collects photons efficiently from the focal point of the mirror, allowing CL images over much larger areas to be taken. The VPSE detector cannot detect the energy of the incident photons so the image formed is effectively a panchromatic CL image. The VPSE detector was used over the MonoCL3 system for panchromatic imaging due to the larger field of view that can be achieved.

3.1.3 Monte Carlo Simulations of the CL Generation Volume

The spatial resolution (δ) that can be achieved by CL in the SEM is determined by three primary factors; the spot size of the electron beam (probe diameter, d_p), the lateral size of the generation volume in the material (diameter, d_g) (the volume over which electron-hole pairs are generated), and the (minority) carrier diffusion length (L), given by Eq 3.2 [107].

$$\delta = \sqrt{d_p^2 + d_g^2 + L^2} \tag{3.2}$$

Most modern SEM's can achieve spot sizes of a few nm, far smaller than the generation volume and the carrier diffusion length in materials, so the probe diameter can be ignored [107]. The carrier diffusion length is a characteristic of the material and as such depends on the material we want to investigate. The size of the generation volume is therefore the only factor we have control over. If the carrier diffusion length is much greater than the diameter of the generation volume, $L > d_g$, then the scattering of the electron beam can be ignored. The shape and diameter of the generation volume can instead be treated as a point source, with the resolution determine solely by the carrier diffusion length [107]. When the carrier diffusion length is much smaller than the generation volume, $L < d_g$, then the size of the generation volume becomes the dominant factor controlling the spatial resolution of a CL image. Monte Carlo simulations, which don't take into account carrier diffusion lengths, can be used to model the generation volume under different beam conditions to study their effect on the spatial resolution.

The simplest method to control the size of the generation volume is changing the accelerating voltage used. Simulations were carried out using the CASINO Monte Carlo (v2.5.1.0) simulation package developed by Hovington et al. (1997) [108], with further developments by Drouin et al. (2007) [109]. A beam with spot size of 2 nm and accelerating voltages between 1 - 15 kV were simulated in diamond and the lateral and depth profile of the CL emission were extracted. For good statistics, the trajectories of 1 million electrons were simulated. An example of the CL intensity with depth along with the cumulative CL intensity with depth is plotted for a 10 kV accelerating voltage, Figure 3.6. Similar plots are obtained for the CL intensity generated with lateral distance from the beam.

Figure 3.6 shows both how the CL intensity varies with depth in the sample and the cumulative CL intensity with depth. Looking at the CL intensity with depth (Figure 3.6 black line) CL emission peaks at approximately 350 nm, however this only accounts for approximately 50% of the CL signal. Significant CL signal is still

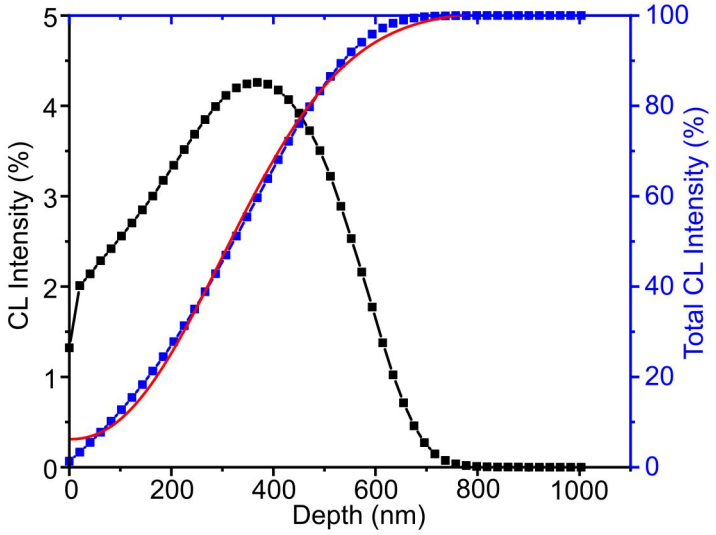

Figure 3.6: CL intensity (black) and cumulative CL intensity (blue) with depth for an electron beam with 10 kV accelerating voltage. Weibull CDF fit shown by red line.

generated at greater depths, as shown by the cumulative CL intensity, Figure 3.6 (blue). Defining the depth and lateral size of the generation volume as the distance encompassing 90% of the total CL intensity, the depth and radius of the generation volume can be plotted against the accelerating voltage, as shown in Figure 3.7.

As expected, Figure 3.7 shows that as the accelerating voltage is increased the penetration depth and lateral spread of the electrons also increases. The best spatial resolution is achieved when a smaller accelerating voltage is used, caused by a reduction in the size of the CL generation volume. This effect can clearly be seen when imaging diamond, Figure 3.8, where the non-radiative sub-grain boundaries can be resolved within a halo of emitting material.

As the accelerating voltage is decreased smaller features can be resolved, as the generation volume becomes smaller in size. There is a trade-off with using a smaller accelerating voltage however, the CL technique becomes more surface sensitive as the electrons don't penetrate as far into the sample and the smaller generation volume leads to a reduced CL signal being generated - less CL emitters are excited with a smaller interaction volume. This can be detrimental when carrying out CL spectroscopy where losses from the optics further reduce the CL signal detected. Changing the accelerating voltage, in addition to controlling the spatial resolution, has also been used as a means of performing depth profiling, where the CL signal at different depths can be probed [110–112].

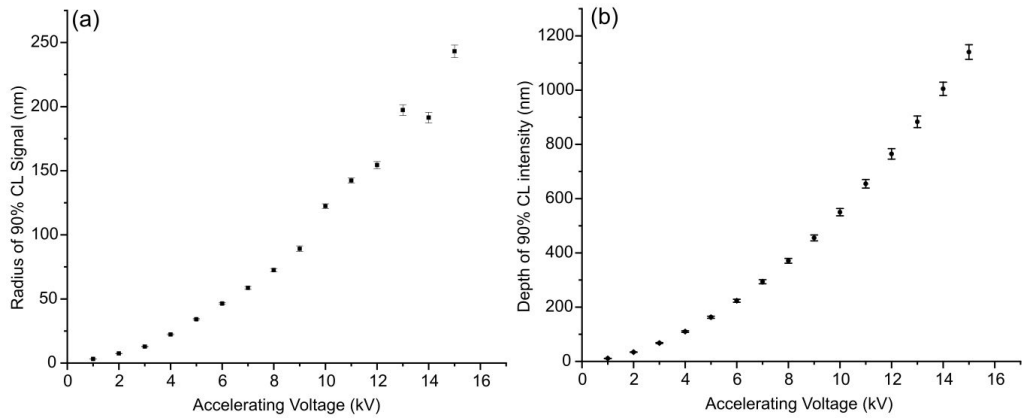

Figure 3.7: Monte Carlo simulation of the CL generation volume showing (a) Radius and (b) Depth at which 90% of the CL signal is generated.

Another method that can be used to reduce the size of the generating volume is to reduce the sample thickness. In the bulk sample the electrons experience many scattering events which cause a large spread in the sample, Figure 3.2. If the thickness of the sample is decreased, so that the electrons can be transmitted through the sample, then the number of scattering events an electron experiences before reaching the exit surface is reduced, Figure 3.9, leading to a much smaller lateral spread.

Monte Carlo simulations of electron trajectories, using a 3 nm probe diameter, in a 100 nm thick diamond film was carried out to investigate the effect of the accelerating voltage on the CL resolution in a thin film. As before, the radius enclosing 90% of the CL signal was plotted against accelerating voltage, Figure 3.10.

It can be seen that larger accelerating voltages lead to better lateral resolution as the electrons undergo fewer scattering events before exiting the sample. The change in resolution is smaller for accelerating voltages above 10 kV, with the radius of the generation volume approaching the diameter of the probe. The CL intensity generated with depth is constant throughout the thickness, although the simulations do not take into account non-radiative surface recombination which will reduce CL emission near the surfaces. For thin films below the thickness of the electron penetration depth, the CL intensity will be strongly dependent on the thickness of the film, and can be affected by interference of light reflected from both top and bottom surfaces[113].

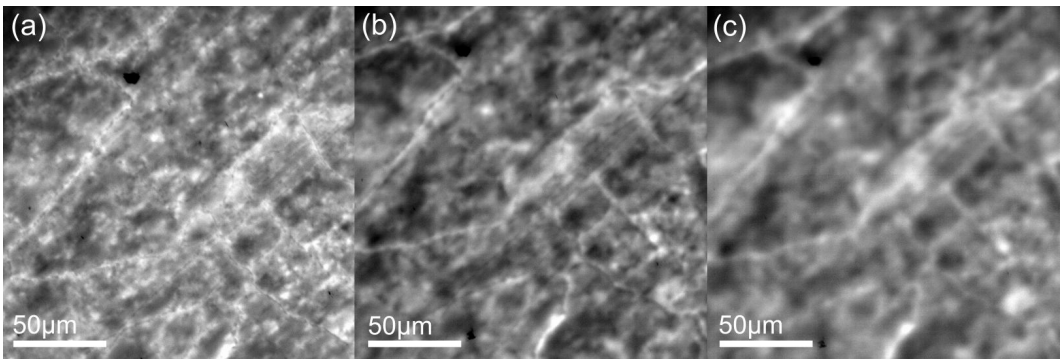

Figure 3.8: Cathodoluminescence image of dislocation structures in diamond using an accelerating voltage of (a) 5 kV, (b) 10 kV, and (c) 15 kV. Finer features can be seen when using a smaller accelerating voltage.

3.2 Photoluminescence (PL)

Photoluminescence (PL) is the study of the light emitted from a sample due to excitation with photons, usually from a laser. PL is a commonly used non destructive technique in the characterisation of diamond, allowing for the identification of optically active defect species and determination of point defect properties [114,115]. Light incident on the sample with sufficient energy can promote electrons from the ground state into a higher energy state, similar to Figure 3.5, which then relax back down to the ground state either radiatively, releasing a photon in the process, or non-radiatively, generating phonons. Electrons relaxing via defect states typically produce sharp spectral features, from well-defined energy levels within the band gap, providing information about the band structure of the defect [115]. Provided the mean free path of excited electrons is smaller than the FWHM of the laser spot on the sample, then the resolution of PL is determined by the size of the excitation spot on the sample [116], with the resolution limited to the diffraction limit of light. Super resolution microscopy techniques have been developed in recent years which can now beat the diffraction limit, with resolutions of 10's - 100's of nm possible. A review of current super resolution microscopy techniques is given by Schermelleh et al. (2019) [117].

An advantage PL has over CL is the selectivity of excitation wavelength which can be used, meaning it is possible to choose which defects to excite. Additionally, the strength of certain excitations varies with excitation wavelength [114,115]. Using a confocal microscope with motorised stage, spectral features can be mapped throughout the sample showing the spatial distribution of the point defects.

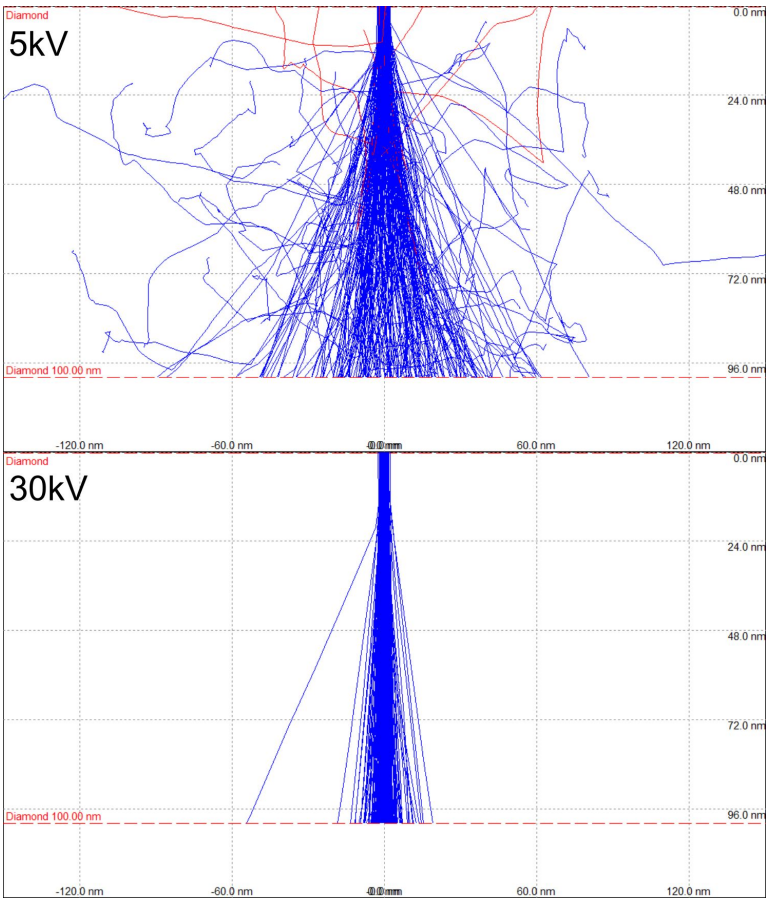

Figure 3.9: Electron Trajectories in 100 nm thick diamond thin film for 5 and 30 kV electrons.

PL spectroscopy mapping was carried out on a Horiba LabRAM Evolution microscope and spectrometer using a 488 nm solid state laser, step size of 5 μm, and a Renishaw InVia confocal microscope using a 325 nm HeCd laser, step size of 7.5 μm, at liquid nitrogen (LN) temperatures. Raman mapping was carried out on the Horiba LabRam Evolution microscope and spectrometer using a 660 nm solid state laser, step size 2 μm, at LN temperatures.

3.3 Transmission Electron Microscopy (TEM)

TEM is a bulk imaging technique, used to observe defects within the bulk of the material. Images are formed using electrons which have been transmitted through a thin electron transparent sample, interacting with the sample in the process, before being detected on a CCD detector. The electrons are incident on the sample

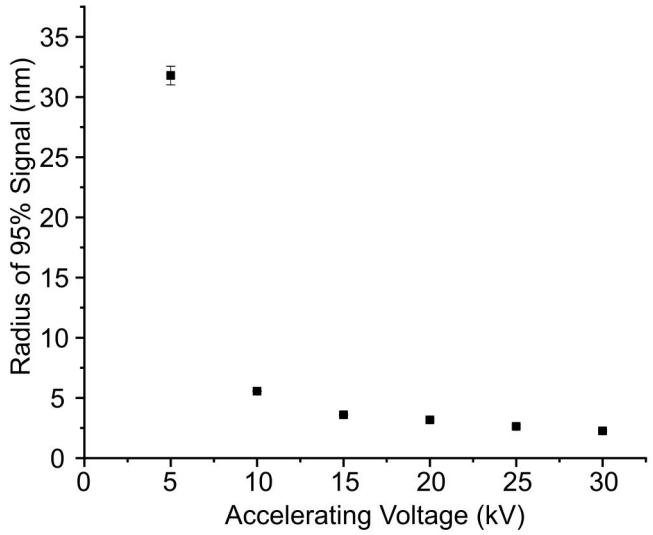

Figure 3.10: Radius in which 95% of the total CL signal is enclosed for different accelerating voltages for a 100 nm thick thin film of diamond. Probe diameter 3 nm.

as a parallel beam, rather than the focussed beam of electrons used in the SEM. The incident electrons can be described as both a particle and a wave, with both descriptions being useful in discussing STEM and TEM imaging. The wavelength of the electron is affected by the accelerating voltage used and, taking into account relativistic effects, is given by:

$$\lambda = \frac{h}{[2m_o eV(1 + \frac{eV}{2m_o c^2})]^{\frac{1}{2}}} \tag{3.3}$$

where h is Planck's constant, m_o is the rest mass of the electron, eV is the kinetic energy of the electron (charge $\times$ accelerating voltage) and c is the speed of light. Eq. 3.3 gives an electron wavelength of 2.51 pm at 200kV and 4.18 pm at 80kV.

As the electrons travel through the sample they can experience different scattering mechanisms which can be broadly split into two categories, elastic and inelastic scattering, Figure 3.1. The electrons can be scattering in all directions however, in the TEM, only the forward scattered electrons are detected. Backscattered electrons are used to form images in the SEM. Referring to the wave nature of the electrons, the scattered electrons can also be coherently or incoherently scattered. Elastically scattered electrons are usually coherently scattered, except when the scattering angle is large, while the inelastically scattered electrons are usually

incoherently scattered. The description of the electrons as waves is only important in the case of elastically and coherently scattered electrons.

To form an image in the TEM two types of contrast mechanisms can be utilised, amplitude and phase contrast. Both mechanisms can contribute to the image, however the microscope is usually set up with conditions that favour only one of them. Mass-thickness, diffraction and Z-number contrast are all types of amplitude contrast, where the contrast is produced from differences in the numbers of electrons detected. Phase contrast imaging, used in High Resolution TEM (HRTEM), utilises the wave nature of the electrons, forming images from the interference of multiple coherently diffracted electron beams. Only amplitude contrast imaging techniques have been used in this project, diffraction contrast in the TEM and Z-number contrast in the STEM. Both techniques will be discussed in more detail in the following sections.

3.3.1 Electron Diffraction

Before discussing diffraction contrast imaging in the TEM it is useful to describe electron diffraction. Treating the electrons as waves, electron diffraction can be described in a similar manner to the Bragg diffraction of X-rays, where the electrons appear to reflect from crystal planes before constructively or de-constructively interfering, depending on the path length difference. Taking the case of electrons scattering from a single crystal plane, the primary electrons are incident on the sample as a flat wavefront with wavevector, $\mathbf{k_I}$ and scattered from the plane into a new direction with wavevector, $\mathbf{k_D}$, Figure 3.11(a). The scattered beam is not necessarily a diffracted beam, with diffraction only occurring if the electrons constructively interfere. This will be dependent on the angle between the incident electrons, scattered electrons and the crystal planes. The electrons are elastically scattered meaning no energy is lost in the scattering process, only the direction is changed. A scattering vector, $\mathbf{K}$, can then be defined as in Figure 3.11(b,c) and Eq. 3.4.

$$\mathbf{K} = \mathbf{k_D} - \mathbf{k_I} \tag{3.4}$$

Since no energy is lost in the scattering event, the magnitudes of the wave vectors, $|\mathbf{k}|$, are equal and unchanged:

$$|\mathbf{k_I}| = |\mathbf{k_D}| = \frac{\mathbf{1}}{\lambda} = |\mathbf{k}| \tag{3.5}$$

From Figure 3.11 we can see that:

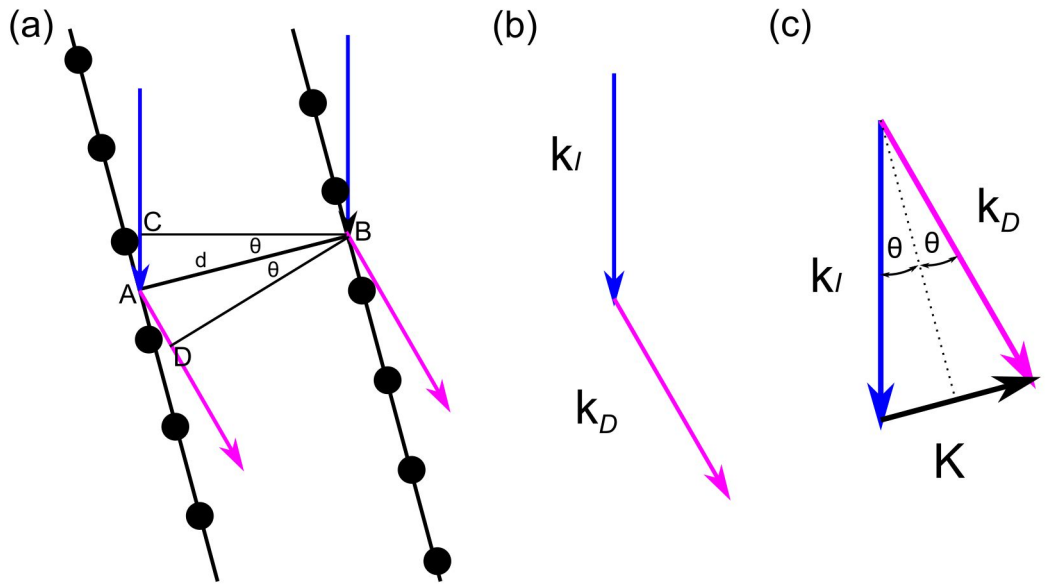

Figure 3.11: (a) Diffraction from crystal planes at the Bragg angle. (b) Definition of the scattering vector. Schematic of wave vectors of incident , $\mathbf{k_I}$, and diffracted, $\mathbf{k_D}$, electron. (c) Scattering vector, $\mathbf{K}$, given by the difference of the incident, $\mathbf{k_I}$, and diffracted, $\mathbf{k_D}$, wave vectors.

$$sin(\theta) = \frac{|\mathbf{K}|/\mathbf{2}}{|\mathbf{k_I}|} \tag{3.6}$$

Which can be rewritten as:

$$|\mathbf{K}| = \frac{\mathbf{2sin}(\theta)}{\lambda} \tag{3.7}$$

The Bragg condition for crystal diffraction is given by:

$$n\lambda = 2dsin(\theta_B) \tag{3.8}$$

where d is the slit, or plane spacing. Comparing Eq. 3.7 with Eq. 3.8, we can see the equations are the same under the conditions of n = 1, the scattering angle, θ, is equal to the Bragg angle, θ_B and the magnitude of the scattering vector is:

$$|\mathbf{K_B}| = \frac{\mathbf{1}}{\mathbf{d}} \tag{3.9}$$

For diffraction to occur, the magnitude of the scattering vector must be the

reciprocal of the lattice plane spacing. The vector, K_B, can also be defined as the vector, **g**, so that:

$$\mathbf{K_B} = \mathbf{g} \tag{3.10}$$

The vector, **g**, is sometimes called the diffraction vector. It is a vector with direction normal to the diffraction planes and a length equal to the reciprocal of the plane spacing. The vector, **g**, is also a vector in the reciprocal lattice. The reciprocal lattice is a mathematical construct, obtained from the Fourier transform of the real space crystal lattice, and is useful in understanding diffraction. In a real space crystal lattice, a lattice position/vector in the crystal can be described in terms of unit vectors, Eq. 3.11.

$$\mathbf{R_n} = \mathbf{n_1 a} + \mathbf{n_2 b} + \mathbf{n_3 c} \tag{3.11}$$

where **a**, **b**, and **c** are the unit vectors and n1, n2 and n3 are numbers. A vector in the reciprocal lattice, likewise, can be described in terms of reciprocal unit vectors, Eq. 3.12.

$$\mathbf{R_n^*} = \mathbf{m_1 a^*} + \mathbf{m_2 b^*} + \mathbf{m_3 c^*} \tag{3.12}$$

where the unit vectors in reciprocal space are defined by the rules that:

$$\mathbf{a^* \cdot b} = \mathbf{a^* \cdot c} = \mathbf{b^* \cdot c} = \mathbf{b^* \cdot a} = \mathbf{c^* \cdot a} = \mathbf{c^* \cdot b} = \mathbf{0} \tag{3.13}$$

and the lengths of the vectors are given by:

$$\mathbf{a^* \cdot a} = \mathbf{1};\ \mathbf{b^* \cdot b} = \mathbf{1};\ \mathbf{c^* \cdot c} = \mathbf{1}; \tag{3.14}$$

The reciprocal unit vector, $\mathbf{a}^*$ is perpendicular to **b** and **c**, likewise for the other reciprocal unit vectors. In the case that the prefactors are integer numbers, the vector, $\mathbf{R_n^*}$, takes on the form:

$$\mathbf{R_n^*} = h\mathbf{a^*} + k\mathbf{b^*} + l\mathbf{c^*} \tag{3.15}$$

where the integers h,k and l are the familiar integers used in the Miller indices. This vector, $\mathbf{R_n^*}$, is the same as the diffraction vector **g**, seen earlier in Eq. 3.10.

Each point in the reciprocal lattice, rather than describe points in a crystal, refers to planes in the crystal, where it can be shown the the spacing of those parallel

planes is given by:

$$d_{hkl} = \frac{1}{|g|} \tag{3.16}$$

As well as describing lattice planes in the crystal, the reciprocal lattice also details the points where the diffraction condition is satisfied. The diffraction pattern can be described from the Ewald sphere construction in reciprocal space. To form the Ewald sphere, the incident wave vector, $\mathbf{k_I}$, is plotted to end at the origin of the reciprocal lattice and oriented correctly with respect to the crystal geometry. Using the origin of $\mathbf{k_I}$ as the centre, a sphere with radius equal to the wave vector of the incident electron beam is plotted, as shown in Figure 3.12.

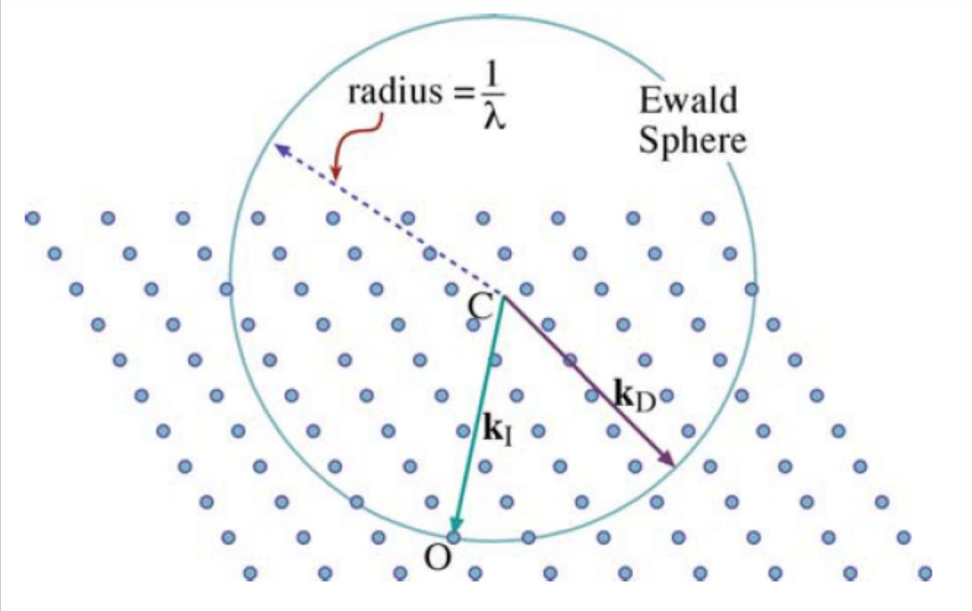

Figure 3.12: Ewald sphere drawn in the reciprocal lattice showing the incident, k_I, and scattered, k_D, wavevectors. Diffraction occurs where the Ewald sphere intersects a reciprocal lattice spot [101].

Where the Ewald sphere intersects the reciprocal lattice points, the scattering vector, $\mathbf{K}$, is equal to a reciprocal lattice point, $\mathbf{g}$, and a diffraction spot will be observed. This would be the case for a perfect crystal however in the TEM, diffraction spots can still be seen even when the crystal is slightly off the Bragg condition. The reason diffraction spots are observed when off-Bragg condition is due to the finite size of the sample.

In real space, the sample is large enough in the x and y directions to effectively be infinite, producing a point-like reciprocal lattice spot in the x-y directions.

However, along the z-axis, the sample has finite thickness, meaning the reciprocal lattice spot has a finite size along the appropriate direction in reciprocal space. Every point in the reciprocal lattice will have a rod-like shape, which are termed reciprocal lattice rods, or relrod for short. The Ewald sphere crossing this rod will produce a diffraction spot, with reduced intensity, despite the diffraction conditions not being satisfied exactly.

The condition for scattering to occur, 3.10, must therefore be modified slightly to include a deviation parameter, s, which defines how far from the Bragg condition the crystal is:

$$\mathbf{K} = \mathbf{g} + \mathbf{s} \tag{3.17}$$

When the Ewald sphere goes through the middle of the Bragg spot, $\mathbf{s} = 0$, otherwise $\mathbf{s}$ can be positive or negative if the Bragg spot is either inside or outside the sphere, Figure 3.13.

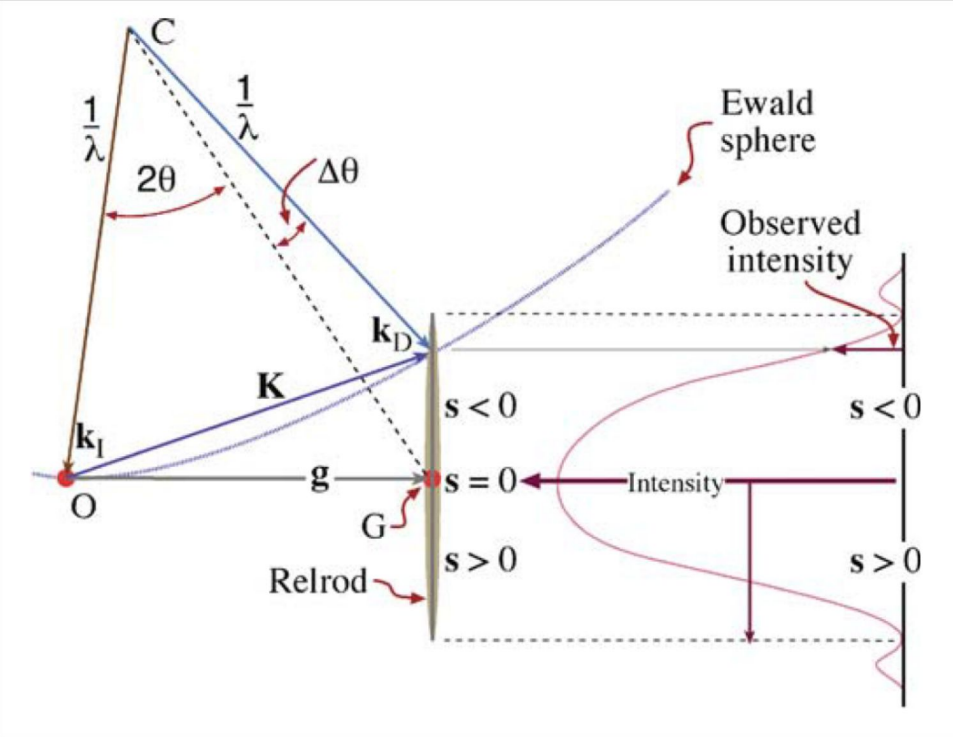

Figure 3.13: Ewald sphere intersecting with a relrod, satisfying the diffraction condition. The values of positive and negative s are defined. Image reproduced from Williams and Carter[101].

3.3.2 Diffraction Contrast

Diffraction contrast imaging is a technique highly suited to the investigation of dislocations or any defect which creates a local strain field. Diffraction contrast imaging has been used extensively in the past to image dislocations and the technique can be used to determine the Burgers vector of the dislocation. Image contrast is produced from variations in the intensity of diffracted beams at different locations in the sample, either caused by variations in the thickness, t, or by deviations in the diffraction condition, $\mathbf{s}$.

The sample is set-up in a two-beam condition, with the direct beam and one strongly diffracted beam. Contrast is formed by tilting the sample slightly off the Bragg condition ($\mathbf{s} \neq 0$), with the strain field around the dislocation core causing the lattice planes surrounding the defect to bend back into diffraction condition, producing variations in the image intensity near the dislocation core. The two-beam condition leads to better image contrast and easier to interpret images.

Apertures can be used to isolate electrons either in the direct beam, forming a Bright Field (BF) image, or in the diffracted beam, forming a Dark Field (DF) image. In a BF image, bending of the lattice planes around the core cause electrons to diffract, resulting in a drop of intensity in the direct beam around the dislocation core while in DF imaging the opposite is case, and an increase in intensity of the diffracted beam is seen, Fig. 3.14 (a). It is important to note that the intensity seen is displaced from the dislocation core and will appear to be on one side of the core, shown in Figure 3.14 (b). Which side of the dislocation core the intensity appears depends on the sign of the diffraction vector, $\mathbf{g}$, and deviation parameter, $\mathbf{s}$.

The diffraction conditions are set-up using the TEM in diffraction mode, where both Bragg spots and Kikuchi bands are seen, corresponding to the diffraction planes. The formation of the Kikuchi bands has been discussed earlier in Section 3.1.1, but are formed by the diffraction of inelastically scattered electrons. The Kikuchi pattern is more accurate in determining the orientation of the sample with the bands acting as a roadmap of crystal orientation. By tilting the sample along the Kikuchi bands, different zone axis and diffraction conditions, $\mathbf{g}$, of the sample can be set-up.

In addition to orientation, the Kikuchi bands can also be used to set the deviation parameter, $\mathbf{s}$, the sign of which is crucial in forming good quality diffraction contrast images. For ideal diffraction contrast imaging conditions $\mathbf{s}$ must be positive. This can be achieved by tilting the crystal so that the excess Kikuchi line lies outside of the diffraction spot. $s = 0$ is achieved for the excess Kikuchi line going through the Bragg spot and $s < 0$ when the excess Kikuchi line lies inside the diffraction

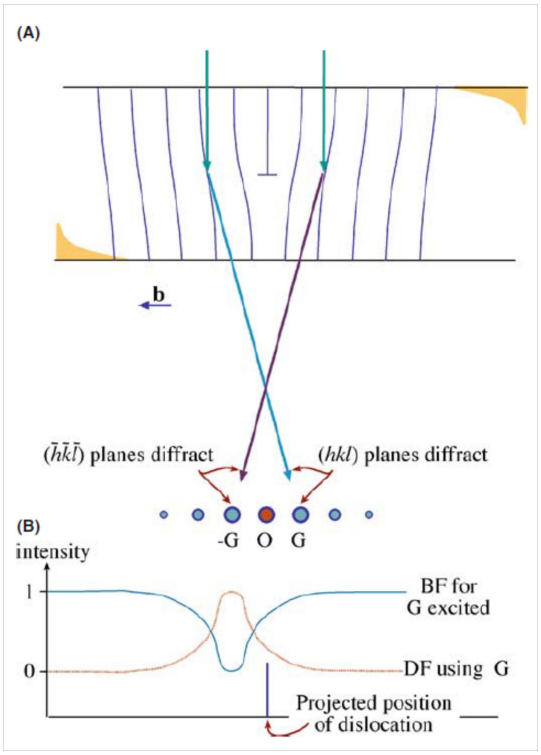

Figure 3.14: (a) Schematic showing how electrons are scattered from the planes near the core of a dislocation to produce image contrast. (b) Intensity profiles of the dislocation in Bright Field (BF) and Dark Field (DF) imaging conditions using the diffraction spot G. Image contrast is displaced from the dislocation core and can appear on either side depending on diffraction conditions used. Dislocations appear dark in BF imaging and bright in DF imaging. Image from Williams & Carter [101].

spot. A schematic of these conditions can be seen in Figure 3.15.

DF imaging is commonly performed using a centred diffracted beam, where the strongly diffracted beam travels along the optic axis, Fig. 3.16c. Rather than tilting the sample to bring the + $g_{(hkl)}$ diffraction spot onto the optic axis, the - $g_{(hkl)}$ is brought onto the same location as the direct beam.

Tilting the beam instead to bring the + $g_{(hkl)}$ onto the optic axis, results in a weak + $g_{(hkl)}$ condition and strong + $3g_{(hkl)}$, resulting in a weak beam dark field (WBDF) image, Fig. 3.16b. In WBDF imaging, the deviation parameter, **s**, is larger than DF imaging, meaning that the crystal planes have been tilted further away from the Bragg condition. Only at the core, where the lattice planes are deformed by a large amount, are the planes brought back into the diffraction condition. This allows the contrast in WBDF imaging to originate from closer to the dislocation core and with a greater resolution, on the order of a few nm. The various beam tilts

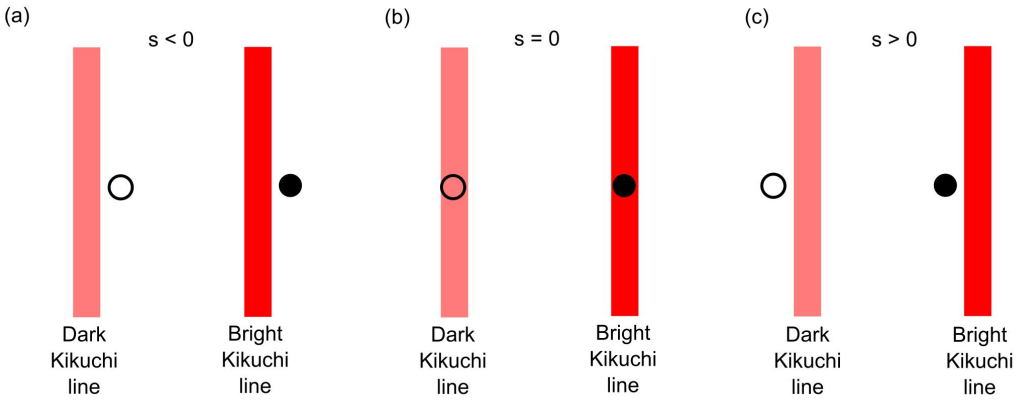

Figure 3.15: Setting the s parameter using the Kikuchi lines, (a) $s < 0$; (b) $s = 0$; (c) $s > 0$. The hollow circle corresponds to the direct beam, while the filled circle represents the diffracted beam.

required to carry out BF, DF and WBDF imaging can be seen in Figure 3.16.

Diffraction contrast imaging also allows for the Burgers vector, $\mathbf{b}$ of the dislocation to be determined by using the invisibility criterion, Eq. 3.18.

$$\mathbf{g} \cdot \mathbf{b} = \mathbf{0} \tag{3.18}$$

By imaging the dislocation under different diffraction conditions, $\mathbf{g}$, and observing when the dislocation becomes invisible, the Burgers vector can be calculated from a table of $\mathbf{g} \cdot \mathbf{b}$ values. The dislocation must be invisible under two different $\mathbf{g}$ conditions for a unique Burgers vector determination to be made. The different diffraction conditions imaged under also allow for the plane the dislocation lies on to be determined, while trace analysis can determine the line direction.

3.4 Scanning Transmission Electron Microscopy (STEM)

STEM imaging operates slightly differently from TEM imaging, using a focussed beam of electrons, similar to the SEM. The electrons are focussed to a small spot, a few pm in diameter, and rastered over the sample. For each point in the image the electrons are detected on a series of annular detectors. BF and DF images can be obtained by forming an image from electrons which have been scattered to different angles. The BF, Annular DF and High Angle ADF detectors can detect electrons scattered over a range of angles to form BF, ADF and HAADF images respectively, Figure 3.17.

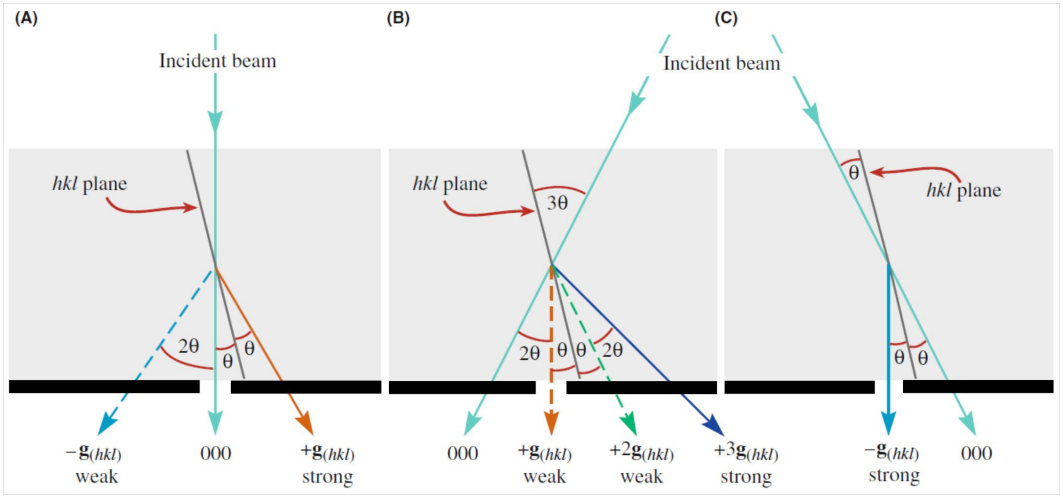

Figure 3.16: (a) Standard Two Beam condition with the direct beam and one strong diffracted beam + $g_{(hkl)}$. BF image formed by inserting an aperture to only let the direct beam reach the detector. (b) Tilting the beam to bring the + $g_{(hkl)}$ onto the optic axis results in the a weak + $g_{(hkl)}$ and strong + $3g_{(hkl)}$ condition. This forms a WBDF image. (c) Tilting the beam to bring the - $g_{(hkl)}$ onto the optic axis results in the centred DF imaging condition. Image from Williams & Carter [101].

BF detectors detect the direct electron beam, electrons that haven't interacted with the sample, or have been scattered by small angles due to inelastic scattering, typically < 50 mrads. Images in this case appear bright with the atom columns dark in contrast. The electrons scattered by atoms are not detected by the BF detector.

A DF image is formed using the ADF or High Angle ADF (HAADF) detectors to detect electrons which have been scattered to larger angles, typically > 50 - 200 mrads. Electrons which have Rutherford scattered from the nucleus to larger angles are detected while those that have not been scattered (or scattered by a small angle) are not detected. The scattering cross section increases with atomic number and so ADF and HAADF imaging is sensitive to Z-number contrast - heavier atoms appear brighter in the image. The High Angle ADF detector differs from the ADF detector by only measuring electrons that have been scattered to larger angles. With increasing scattering angles the coherency of the electrons decreases. The HAADF image formed is therefore less susceptible to interference effects that may affect the contrast, such as diffraction, which may be detected on the ADF detector.

Atomic resolution imaging, using Z-number contrast in ADF or HAADF, has become the more commonly used technique compared to phase contrast HRTEM

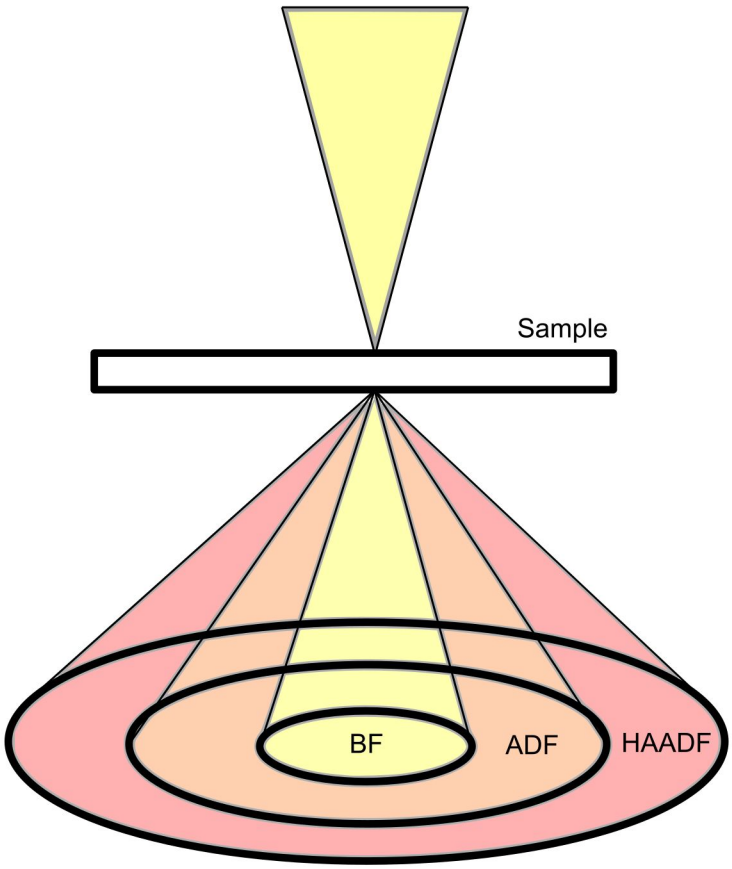

Figure 3.17: Schematic of STEM detector set-up showing how BF, ADF and HAADF images are formed by the annular detectors.

imaging, which was once widely used in the past. One of the primary reasons for this is due to the images being much easier to interpret. Interpretation of phase contrast imaging requires comparison of the images with simulations in order to understand the contrast observed.

3.4.1 Electron Energy Loss Spectroscopy (EELS)

Diffraction contrast TEM imaging and ADF STEM imaging techniques both use the coherently and incoherently elastically scattered electrons respectively to image the sample however these techniques have largely ignored the contribution of inelastically scattered electrons and the wealth of information they can provide. As the beam electrons travel through the sample, they can lose energy through inelastic scattering processes, involving electron-electron Coulomb interactions. The inelasti-

cally scattered electrons provide information about the optical, electronic, chemical and structural properties of the sample. Rather than measure the x-rays or light that can be generated by the inelastic scattering events, EELS measures the energy lost by the incident electrons after they have interacted with the sample.

The cross section for inelastic scattering is much smaller than the elastic scattering cross section, leading to a reduced angular distribution of scattered electrons. The majority of inelastically scattering electrons are only scattered by a few mrads from the beam. A comparison of the angular distribution of elastically and inelastically scattered electrons from a carbon atom is shown in Figure 3.18. In Figure 3.18, for comparison with the elastic and inelastic scattering distributions in diamond, the Lenz model is also included. The Lenz model simply describes the scattering of an fast electron from a single screened nucleus (a carbon atom), with a screening distance of $r_0 = a_0/Z^{\frac{1}{3}}$ [118]. Inelastic scattering of elastically scattered electrons can occur also, and is the reason why Bragg spots in the diffraction pattern will appear to have a diffuse halo. These inelastically scattered electrons are not of interest and not detected by the spectrometer.

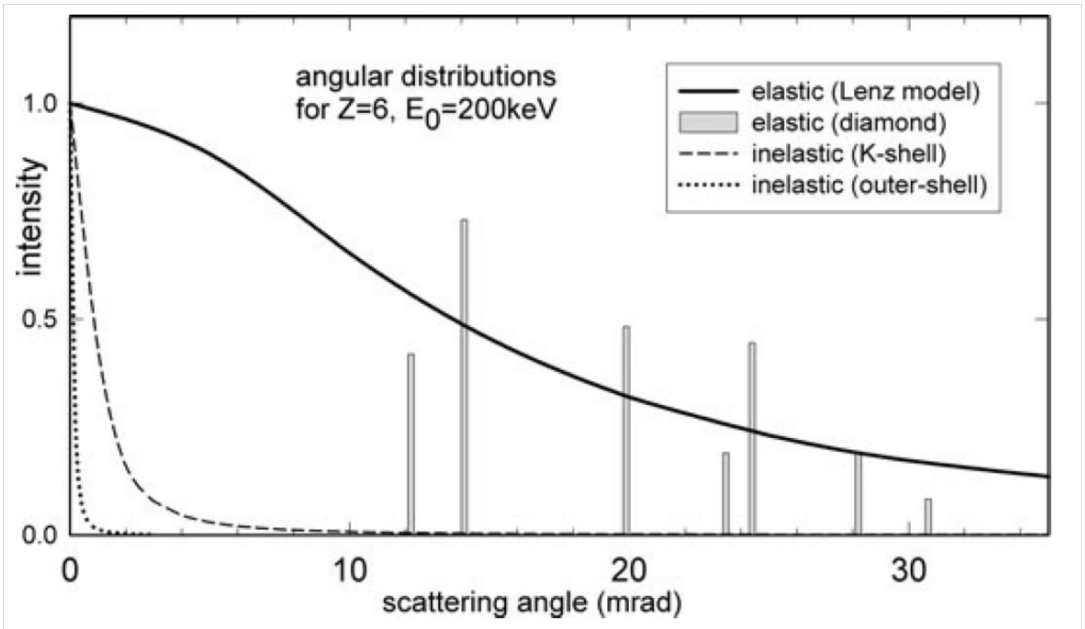

Figure 3.18: Elastic and inelastic angular distribution of scattered electrons from a single carbon atom (solid black curve) and the low order Bragg spots in diamond (peaks). The distribution of electrons inelastically scattered from the outer shell and K-shell electrons corresponding to energy losses of 35 and 300 eV respectively are shown by the dashed lines. Image from Egerton [118].

To measure the energy losses of the incident electrons, the BF annular detector is removed, allowing the unscattered and inelastically scattered electrons to pass

into a spectrometer situated at the bottom of the microscope where the electron energy is measured. The JEOL ARM200F was equipped with a Gatan Imaging Filter (GIF) Quantum, Figure 3.19.

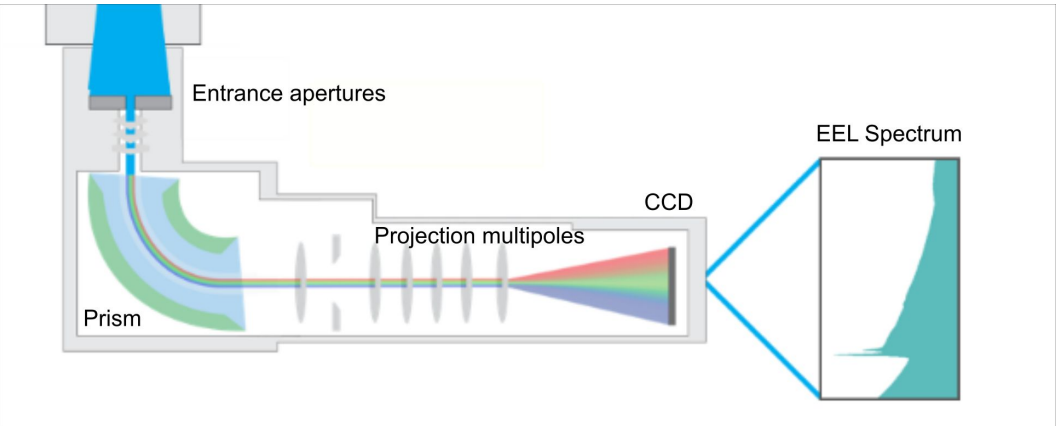

Figure 3.19: Schematic operation of the Gatan Quantum GIF. Electrons passing through the entrance aperture of the spectrometer are separated in energy using a magnetic prism, changing the trajectory of the electrons by 90°. An energy selecting slit can be inserted after the prism to enable energy filtered image to take place. Multipole lenses after the magnetic prism allows for either the energy spectrum or an energy filtered image to be projected onto the CCD detector [119].

The Electron Energy Loss Spectrum can be split into three components, the zero-loss peak (ZLP), low-loss and core-loss regions. The zero loss peak includes the electrons which haven't been scattered as they pass through the sample or electrons which have been scattered without any measurable energy loss. The energy resolution that can be achieved is dependent on the electron source of the microscope, which will accelerate the beam electrons within a small range of energies. The small range of acceleration energies can be indistinguishable from energy losses of that magnitude. The FWHM of the ZLP is typically used to define the energy resolution that can be achieved from the system and can assist in the alignment of the spectrometer. The ARM 200F used in this project for EELS measurements uses a Schottky FEG (Field Emission Gun) as the electron source, achieving a maximum energy resolution of about 0.9 - 1eV. Monochromators can reduce the energy spread of the electron beam, allowing vibrational EELS spectroscopy to be possible, with energy resolutions of the order of 10 meV being achieved [120,121].

The low-loss region of the EEL spectrum is defined as energy losses between 0 - 50 eV. This region of the spectrum includes losses due to either single or collective excitation of the valence (or outer shell) electrons, such as interband (band-gap)

transitions and plasmon losses respectively. Plasmon losses are the most prominent feature in the LL spectra of diamond, Fig. 3.20, produced by a collective oscillation of the outer shell electrons as the beam electrons travel through the sample. Since the low-loss region is attributed with the outer shell electrons, this region of the spectrum can be used to probe the optical and electronic properties of the material. The sample thickness can also be determined from the low-loss region from the ratio of the low-loss intensity to the ZLP intensity.

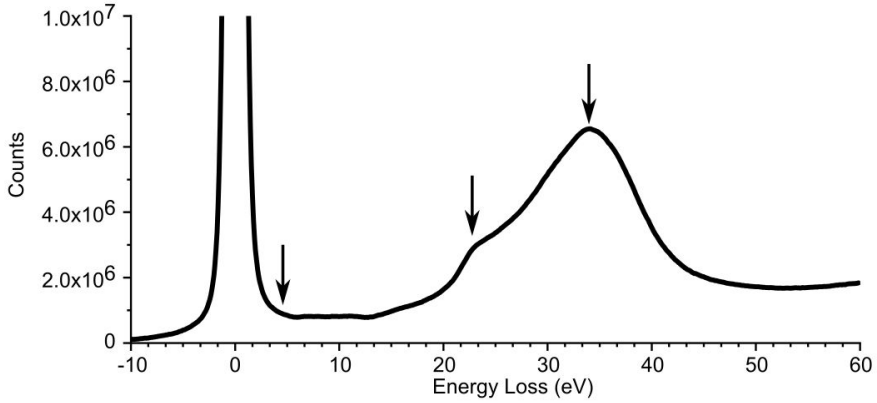

Figure 3.20: Low-loss EELS spectrum of diamond. Features highlighted are the band gap transition at 5.5eV (obscured by the tail of the ZLP), surface plasmon at approx. 21eV and the bulk plasmon at approx. 34 eV. Sample thickness approx. 100nm

The core-loss region of the EELS spectrum, energy losses > 50 eV, are attributed to interactions of the primary electron with inner shell electrons, causing their excitation into unoccupied states. The core-loss spectrum provides information about the chemical and bonding structure of the material. Different atoms have different ionisation energies and the energy loss near-edge structure (ELNES), losses within 50 eV of the ionisation edge onset, provides information about the local joint density of states, reflecting the local bonding configuration [118]. In anisotropic materials, different directions in the crystal will have different unoccupied density of states. Allowed transitions of the inner shell electrons into these unoccupied states, due to excitation from the fast electrons, will therefore cause changes in the shape of the core-loss edge for different crystal directions [118]. The shape of the carbon K-edge is different for amorphous carbon, parallel and perpendicular graphite, hexagonal and cubic diamond, as shown in Figure 3.21.

The differences in the shapes of the low-loss and core-loss spectra allow for the identification of different carbon phases using a "fingerprinting" method, by

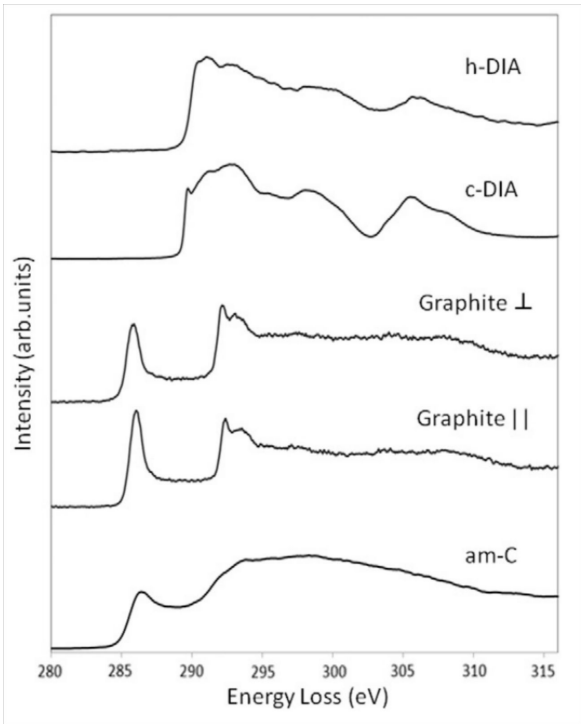

Figure 3.21: Core-loss EELS spectra for hexagonal and cubic diamond, parallel and perpendicular graphite and amorphous carbon [122].

comparing the EELS spectrum obtained with a database of EELS spectra from known phases of carbon.

In thicker samples, multiple scattering events can occur which will alter both the low-loss and core-loss spectra. Multiple plasmon peaks at integer values of the plasmon energy will be seen as the sample thickness increases, while electrons which underwent scattering from valence electrons, before then undergoing a core-loss scattering event, will change the shape of the core-loss edge. Deconvolution techniques can be used to correct the spectrum from the effects of plural scattering however this can introduce artefacts into the core-loss spectrum. For high resolution and accurate analysis of the core-loss edge fine structure, the sample thickness must be below one inelastic mean free path to reduce multiple scattering events. In diamond, the inelastic mean free path at 80 kV is 88 nm and at 200 kV is 112 nm [118].

Standard Spectrum Imaging (SI) methodology was used in the collection of EELS datasets. Data acquisition was carried out with a beam current of 75pA in a <0.1 nm probe, a convergence angle of 16 mrad and a collection angle of 25 mrad. Background subtraction, deconvolution and subsequent analysis was carried

out using routines in Gatan's Digital Micrograph software.

3.5 Sample Preparation

3.5.1 Focussed Ion Beam (FIB) Sample Preparation

TEM lamellae were prepared from bulk stones, (A630-09-01/02/03), using standard FIB lift out methodology on a JEOL 4500 FIB-SEM, and later, on an FEI Versa and Scios Dual Beam FIB. All of the FIBs utilised Gallium ions to mill the samples. Cathodoluminescence imaging of the bulk sample prior to any FIB lift-outs identified areas of potential interest for TEM imaging, such as grain boundaries. The bulk samples were provided as cubes with faces of $\{100\}$ orientation. To achieve a $\langle 110 \rangle$ TEM sample orientation, FIB lift-outs were taken with the lamella at a 45° angle to the cube edges.

Firstly, a protective layer, approx. 2 μm $\times$ 20 μm $\times$ 2 - 3 μm (width $\times$ length $\times$ height), was deposited at the area of interest to protect the surface from any damage from the ion beam. The JEOL 4500 FIB-SEM was equipped with carbon gas injectors while the FEI Versa and Scios were both equipped with Pt injectors to provide the protective layer.

Using a 30 kV Ga ion beam, trenches of approx 10 μm depth were milled on either side of the protective layer and the lamella was thinned to approx 1 - 1.5 μm. The TEM lamella was then extracted from the surface and attached to a copper TEM grid where final thinning was performed. The lamella was then thinned with the ion beam at an angle of approx 1.5 - 2° on either side of the sample surface until the sample was electron transparent. To reduce ion beam induced damage to the sample surface, the thinning was carried out in stages with progressively reduced accelerating voltage with a final polishing stage at 5 kV. Final thinning was carried out using a short time, $\sim$ 30 s, to prevent surface steps being formed in the lamella surface. The final size of the lamellae extracted from the sample measured approximately 10 μm (length) $\times$ 5 - 6 μm (depth) $\times$ 100 nm (thickness).

3.5.2 Argon Ion Milling Sample Preparation

Preparation of the A628 diamond series into electron transparent TEM samples was carried out by argon ion milling in a Gatan Precision Ion Polishing System (PIPS). Final low energy surface cleaning steps took place in a newer Gatan PIPS II. The A628 series of diamonds were prepared as plates with dimensions (2 mm $\times$ 2 mm $\times$ 50 μm) by Element 6 and De Beers Technology UK. The diamond plate was mounted

on a stub holder using wax and ion milled at an angle of + 5° using both guns at 5 kV accelerating voltage for 3 hours. The sample was then dismounted from the stub, flipped, and mounted on a Cu TEM grid (containing a 1.5 mm circular hole) with wax. The Cu grid with the diamond plate was then placed in the PIPS using a Gatan Duopost® sample holder and milled at the same settings until perforation. Large areas of electron transparent material, up to 100 μm away from the perforation was produced using this method. This technique typically left behind Cu deposits from the TEM grid on the surface of the diamond so final cleaning stages at lower kV and angle were used. A first cleaning step of 3 kV beam energy using both ion guns at angles of + 3.5° and - 3.5° for 20 minutes was used before a final cleaning stage at 1 kV, ± 3.5° and 10 - 30 minutes duration. This final cleaning step was found to achieve much smoother samples with fewer thickness variations.

The final specimen was found to be far superior to that produced by FIB preparation. The thin electron transparent region was found to be several 10's of μm in size, allowing for larger areas of dislocation structure to be examined. Thickness of less than 30 nm could be achieved near the edge of the perforation, although this material at the edge appeared to be more amorphous in nature, possibly due to surface damage.

3.6 Diamond Samples

A variety of untreated and treated type IIa natural brown diamond samples, which had been plastically deformed by nature, were studied in this project. By selecting type IIa diamond, the nitrogen-related defects within the material are minimised. Details of their colour, type, treatment and the TEM sample preparation used can be found in table 3.1.

The type IIa diamonds (A630 series) were provided as cubes of approx. 0.5 - 2 mm in size, with TEM lamella being prepared by Focussed Ion Beam (FIB) milling. The type IIa "zebra" diamonds (A628 series), containing both colourless and brown bands, were prepared by De Beers and Element 6 into thin plates, size 2mm × 2mm × 50μm. A628-09-07-a was provided as a larger offcut of material from the preparation of the plates. The plates were prepared to this specification to facilitate thinning by argon ion milling, which was found to produce better electron transparent samples than FIB. Both of these sample preparation techniques will be discussed later in sections 3.5.1 and 3.5.2. All electron transparent specimen were prepared looking along a $\langle 110 \rangle$ zone axis with a thickness ideally below 100nm.

To ensure a clean surface for optical, SEM and CL imaging, samples were

Table 3.1: Type IIa diamond samples examined, their colour, treatment and TEM sample preparation,

Name	Colour	Treatment	Prep
A628-09-02-a	colourless (former brown bands)	2000° C : 12hr	None
A628-09-02-b	colourless (former brown bands)	2000° C : 12hr	Argon Ion Milling
A628-09-06	brown and colourless bands	Untreated	Argon Ion Milling
A628-09-07-a	brown and colourless bands	Untreated	None
A630-09-02	colourless (originally brown)	2300° C : 1hr	FIB
A630-09-03	brown	Untreated	FIB

cleaned using a standard acid oxidation treatment. This treatment will be discussed in more detail in section 6.2.3.

Chapter 4

Point Defect Generation in Diamond by Plastic Deformation and the Climb of the 90° Partial Dislocation

4.1 Introduction

PAS measures significant concentrations of monovacancies ($\approx 10^{18}$cm^{-3}), and vacancy clusters ($\approx 10^{15}$cm^{-3}) in brown diamond [30], which are not seen in naturally colourless diamond. At elevated temperatures, where the vacancy is free to move, vacancies present in the lattice are thought to aggregate together into vacancy clusters. To fully understand how the brown colouration is formed in diamond, a detailed investigation into the origin of intrinsic point defects and their behaviour is needed. This chapter briefly reviews relevant intrinsic point defect properties and the generation of intrinsic point defects by interacting dislocations, before discussing the results in later sections.

Using the formation energies of interstitials ($E_i{}^f \approx 12$ eV) and vacancies ($E_v{}^f \approx 6$ to 7 eV. [61,70,78,81,123]) in diamond, see section 2.1.1, the expected interstitial and vacancy concentrations at thermodynamic equilibrium can be determined by an Arrhenius law of the form [66]:

$$c_p = n_p \exp(\frac{E_p^f}{k_B T}), \tag{4.1}$$

where n_p is the density of possible point defect p sites per unit cell, $E_p{}^f$ is the

formation energy of p, k_B is Boltzmanns constant and T is absolute temperature. The thermodynamic equilibrium concentrations calculated by Eq. 4.1 are shown in Figure 4.1. At the temperatures that lithospheric diamond experiences in the mantle, between 900 - 1400°C,[50,56], the expected thermodynamic equilibrium concentration should be orders of magnitude less than that measured by PAS, Figure 4.1. The vacancies measured in brown diamond must therefore be generated under non-thermodynamic equilibrium conditions.

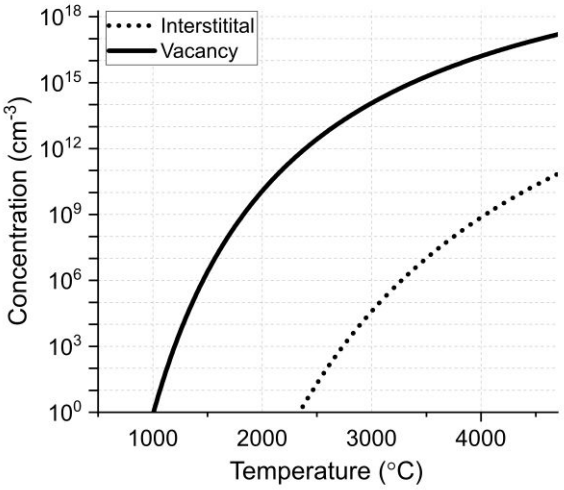

Figure 4.1: Thermodynamic equilibrium concentration of interstitials and vacancies in diamond, determined from Eq. 4.1.

All brown diamonds are found to have experienced plastic deformation at some point in their history[26], with the appearance of slip bands usually indicating deformation has occurred. Point defects, either interstitials or vacancies, can be produced during plastic deformation when mobile dislocations pass through a "forest" of pre-existing dislocations[124,125]. Dislocations which lie on different glide planes to the moving dislocations are termed forest dislocations. Named so due to the visual similarity to trees (dislocations) stretching vertically from the forest floor (glide plane). A review into the literature of point defect generation by interacting dislocations is given in section 4.1.1. Point defect generation by this mechanism have often been studied using ductile metals, such as Cu and Al, where plastic deformation can occur over a wide range of temperatures (including at temperatures as low as 4K)[126–128]. Low temperature deformations freeze in point defect supersaturations, allowing these processes and point defect migration to be investigated[125,128–130].

Large point defect supersaturations can be produced by deformation since the formation energy of interstitials and vacancies is small in comparison with the energy

released by a moving dislocation in a stressed crystal. Once they are produced, vacancies and interstitials generally behave in quite different ways due to their very different formation and migration energies. As seen in Figure 4.1, the large difference in interstitial and vacancy formation energies mean that, under thermodynamic equilibrium conditions, the concentration of interstitials is much lower than that of vacancies.

A second important difference is that the energy barrier for thermally activated diffusion is lower for interstitials, meaning that they form clusters or condense onto a suitable sink much quicker and at lower temperatures than for vacancies. The lower migration energy of the interstitial, ${E_i}^m \approx 1.6$ eV, compared to the vacancy, ${E_v}^m \approx 2.3$ eV, means significant migration occurs at lower temperatures, > 330 °C compared to > 600 °C respectively[61,70,78,81,123]. The interstitials are therefore far more mobile than the vacancy and will be frozen in at lower temperatures. The high temperatures, > 900°C, required for the plastic deformation of diamond means that both interstitials and vacancies will be mobile following their generation. To establish thermodynamic equilibrium concentrations, the interstitials and vacancies will migrate and either be trapped at sinks, such as at dislocations, grain boundaries or the surface, or form clusters.

In this chapter, the generation of point defects by plastic deformation will be examined in detail. Rather than find evidence of significant vacancy generation and vacancy clustering, as expected for a brown diamond, it is found that large numbers of interstitials have been generated by plastic deformation and have condensed onto the 90° partial dislocations. Vacancy generation is still expected but is not detected by electron microscopy techniques.

4.1.1 Generation of Point Defects by Plastic Deformation

The mechanism of point defect emission during plastic deformation is shown in Fig. 4.2, following Amelinckx[126]. Two screw dislocations D1 and D2 are shown, with Burgers vector $\mathbf{b_1}$ and $\mathbf{b_2}$ respectively. D1 moves to the right on its glide plane, approaching D2 (Fig. 4.2 (a)) and then passes through it (Fig. 4.2 (b)). In doing so a jog is introduced in both dislocations; a jog of size $\mathbf{b_1}$ is produced in D2, and one of size $\mathbf{b_2}$ is produced in D1. These jogs can be sessile, in which case they can only move by emission or absorption of point defects. In Fig. 4.2 (b) the jog in D1 acts as an anchor, and as D1 moves onwards it leaves behind a dipole, since the upper and lower arms attached to the jog now lie on parallel glide planes separated by $\mathbf{b_2}$ and cannot meet by glide. The attractive force between these two arms is large, since they both have opposite signs and are separated only by a single lattice

translation. It is energetically favourable for them to recombine and in doing so, emit point defects. Fig. 4.2 (c) shows the final situation where the dipole has "evaporated" by emission of point defects, in this case vacancies. Dissociation of dislocations into partials[97] does not change the total Burgers vector or the size of the jog produced when one dislocation passes through another. Interstitials are emitted by similar configurations with reversed Burgers vector or line direction of one of the dislocations. It should therefore be expected that both vacancies and interstitials are produced in plastic deformation, since the type of point defect is determined primarily by geometry[98,130].

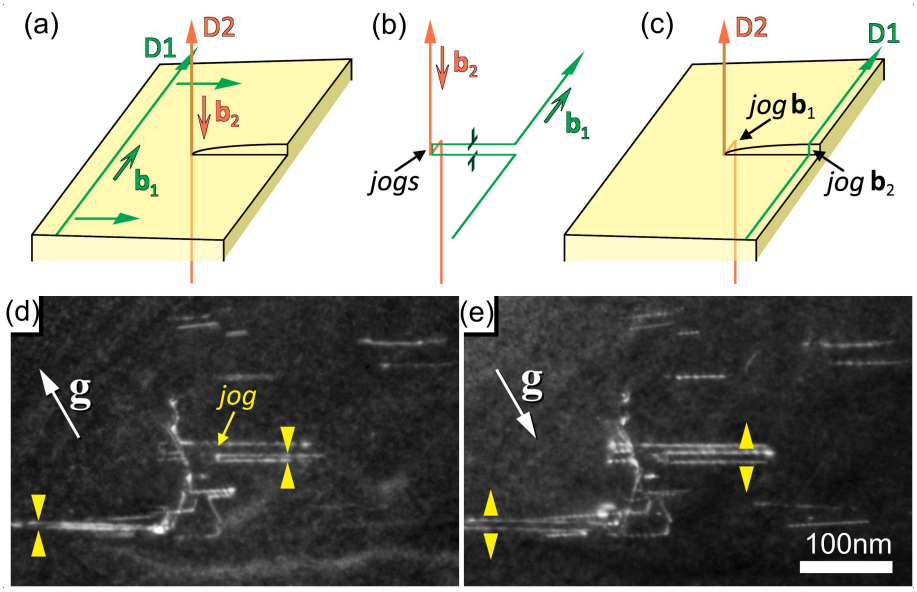

Figure 4.2: Schematic showing the formation of intrinsic point defects by the interaction of two dislocations. a) Dislocation D1 (green) lies in screw orientation with Burgers vector $\mathbf{b_1}$ and glides to the right on the plane shown, approaching dislocation D2 (orange), which cuts through the glide plane and has a screw component perpendicular to it $\mathbf{b_2}$. b) Once D1 passes through D2, both dislocations have a sessile jog, each with a size corresponding to the screw component of the Burgers vector of the other dislocation. As D1 moves to the right a dipole forms, anchored by the jog. c) the dipole in D1 can shrink by movement of the jog, in this case by emission of vacancies. After Amelinckx[126]. d) and e) dark field weak beam g3g = 220 TEM images of a dislocation dipole ending at a jog in a natural type IIa diamond with slight brown coloration. The bright line is displaced from the actual position of the dislocation, depending upon the local bending of the diffracting planes close to the dislocation core. The change in apparent separation of the pair of dislocations as g is reversed, indicated by the yellow arrowheads, indicate that they form a dipole.[131]

As seen in Section 2.2.1, dislocations in diamond are of the $1/2\langle 110\rangle$ type. For a dislocation D_1 with Burgers vector, $\mathbf{b_1}$, lying in a specific $\{111\}$ glide plane, the Burgers vector, $\mathbf{b_2}$, of the dislocation D_2 must have a component perpendicular to this $\{111\}$ plane in order to produce a jog. Section 2.2.6 reviews the dislocation reaction products between two dislocations in an fcc material. The interaction of two 60° dislocations which lie on different $\{111\}$ glide planes will therefore be able to produce a jog (with normal parallel to $\mathbf{b_2}\times\mathbf{b_1}$). The jog can move conservatively, without emitting point defects, along the $\langle 110\rangle$ direction that is the intersection of these two $\{111\}$ planes. Conversely, perpendicular to this $\langle 110\rangle$ direction, point defects must be produced to move D1 by a lattice translation vector. (In a simple fcc crystal this would be a single point defect; in diamond it is two.) The number of point defects emitted N by a moving jog is given by [126,132]

$$N = \frac{\vec{\mathbf{v}}\cdot(\mathbf{u_2}\times\mathbf{u_1})}{|\vec{\mathbf{v}}\cdot(\mathbf{u_2}\times\mathbf{u_1})|}[\vec{\mathbf{v}}\cdot(\mathbf{b_2}\times\mathbf{b_1})]\frac{L}{8a} \tag{4.2}$$

Where $\vec{\mathbf{v}}$ is a unit vector along the direction of motion for D1, L is the distance D1 has travelled from the intersection, a is the lattice parameter, and $\mathbf{u_1}$, $\mathbf{u_2}$ are the dislocation line directions (following the finish-start/right-hand (FS/RH) convention).

The density of point defects produced by deformation is not only related to the plastic strain that the crystal experiences but also depends on the density of forest dislocations. Crucially, the active slip system must pass through pre-existing forest dislocations [125,127]. The dislocation D2 in Fig. 4.2 is such a forest dislocation, obstructing the slip of D1. The dislocations running vertically in Figs. 4.2 (d) and 4.2 (e) could also be forest dislocations. The link between point defects generated this way and brown colouration is reinforced by the observation that the colouration is stronger when multiple slip systems operate simultaneously during deformation of synthetic diamond [63]. The total length of dragged jogs per unit volume λ, when a glissile array of dislocations producing plastic strain ϵ passes through an array of forest dislocations with density ρ is:

$$\lambda = \frac{\rho\epsilon}{4b}, \tag{4.3}$$

Taking into account that half of the interactions produce no jogs. The concentration of point defects per unit volume produced by plastic strain is therefore:

$$C = \frac{\vec{\mathbf{v}}\cdot(\mathbf{u_2}\times\mathbf{u_1})}{|\vec{\mathbf{v}}\cdot(\mathbf{u_2}\times\mathbf{u_1})|}[\vec{\mathbf{v}}\cdot(\mathbf{b_2}\times\mathbf{b_1})]\frac{\rho\epsilon}{32ab}, \tag{4.4}$$

which is shown in Figure 4.3 for different forest dislocation densities. A forest dislocation density of 10^9 cm^{-2} and a plastic strain of 1% can generate $\sim 10^{20}$ point defects cm^{-3}.

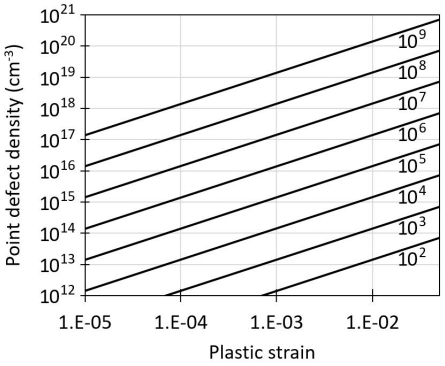

Figure 4.3: Point defect concentrations generated during plastic deformation of diamond from Eq. 4.4. Each line corresponds to a different forest dislocation density, from 10^2 cm^{-2} to 10^9 cm^{-2}.

Although this calculation predicts point defect concentrations significantly larger than the vacancy concentrations of 10^{18} cm^{-3} measured by PAS[30], Eq. 4.4 will likely overestimate the number of point defects generated. Dislocations gliding through the crystal during plastic deformation may meet bundles of forest dislocations as well as single defects. If D2 is replaced in Fig. 4.2 by several forest dislocations that are too close together to allow the dislocation to pass between them[125], the jog produced in D1 will be larger. The height of the dipole in Fig. 4.2 (b) will be correspondingly larger and the driving force for recombination is reduced. Beyond a certain height the attractive force will not be sufficiently high to cause dipole annihilation, point defects will not be generated and the dipole will remain stable. A large majority of the jogs created by forest interactions may not produce point defects since the dipoles they produce are too widely spaced. Dislocation dipoles are commonly observed in deformed fcc materials[127,128,133,134], as well as chains of dislocation loops condensed from point defects produced by dipole collapse[135]. The latter has not been observed in diamond, but large numbers of dislocation dipoles are. An example of a dipole terminated by a jog in brown type IIa diamond is shown in the dark field weak-beam TEM images Figs. 4.2 (d) and 4.2 (e). Dislocation dipoles can easily be identified from their inside-outside contrast, the change in the apparent spacing of their constituent dislocations when the diffraction vector is reversed[131], as shown by the yellow arrowheads. The jog is dissociated, with a faint loop visible to the left of the arrow. The limited resolution of weak-beam dark field TEM imaging means direct evidence of point defects is

absent from these images. In order to study this aspect further, atomic resolution imaging is necessary.

4.2 Results

4.2.1 Spectroscopy and Low Magnification Imaging

Photoluminescence spectroscopy of the untreated stone, A630-09-03, shows broad band-A luminescence centred at $\sim$ 430nm, and a small concentration of the H3, N3 and GR1 neutral vacancy centres, Fig 4.4. The H3 and N3 centres are common defects in natural diamond. The origin of the band-A emission is unknown but has been associated with sp^2 carbon at dislocations and grain boundaries[136]. PL spectroscopy is a much more sensitive technique for detecting defects than FTIR spectroscopy and, despite the detection of nitrogen containing centres in the diamond, the concentration is below the detection limit of FTIR spectroscopy[137] ($<$ 1ppm) confirming this stone as a type II diamond. The large width of the GR1 line may indicate large strains in the vicinity of the vacancies[38], from point defects, dislocations or other extended defects.

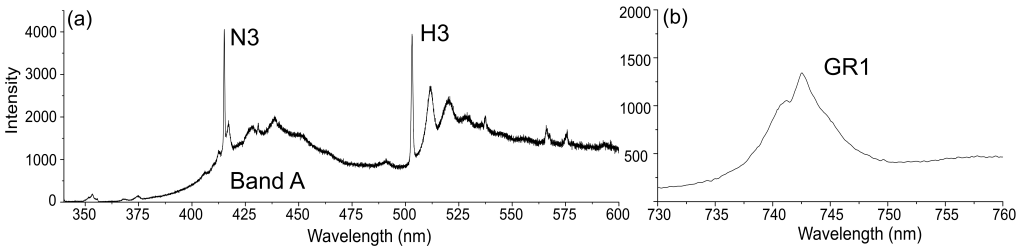

Figure 4.4: PL spectra taken of the untreated brown type IIa diamond sample, A630-09-03, showing the presence of N3, H3 and GR1 defect centres. Spectra obtained at liquid nitrogen cooled temperatures. Laser excitation wavelength of 325nm used for spectrum (a) and 660nm used for (b).

EBSD and Optical Imaging provides clear evidence that the diamond has undergone significant amounts of plastic deformation. Figure 4.5 (a) shows an optical image of one of the {001} faces of the untreated stone. Optically, the diamond appears to have a light brown colour throughout the stone with a few bands of heavier brown colouration. The bands are several hundred μm wide at angle of $45° \pm 10°$ to the crystal face. These bands can be seen more clearly in the EBSD map, Figure 4.5 (b), where undulating strands of material with a similar orientation (misorientation

<2°) can be seen. The bands are consistent with the intersection of a {111} glide system with the polished crystal surface and are similar in appearance to slip bands seen in heavily deformed fcc metals [128].

Strong band A luminescence is observed by CL with panchromatic images revealing a cellular network of sub-grain boundaries, Figure 4.5 (c), several μm in size, with a lower density of individual end-on dislocations ($\sim 1\times 10^{8}$ cm^{-2}) within the cells, Figure 4.5 (d). The band A emission is strongest around the sub-grain boundaries with an intensity that decays over several microns. The grain boundaries and dislocations appear to be non-radiative recombination centres, as seen from the dark contrast in the images.

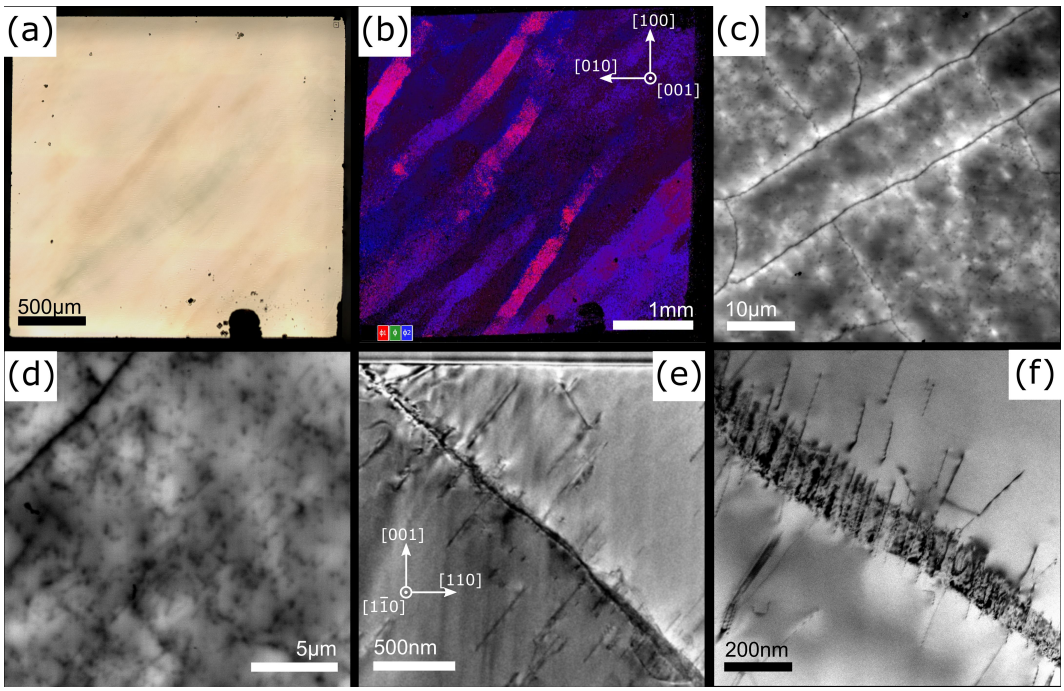

Figure 4.5: Microstructure of the untreated stone, A630-09-03, used in this study. a) Optical image of the (001) surface showing the brown colouration with some colouration showing banding (edges of the image are parallel to 100). b) EBSD orientation map of the same surface showing a banded structure. c) Room temperature panchromatic CL at 5kV incident electron beam energy showing bright luminescence around sub-grain boundaries and patchy luminescence between; d) Panchromatic CL image (-168 °C) between the sub-grain boundaries showing dark spots corresponding to individual dislocations; e) Cross section TEM image of a sub-grain boundary and straight dislocations. Surface of the sample is towards the top of the image. f) The same boundary imaged using the [$\bar{2}$02] diffraction condition showing the high density of dislocations.

Cross section TEM lamellae taken parallel to {110} show the sub-grain boundaries to be inclined to the crystal surface, with a tendency to lie roughly on {111} planes (Fig. 4.5 (e)). Imaging using a $[\bar{2}02]$ diffraction condition reveals that the sub-grain boundary is composed of lots of closely spaced straight dislocations of similar line direction, Figure 4.5 (f).

Dipoles with $\langle 110 \rangle$ line directions are observed close to the low angle sub-grain boundaries. These sub-grain boundaries appear to take the role of forest dislocations, with dislocations passing through this tangled wall of dislocations forming the dipoles and jogs by the mechanism discussed in sections 4.1.1. Using aberration corrected-STEM, the atomic structure of several dissociated dislocations and dipoles in the vicinity of sub-grain boundaries were imaged.

4.2.2 STEM Imaging of Dissociated Dislocations

An ADF-STEM image of a dissociated 60° dislocation in the untreated stone, A630-09-03, can be seen in Figure 4.6 (a). Drawing a Burgers circuit around each partial, the Burgers vector was determined. The method to calculate the Burgers vector from the ADF-STEM images is described in more detail in Sanchez et al. (2018) [138]. Burgers vector components parallel to the beam direction could not be determined, but for definiteness these components were chosen to point out of the image, i.e. the Burgers vector is $\mathbf{b} = \frac{1}{2}[01\bar{1}]$, with the line direction defined pointing into the image. A schematic of the dissociated dislocation structure seen in Figure 4.6 (a) can be seen in Figure 4.6 (d). The intrinsic stacking fault is highlighted by green atoms, while the 30° partial dislocation at the bottom end of the stacking fault is highlighted in red, with $\mathbf{b} = \frac{1}{6}[\bar{1}2\bar{1}]$. The stacking fault is 2.40 nm wide, in agreement with measurements of dissociation widths obtained using weak-beam dark field TEM [97]. The structure of the 90° partial at the upper end of the stacking fault is different from that expected by DFT, section 2.2.3. An additional half plane of atoms appears to have formed between the (111) planes, with one side of the extra plane attached to the 90° partial, forming an obtuse angle with the stacking fault. The type IIa nature of the diamond (low impurity concentration) means the structure observed in Figure 4.6 (a) has formed by the condensation of interstitial carbon atoms onto the 90° partial dislocation, moving the 90° partial out of the glide plane by approx. six lattice translations, highlighted in dark blue in Fig. 4.6 (d). The atom columns of the climbed section are blurred and indistinct, indicating that the structure varies along the electron beam path through the thin lamella.

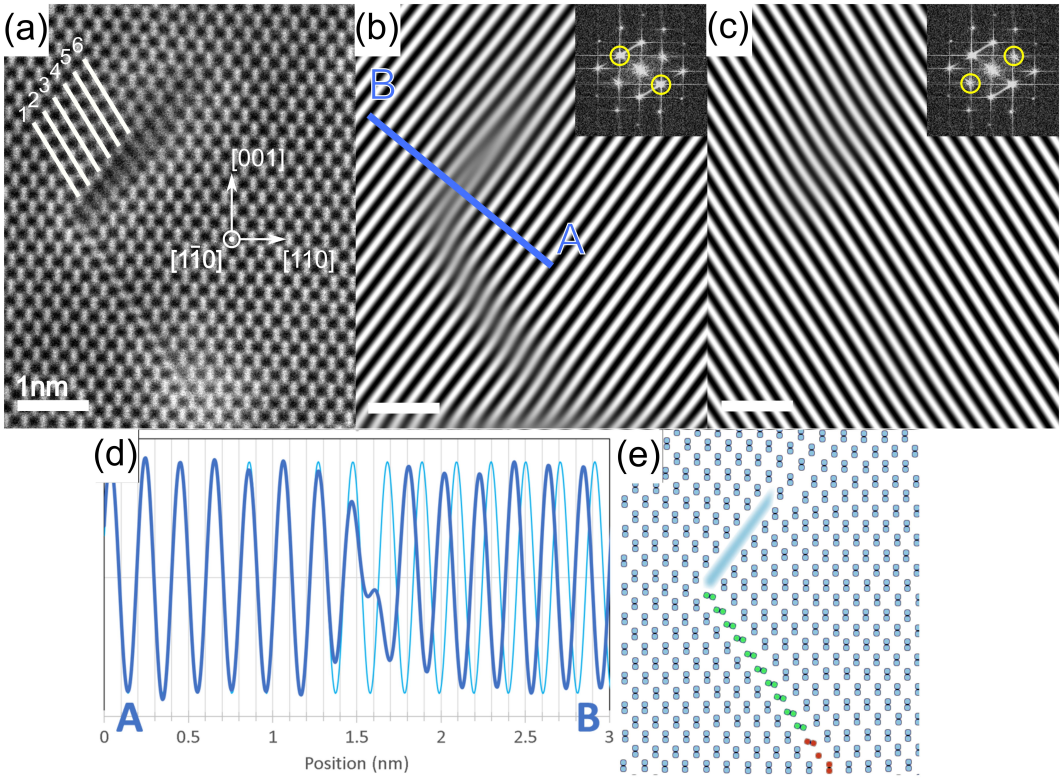

Figure 4.6: (a) ADF-STEM image of a dissociated $\frac{1}{2}[01\bar{1}]$ dislocation in an untreated brown diamond, in the vicinity of the low angle grain boundary shown in Figure 4.5 (e/f), with a 90° partial that has climbed by addition of interstitial atoms over approximately 6 lattice planes. (b) Fourier filtered image showing the $(11\bar{1})$ planes. Inset shows the FFT of (a) and spots used to produce the Fourier fringe image. (c) Fourier filtered image showing the (111) planes. Inset shows the FFT of (a) and spots used to produce the Fourier fringe image. (d) intensity plot of Fourier fringes along A-B (dark blue) and extrapolated fringes from perfect lattice (light blue) showing that there is a shift of one third of the lattice period across the climbed fault; (e) schematic of the defect highlighting the 30° partial dislocation with Burgers vector $\frac{1}{6}[\bar{1}2\bar{1}]$(red) bounding an intrinsic stacking fault (green) , and climbed 90° partial (dark blue).

Fourier analysis (Figs. 4.6 (b) and (c)) of the (111) planes perpendicular to the climb direction shows an expansion of only one third (0.33 ± 0.01) of a plane spacing. The component of the fault vector is therefore $\frac{1}{9}[11\bar{1}]$ in the plane of the image. This displacement is only a half of the value that would be expected for a prismatic loop, indicating the additional layer is, at most, only one atom thick

rather than a complete bilayer. The Fourier fringes parallel to the direction of climb appear to show no shear of the planes, Figure 4.6 (c), indicating that the stacking sequence in maintained on either side of the extra plane.

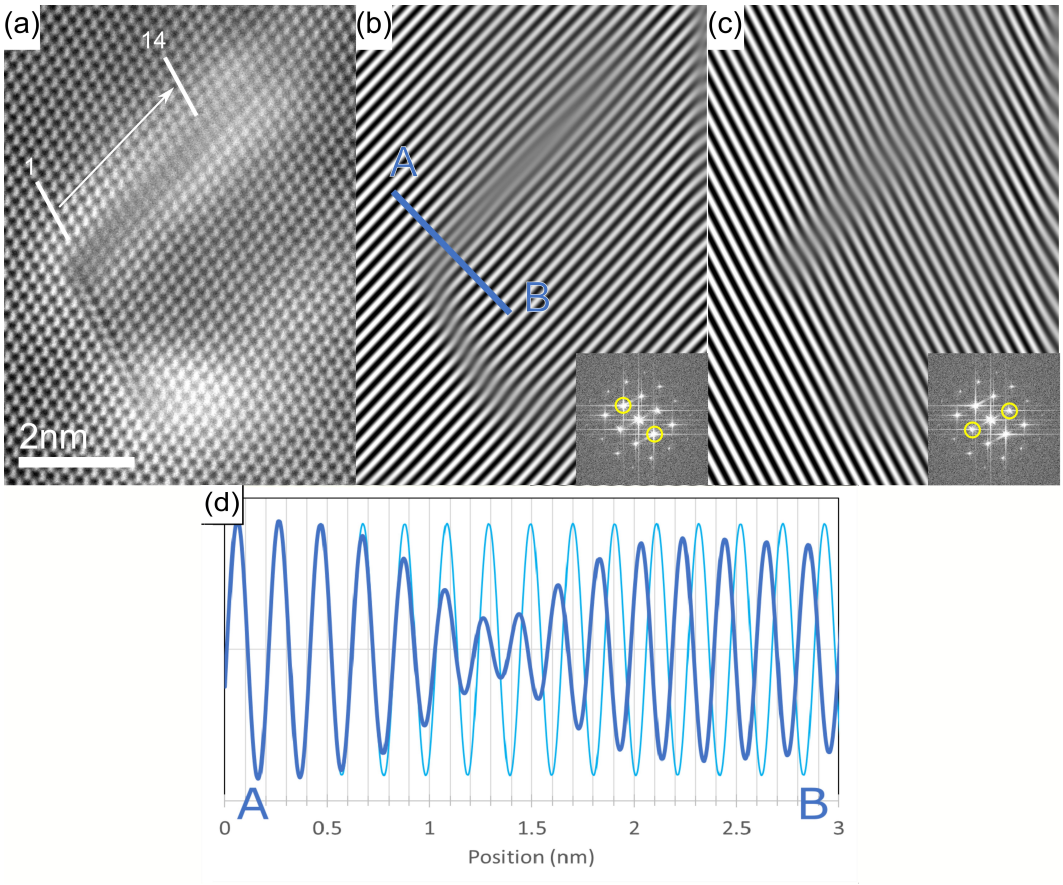

Figure 4.7: (a) ADF STEM image of a dissociated $\frac{1}{2}[01\bar{1}]$ dislocation in the HPHT treated brown diamond, A630-09-02. The 90° partial has climbed by addition of interstitial atoms over approximately 14 lattice planes. (b) Fourier filtered image showing the $(11\bar{1})$ planes. Inset shows the FFT of (a) and spots used to produce the Fourier fringe image. (c) Fourier filtered image showing the (111) planes. Inset shows the FFT of (a) and spots used to produce the Fourier fringe image. (d) Intensity plot of Fourier fringes along A-B (dark blue) and extrapolated fringes from perfect lattice (light blue). A phase shift of 0.38 between the actual Fourier fringes and extrapolated fringes is observed across the climbed fault.

This distinctive micro-structure was found for all dissociated dislocations observed by atomic resolution ADF-STEM, with only interstitial climb being observed.

Climb by vacancy absorption would cause climb on the same (111) plane but on the other side of the stacking fault, and the climbed section would form an acute angle with the stacking fault [139].

A second example, from HPHT-treated sample A630-09-02, is shown in Fig. 4.7. Here more climb has taken place, roughly 14 lattice translations, and the thickness of the climbed region is slightly larger at 0.38 ± 0.01 of a $(11\bar{1})$ plane spacing, Figure 4.7.

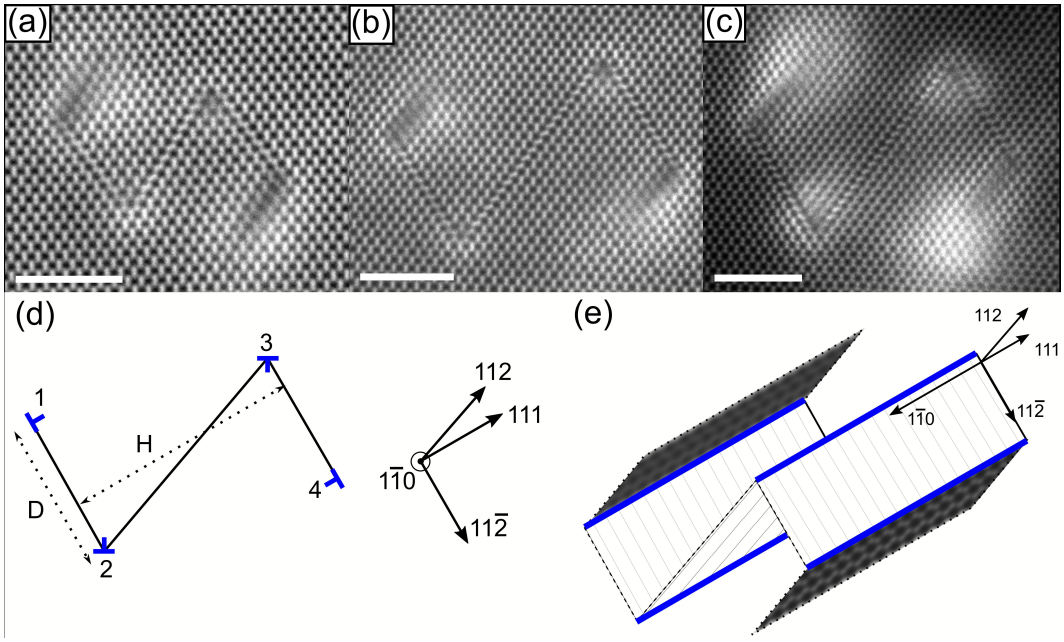

Figure 4.8: (a, b, c) ADF-STEM images of z-type faulted dipoles in an A630-09-03 showing interstitial climb of the 90° partial. Scale bars are 2 nm. (d) Schematic showing the structure of an ordinary z-type faulted dipole. Partial dislocations 1 and 4 are 90° partial dislocations. Partial dislocations 2 and 3 are stair-rod partial dislocations. (e) 3D schematic of the faulted dipoles shown in (a),(b) and (c), showing climb of the 90° partial.

Z-type faulted dislocation dipoles in the untreated sample, Figure 4.8 (a,b,c), also show climb of the 90° partial dislocation. Z-type faulted dipoles are composed of two 90° partial dislocations, two stair-rod partial dislocations and three intrinsic stacking faults. A schematic of the z-type faulted dipole structure can be seen in Figure 4.8. All of the dipoles have absorbed interstitial atoms onto the 90° Shockley partial dislocations, with climb occurring over 5 - 9 glide planes. The dipoles in Figure 4.8 (a) and (b) shows expansion of $\sim$ 0.44 of a $(11\bar{1})$ plane spacing, while the width of the climbed section in Figure 4.8 (c) shows an expansion of $\sim$ 1.1 of a

$(11\bar{1})$ plane spacing, which would indicate the formation of a full extra plane. Close inspection of Figure 4.8 (c) shows that the atom columns of the climbed section are more clearly resolved. Additional absorption of interstitials appears to have occurred on the top right most stair-rod partial dislocation, Figure 4.8 (c), causing expansion around the stacking fault. Equal amounts of climb are observed on both the 90° partials of each faulted dipole, suggesting that the local interstitial concentration varies on length scales larger than the size of the dipole.

Based on the STEM images of the climbed dissociated dislocations, it is possible to estimate the concentration of interstitial atoms absorbed onto the partials using the equation:

$$C_{int} = R\rho n \tag{4.5}$$

where R is the number of atoms absorbed per unit length of dislocation line for the climb of one glide plane, ρ is the dislocation line density and n is the number of glide planes climbed. Dislocation climb in which just one interstitial atom is accommodated per periodic unit along the dislocation core requires R $\sim 4 \times 10^7$ atoms cm^{-1} of dislocation length. Diamond has a two atom basis, so the formation of a full {111} plane requires two interstitials to be absorbed per periodic unit per glide plane, giving R $\sim 8 \times 10^7$ atoms cm^{-1}. Dislocation densities of $\sim 10^9$ cm^{-2} have been measured in similar brown type IIa diamond [18,31], using this value and observing that climb of between five and twenty glide planes has occurred, gives an absorbed interstitial concentration of 10^{17} to 10^{19} cm^{-3}.

4.2.3 Other Interstitial Related Defects

In the type IIa diamond examined here, the climbed 90° partial dislocations are the most commonly observed evidence that large numbers of interstitials have been generated. On rare occurrences, other interstitial related defect have also been observed. Nitrogen containing diamonds are typically found to contain {100} platelets. ac-STEM imaging was able to recently determine the structure of the platelets for the first time [62], resolving a decades long argument. Although the platelet is mainly found in type I diamond, it is composed mainly of interstitial carbon and the presence of any nitrogen in the structure is adventitious [62]. The presence of nitrogen does seem to be necessary for the production of the platelet [62] however, with very few platelets being observed in type II diamond. One small platelet has been observed in the type IIa diamond observed, Figure 4.9.

The interstitial carbon atoms that form the platelet are thought to be gen-

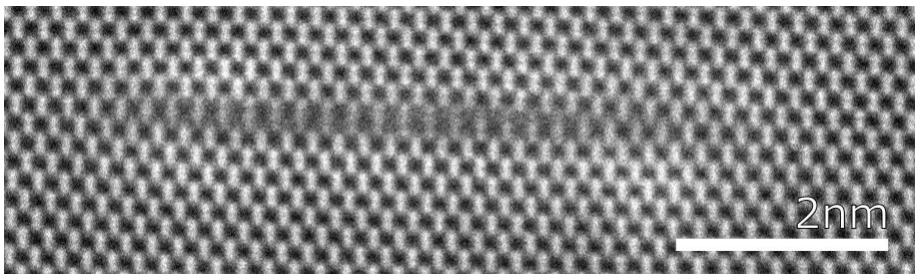

Figure 4.9: Small platelet observed in type IIa diamond, measuring about 4nm in length

erated during the formation of the B-centre, where the 4 nitrogen atoms eject an interstitial carbon atom as they aggregate. The low nitrogen concentration and undetectable level of B-centre mean the {100} platelet is unlikely to form in large numbers in this sample. Given estimates of the interstitial concentration generated by plastic deformation, it seems unlikely that this platelet has been the result of plastic deformation. If the interstitials generated by plastic deformation could form the platelets, far more platelets would be expected. Despite the large numbers of interstitials thought to be generated during deformation, the lack of platelets observed would indicate that the vast majority of interstitials generated are condensed onto the 90° partials, rather than forming other defects. Although rare in this type IIa diamond, with only one being observed, this defect is additional evidence of interstitial generation. Another interstitial related defect observed is the {113} defect, Figure 4.10.

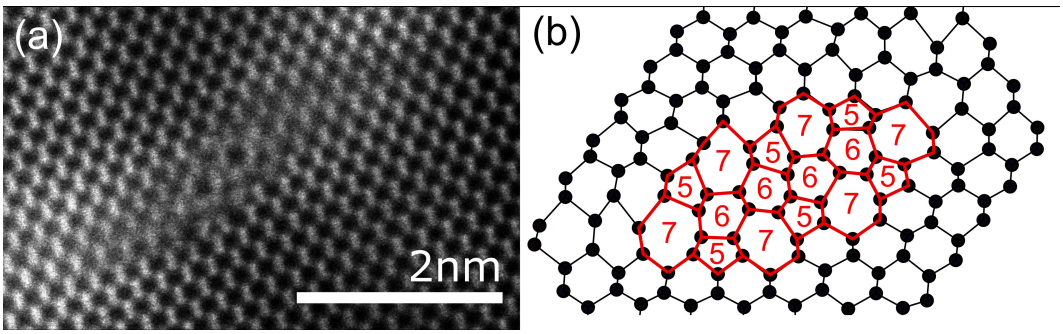

Figure 4.10: (a) {113} defect observed in diamond. (b) Proposed atomic structure based on (a) and the {113} defect structures modelled in Si and Ge.

The core of the defect in Figure 4.10 is blurred meaning it is difficult to accurately determine the core atomic structure, however the long axis appears to lie along a {113} plane with a line direction of ⟨110⟩, consistent with the {113}

defect observed in both silicon and germanium [61,140,141]. DFT modelling of the {113} defect structure in both Si and Ge appear to be a good visual match for parts of the defect structure [140,141], differences may be due to a defective core, possibly caused by an unstable structure, or as variations along the line direction of the defect. At each end of the long axis, the dumbbells appear stretched along a {001} direction, similar to the platelet, suggesting that conversion from a {113} defect to platelet could be occurring. The {113} defect is the most common interstitial aggregate defect in both silicon and germanium, while only the {001} platelet has been observed in diamond [61]. DFT modelling indicates the {113} defect is higher in energy than the {001} platelet, explaining its lack of observation in diamond, [61]. Further work is required to investigate the properties and formation of this defect in diamond.

4.2.4 Calculation of the Stacking Fault Energy

Z-type faulted dipoles are ideal defects for measuring the stacking fault energies of materials. The dissociation width (D) is a function of both the dipole height (H) and stacking fault energy (SFE) [97,142]. The Shockley partial separation, W, is sometimes referred to instead of D, and is the distance between the two 90° partial dislocations measured in the plane of the dislocation dissociation. Definitions of H, D and W can be seen in Figure 4.8 (d). The ac-STEM images of the faulted dipoles in diamond, Figure 4.8, allow for more accurate measurements of both the dissociation width and dipole height than is possible using WBDF imaging. Stacking fault energies have been measured from faulted dipoles in a variety of materials [97,143–145], however the WBDF technique is limited to only measure either the height, H, or the width, D, of the dipole, meaning only an upper limit to the stacking fault energy can be determined. Additionally, the contrast in WBDF images of dipoles with heights below 5nm is not well behaved [146] and therefore, measurements of these dipoles, cannot be accurately determined. Measurement of both H and W on the atomic scale allows for the SFE to be more accurately determined.

The equilibrium configuration of the faulted dipole can be determined by balancing the forces exerted on one of the Shockley partials by the other three partials and the stacking fault (assuming that an equilibrium configuration was attained before climb occurred). The equilibrium condition for a faulted dipole is met when the force on partial 1 is zero:

$$f_1 = \frac{a_0}{6\sqrt{3}} \sum_{2,3,4} [\sqrt{2}(\sigma_{22} - \sigma_{11}) - \sigma_{12}] - \gamma = 0 \tag{4.6}$$

where f_1 is the total force on partial 1, σ_{ij} is the ijth component of the stress tensor exerted on partial 1 by partials 2,3 and 4, and γ is the stacking fault energy. In anisotropic elasticity theory the relevant components of the stress tensor are given by the equations:

$$\sigma_{11} = C_1 \frac{-b_1 x_2[(\delta_1+\delta_2)x_1^2 + \delta_1^2 x_2^2] + b_2 x_1(x_1^2 - \delta_1 x_2^2)}{x_1^4 + \delta_2 x_1^2 x_2^2 + \delta_2^2 x_2^4} \tag{4.7}$$

$$\sigma_{12} = C_1 \frac{(b_1 x_1 + b_2 x_2)(x_1^2 - \delta_1 x_2^2)}{x_1^4 + \delta_2 x_1^2 x_2^2 + \delta_2^2 x_2^4} \tag{4.8}$$

$$\sigma_{22} = C_1 \frac{b_1 x_2(x_1^2 - \delta_1 x_2^2) + b_2 x_1[\delta_1^{-1} x_1^2 + (1+\frac{\delta_2}{\delta_1})x_2^2]}{x_1^4 + \delta_2 x_1^2 x_2^2 + \delta_2^2 x_2^4} \tag{4.9}$$

where b_i are the components of the Burgers vectors. C_i and δ_i are given by:

$$\delta_1 = (\frac{c_{11}}{c_{22}})^{\frac{1}{2}} \qquad\qquad \delta_2 = \frac{c_{11}c_{22} - c_{12}^2 - 2c_{12}c_{66}}{c_{22}c_{66}} \tag{4.10}$$

$$C_1 = \frac{c_{11}c_{22} - c_{12}^2}{2\pi c_{22}(2\delta_1 + \delta_2)^{0.5}} \tag{4.11}$$

Where c_i are the elastic constants in the reference frame of the dislocation, in which x is along $[10\bar{1}]$, y along [010] and z along [101], the dislocation has line direction parallel to x. The relation between the elastic constants in the dislocations reference frames and the cubic reference frame are given in Hirth & Lothe Theory of Dislocations Chapter 13.2 [66]. Elastic constants used for diamond were those determined by Grimsditch and Ramdas (1975) [147]:

$$c_{11} = 10.764 \times 10^{11} \text{ Nm}^{-2}$$
$$c_{12} = 1.252 \times 10^{11} \text{ Nm}^{-2}$$
$$c_{44} = 5.774 \times 10^{11} \text{ Nm}^{-2}$$

The equilibrium separation as a function of dipole height for different SFEs is given in Figure 4.11, along with the measured D and H values for the dipoles in Figure 4.8. From the three faulted dipoles in Figure 4.8, a SFE of 472 ± 38 mJm^{-2} is obtained. The configuration of all three dipoles appear to lie along the same equilibrium curve, indicating that climb of the 90° partial has occurred after the equilibrium dipole configuration has been reached.

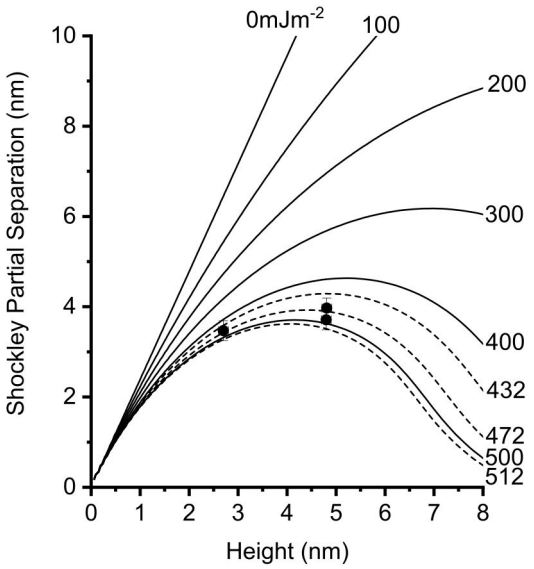

Figure 4.11: Equilibrium dipole configuration curves showing the allowed H and W measurements for different values of SFE. Measured H and W values for the dipoles seen in Figure 4.8 plotted alongside curves.

4.3 Discussion

4.3.1 Point Defect Generation in Diamond

The ac-STEM images demonstrate that a significant concentration of interstitial atoms have been generated at some point in the history of the type IIa diamond studied here, likely as a result of significant plastic deformation. There are several mechanisms that can generate intrinsic point defects in diamond so it is worthwhile briefly surveying those mechanisms to show that, in the type IIa diamond investigated here, plastic deformation is the primary mechanism at play here.

High point defect supersaturations can be generated in materials by quenching the material from a high temperature, where the thermodynamic equilibrium concentration of interstitials and vacancies is higher. This method has been used in the past to produce the climbed 90° partial structures in other fcc materials such as Si, Ga and GaAs[139,148,149]. As seen from Figure 4.1, to achieve interstitial or vacancy concentrations of 10^{17} to 10^{19} cm^{-3} would require quenching from temperatures $> 4000°C$ for vacancies and $> 6000°C$ for interstitials. These temperatures are far in excess of those that diamond experiences in the mantle and no natural mechanism exists to rapidly quench from those temperatures.

Irradiation is a commonly used experimental technique to generate Frenkel

pairs in diamond[38,81,150] and other materials. Climbed 90° partial dislocations have been created in other materials using irradiation to generate intrinsic defects[148,151]. Irradiation of diamond results in the production of the GR1 neutral vacancy centres and an accompanying green colouration[17], which upon annealing turns into a brown colouration. Natural irradiation of diamond in the mantle by alpha-decay radiogenic elements (^{232}Th, ^{235}U, ^{238}U) produces green colouration only at shallow depths from the surface due to the small penetration depth of alpha particles[17,152]. The stones examined were cut and polished into {100} facetted cubes, removing any potentially surface-irradiated material. The main beta-decay element in the Earths crust is ^{40}K, which can produce Frenkel pairs in a diamonds interior, but is very scarce in the Earths mantle. The sample could also be irradiated experimentally during TEM or SEM imaging, or during sample preparation in the FIB. TEM imaging was carried out at 200 kV, which is close to the damage threshold, 220 kV, for diamond along a ⟨110⟩ direction[153]. Nevertheless, no sample annealing was carried out at temperatures where interstitials or vacancies are mobile, and efforts were made to reduce the time spent imaging to reduce any irradiation damage. Imaging diamond in the SEM and TEM has also been found to generate Frenkel pairs and this has been successfully used to generate NV centres in diamond[154,155]. The higher vacuum pressures in the SEM and FIB allows nitrogen to be implanted into the diamond, with additional damage being generated. The PL spectroscopy was carried out post SEM imaging and FIB sample preparation and so the GR1 seen, Fig. 4.4 (b), is possibly the result of irradiation in the SEM/FIB. PL mapping of the GR1 feature would indicate if the GR1 signal is isolated to areas around the FIB milled areas, or areas viewed in the SEM, which would inform as to the origin of the GR1 signal. If GR1 is observed throughout the sample, its presence may be the result of natural processes.

Interstitials are also thought to be generated during the formation of the B-centre in diamond, with the secondary effect of forming platelets. The formation of the B-centre and platelets are believed to be linked owing to the strong correlation between the strength of IR absorption from the B-centre and the platelet[92,93]. Woods (1986)[92] proposes a mechanism for the formation of B-centres and the platelet whereby A-centres migrate as a unit and, upon encountering another A-centre, form a vacancy by the expulsion of an interstitial to complete formation of the B-centre[92]. The interstitial is then free to migrate to form the platelet. For every B-centre formed by this mechanism, an interstitial carbon atom will also be formed. Nitrogen concentrations of a few thousand ppm can be found in type I diamonds[93], which could produce over 10^{20} cm^{-3} interstitials. The interstitials then

condense into the well-known {100} platelets[92]. Based on the evidence presented here we might also expect them to produce climb of the 90° partial dislocations. The absence of B-centres and very low concentration of H3 and N3 nitrogen-vacancy complexes (intermediate steps in the formation of the B-centre) in our type IIa stone shows that nitrogen cannot be the source of the interstitials observed.

The movement of jogged dislocations by the mechanism discussed in section 4.1.1 is therefore the only mechanism which can account for the point defect concentrations measured. The sub-grain boundaries observed in the sample are likely candidates for the forest dislocations, through which dislocations move forming jogged dislocations. The estimated interstitial absorption of 10^{17} - 10^{19} cm^{-3} onto the 90° partials is consistent with estimates of point defect concentrations generated by plastic deformation, Figure 4.3, and monovacancy concentrations measured in similar brown type II diamonds[30], $\approx 10^{18}$ cm^{-3}. The similarity between the two values indicates that roughly equal numbers of interstitials and vacancies are generated during plastic deformation, by the mechanism described in section 4.1.1.

4.3.2 Climb of the 90° Partial Dislocation

The climbed 90° partial dislocation structure seen in Figures 4.6, 4.7 and 4.8 appear identical to those seen in silicon by Thibault-Desseaux et al.[139], in Cu-Al alloys by Cherns et al. (1980)[151] and Décamps et al. (1983)[149], and in GaAs by Cherns et al. (1985)[148]. In silicon, Thibault-Desseaux et al. (1989) used high-resolution TEM to examine the climbed dislocations which had been formed by carrying out a high temperature deformation and then subsequently cooled while still under load. These conditions are expected to be somewhat similar to those experienced by diamond during a kimberlite eruption, where plastic deformation is followed by cooling.

Climb of the 90° partial dislocation is thought to occur by the nucleation of, firstly, a Frank loop which then unfaults into a lower energy prismatic $\frac{1}{2}[011]$ loop[139,148,149,151] as the loop continues to grow. The formation of a Frank loop is not observed in the case of silicon by Thibault-Desseaux et al. (1989)[139]. Nucleation of loops should be able to occur via interstitial or vacancy absorption, with interstitial climb being identified by the obtuse angle formed between the nucleated loop and the stacking fault and vacancy climb from the loop forming an acute angle with the stacking fault[139], due to climb in the opposite direction.

The structure of the climbed dislocations appears to vary along the length of the dislocation line, resulting from various cross-slip events, the nucleation of discrete loops and debris remaining behind following climb[139,149]. The appearance of the climbed sections in Figure 4.6, 4.7 and 4.8 agree with this assessment. The

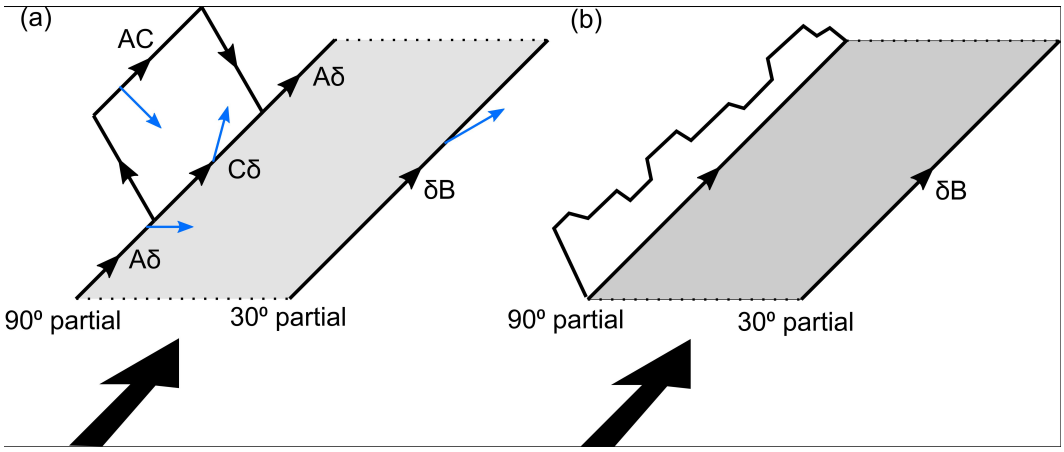

Figure 4.12: (a) Dislocation climb by growth of a prismatic dislocation loop on the 90° partial dislocation, after Cherns et al. (1985)[148]. Burgers vectors, given in Thomson tetrahedron notation, all lie in the grey (111) plane and are A$\delta = \frac{1}{6}[11\bar{2}]$, δB $= \frac{1}{6}[\bar{1}2\bar{1}]$, C $\delta = \frac{1}{6}[\bar{2}11]$ and AC $= \frac{1}{2}[10\bar{1}]$, i.e. consistent with the indexing of Figure 4.6. (b) Schematic showing a varying width of the climbed region along the defect, with undulations on the scale of a few nm in a TEM specimen tens of nm in thickness. Large black arrows show the direction of the electron beam, corresponding to Figures 4.6, 4.7 and 4.8.

atomic columns appear blurred and indistinct indicating a varying structure has been projected into the 2D image. If a prismatic loop has nucleated on the partial then the climbed section should appear as a full bilayer (a complete extra $(11\bar{1})$ plane), which is not always the case. Thinner samples may be more likely to only intersect a single climbed structure and could show the presence of a full bilayer. Thicker samples are more likely to show variations in the three dimensional structure of the dislocation.

Several interpretations have been proposed to explain the variations along the line direction, Figure 4.12.

One interpretation is that the climbed section is not a prismatic loop, instead only containing a single layer of interstitial atoms, more closely resembling the structure of the platelet, which has a single layer of interstitial atoms lying on a {100} plane. The atom columns seen in the climbed section are blurred and dimmer than surrounding atomic columns which could indicate there is less material present there, however it is not clear what the structure of a single layer of atoms between {111} planes would be.

A second interpretation is that the nucleated loop(s) do not extend throughout the entire thickness of the TEM lamella, Figure 4.12 (a). The resulting image

would then be a projection of the atomic structure through a region of perfect material and that containing an extra half plane. The atoms of the extra half plane would appear blurred and the displacement of the atomic columns would be some average of both regions. Multiple disconnected loops may be present along the line direction.

A third interpretation is that the climb extends throughout the thickness of the TEM lamella but the level of climb varies along the line direction, Figure 4.12 (b). The resulting image would also appear much like the second interpretation.

A model proposed by Thibault-Desseaux et al. (1989)[139], has prismatic loops of alternating Burgers vector character connected together along the line direction. The alternating loops would similarly cause the blurring of atomic columns in the climbed section.

Due to the inhomogeneous nature of plastic deformation the differences in the level of climb, or the formation of discrete loops along the line direction, are possibly due to inhomogeneities in the point defect densities generated from place to place in the crystal, reflecting differences in the forest dislocation density throughout the crystal. The nucleated loops are too small to be observed using WBDF imaging, so determining the structure of the climb along the dislocation line is not possible.

Only interstitial climb of the 90° partial is observed here, with the vacancies playing no part. In other fcc materials[139,148,151], where equal numbers of interstitials and vacancies have been generated, the observation of interstitial climb has been attributed to the "dislocation bias"[156]. The dislocation bias is the preferential absorption of interstitials at dislocations caused by the stronger interaction between their stress fields. The dislocation bias was proposed as a mechanism to describe the growth of voids in irradiated metals. During irradiation, both interstitials and vacancies are generated in equal numbers however the interstitials are quickly absorbed by the dislocations leaving behind an excess of vacancies. The excess vacancies cluster together eventually forming voids and causing the material to swell[156]. Ion irradiation has been shown to cause swelling in diamond[157], which indicates the dislocation bias is responsible for the absorption of interstitials here. The vacancies generated during the deformation are not absorbed onto the dislocations but instead cluster together, forming the brown colouration.

4.3.3 Faulted Dipoles in Diamond and the Stacking Fault Energy

Faulted dipoles are often observed in plastically deformed fcc materials and have been reported in metals (Cu, Ag, Ni, Au)[131,145,158–161] and semiconductors both with diamond (Si, Ge)[143,162–165] and zinc-blende structure (GaAs)[166,167]. Two

types of faulted dipole are thought to be possible, the S-type and Z-type dipoles of either interstitial or vacancy nature. The nature of the dipole is dependent on whether the connecting stacking fault (SF), between partials 2 and 3 in Figure 4.8, is extrinsic or intrinsic. If the connecting SF is extrinsic, the dipole is interstitial in nature, while an intrinsic connecting SF results in a vacancy dipole [162]. Only vacancy Z-type dipoles have ever been observed in materials [128,131,143] and the dipoles observed here agree with those results. In copper, faulted dipoles have been observed to form by conversion of unfaulted dipoles [131] and presumably are produced by similar routes here.

Measurements of the dipole height and dissociated widths of the dipoles in Figure 4.8 are consistent with a single equilibrium configuration curve [142], Figure 4.11, indicating that the faulted dipoles formed some time before climb occurred.

The SFE calculated from the faulted dipoles is significantly larger than the value of 279 ± 41 mJm^{-2} determined by Pirouz et al. (1983) [97], from dissociated 60° dislocations, but is similar to their upper limit of 465 mJm^{-2}, determined from faulted dipoles. This can be attributed to the higher accuracy of the measured H, D and W values obtained by atomic resolution imaging. Additionally, Pirouz et al. (1983) measured larger dissociation widths, ranging between 2.5 - 4.3 nm, than observed here. The larger dissociation widths contribute to the lower SFE they calculate however all of the dissociated dislocations observed here were towards the lower end of that range, and in some cases, were smaller than 2.5 nm, indicating a higher SFE for diamond.

Above a certain H, an unfaulted dipole has a lower energy than a faulted dipole [142]. The smallest dipole height measured for an unfaulted dipole is currently 7.4 nm ± 0.8nm [168] while the largest faulted dipole height observed, Figure 4.8c, is 4.73 nm (23 glide planes). The transition between the faulted and unfaulted configurations for the dipole therefore lies between these values. Below a critical height, H_c, dipoles are unstable and annihilate to form point defects. The smallest faulted dipole height observed, Figure 4.8 (a), is 2.47 nm (12 glide planes), indicating H_c is below this value.

4.4 Chapter Summary

Plastic deformation of diamond is an important mechanism by which large amounts of both interstitials and vacancies are formed. Estimates of the number of vacancies generated, from the interaction of dislocations with forest dislocations, are sufficient to account for the concentration of monovacancy type defects and vacancy clusters

observed in brown diamond by PAS.

The interaction of dislocations during plastic deformation leads to the formation of jogs, which can move by the emission of point defects. Jogs which have moved by the emission of point defects will not be observed in the TEM images, however the superjogs, formed by the movement of a dislocation through forest dislocations, will lead to the formation of dislocation dipoles, which remain behind in the crystal. These dipoles are clear evidence that point defects have been generated within the crystal. The interstitials nucleate as a prismatic loop on the 90° partial due to the dislocation bias, while the excess vacancies left behind likely cluster together into the vacancy clusters responsible for the brown colouration.

Estimates of the interstitial concentrations absorbed , 10^{17} - 10^{19} cm^{-3}, are close to the monovacancy concentrations measured in similar brown type IIa diamond, 10^{18} cm^{-3}, indicating that equal numbers of interstitials and vacancies are formed during deformation.

Faulted z-type dipoles are observed in diamond, in common with other fcc materials. Atomic resolution images of the faulted dipoles have been used to calculate the SFE of diamond giving a value of 472 $\pm$ 38 mJm^{-2}.

The defects observed in diamond following plastic deformation and the behaviour of the intrinsic point defects appears to be no different to that seen in other fcc materials, albeit under far more extreme conditions.

Chapter 5

Spatial Distribution of Defects in a Plastically Deformed Natural "Zebra" Brown Diamond

5.1 Introduction

Colouration in plastically deformed type I diamonds, predominantly brown and pink, tends to be localised within lamellae lying along {111} planes, while in type II diamond, the colouration tends to be found with a uniform distribution throughout the sample, although the occasional type IIa diamonds can show some deformation lamellae[10,169]. Single crystal diamond where the brown lamellae are separated by colourless regions, with an alternating brown-colourless pattern, are sometimes referred to as "zebra" diamonds. These coloured lamellae are consistent with slip bands in the material, caused by the movement of dislocations during plastic deformation[128], or deformation twins[14,63,170]. The appearance of coloured lamellae within bulk colourless material is commonly referred to by gemmologists as "graining" (or specifically "brown-graining and pink-graining" in cases where the colouration is well defined)[10,14,170]. These "zebra" diamonds are extremely useful for comparing the effect of plastic deformation on the dislocation microstructures and point defect distributions. Additionally, the presence of both brown and colourless material in the same sample reduces the sample-to-sample variations that could be present if comparing two different samples. Similar conditions will be experienced by both the brown and colourless material.

Plastic deformation can produce a variety of effects on the crystal structure which can contribute to the colouration of the diamond. The primary changes to the crystal induced by plastic deformation is the generation and movement of dislocations within the material or the formation of deformation twins [10,14,170,171]. As deformation progresses, the glide motion of dislocations will cause slip bands to appear at the surface of the material, while dislocations within the material will rearrange themselves in an attempt to reduce crystal stresses, leading to the formation of various distinctive dislocation microstructures and causing work hardening of the material [127,128,172]. As seen in Chapter 4, secondary effects of plastic deformation are the production of intrinsic point defects (both interstitials and vacancies) caused by the movement of jogged dislocations. At the temperatures required for plastic deformation of diamond, the interstitials and vacancies can readily migrate to form new point defect complexes. For example, as mentioned in Section 2.1.2, the H3 centre is commonly observed with higher concentrations in areas showing evidence of deformation [85–87].

Plastic deformation is often thought to enhance the migration of nitrogen via interstitial or vacancy mediated diffusion processes, however this might not always be the case. It has been suggested that the movement of dislocations through point defect complexes can break them up, resulting in the production of single substitutional nitrogen atoms [46] or the creation of new point defects. The movement of dislocations through A-centres has been proposed as the origin of a series of point defects, such as the "amber" centres and W7/N2 EPR centres, observed in plastically deformed diamonds [11,173].

In this chapter untreated and treated "zebra" diamond samples, containing both brown and colourless bands, were examined to investigate these plastic deformation processes. Correlative microscopy was used to obtain a more complete picture of the material properties and processes, able to image the sample on various length scales and extract more information than possible with a single technique. Here PL, CL and Raman spectroscopy were used to observe the point defect distributions and crystal stresses, with TEM being used to image the dislocation microstructure in order to examine their relationship.

The untreated and treated samples observed here originated from the same original stone. After being cut into a number of sections, those sections then underwent differing treatments, Section 3.6, before being examined here. HPHT treatment would destroy a thinned TEM sample, so a direct comparison of the same region before and after treatment could not be performed. Assuming the defect microstructure is uniform throughout the original sample before being sectioned,

comparisons can be made between the different sections to examine the effect of HPHT treatment.

5.2 Results

5.2.1 Optical Imaging and Spectroscopy of Untreated Sample

Optical images of the untreated sample, A628-09-07-a, show the brown colouration is concentrated in sharp bands, Figure 5.1 (a). The sample has been cut and polished with the major face parallel to {110}, resulting in a view directly down the ⟨110⟩ zone axis. The brown bands are orientated at approx. 54° (± 3°) to the {100} face, consistent with the intersection of a {111} plane on the {110} face, as expected for slip bands. A distinct brown band is highlighted, ■, as a useful reference for comparison between the various imaging techniques. Birefringence imaging, Figure 5.1 (b), which is sensitive to shear strains that induce optical anisotropy, clearly shows the bands and the highly strained nature of the diamond. The stress appears to vary across the sample, with a distinct banding pattern, where broader bands in the material show a higher order of birefringence at the interfaces.

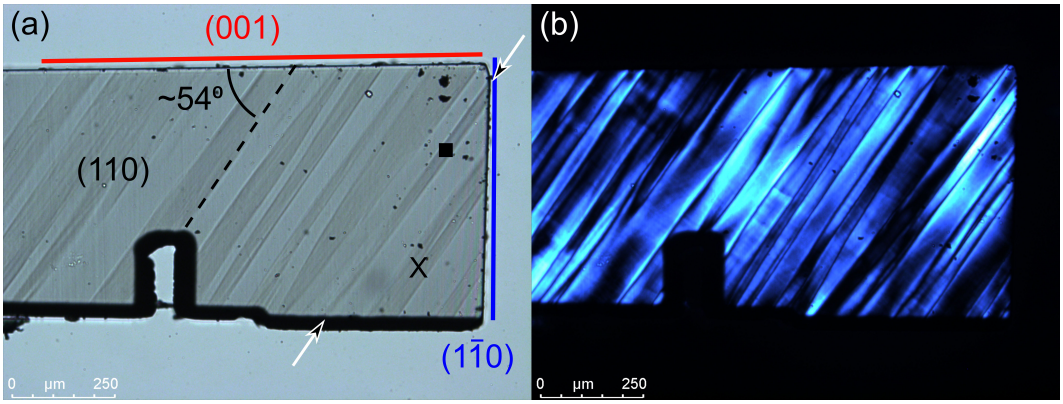

Figure 5.1: (a) Optical Image of section of A628-09-07-a (untreated sample). Brown colouration appears as bands running from bottom-left to top-right.{100} and {110} planes highlighted by red and blue colour respectively. X marks approximate location of PL spectra seen in Figure 5.3. A distinct brown band, ■, used as a reference is highlighted. (b) Imaged with cross polarisers to show birefringence. Sample is highly strained along the bands.

While the birefringence images can image shear strains in the sample, shifts in the peak position of the Raman line can be used to measure hydrostatic stresses in the diamond. The results of Raman mapping from 660 nm laser excitation can be

seen in Figure 5.2. The hydrostatic stress present in diamond was calculated from the shift in the position of the Raman line using the formula $\sigma = \Delta_{shift}/\alpha$, where Δ_{shift} is the difference in Raman peak position measured from the peak position in unstrained diamond (taken to be 1332.5 cm^{-1}) and α is the hydrostatic stress gauge factor (approx. 2.9 cm^{-1}/GPa)[174].

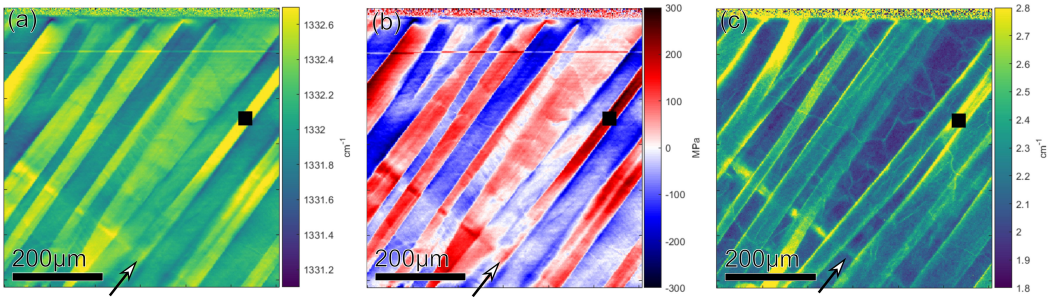

Figure 5.2: (a) Map of Raman peak position of A628-09-07-a shown in Figure 1, right side of sample. (b) Map of hydrostatic stress calculated from shift in Raman peak position. (c) Map of Raman peak width. The distinctive brown band, ■, is highlighted in all images.

Comparing the maps of Raman peak position and hydrostatic stress, Figure 5.2 (a,b), with the optical images, Figure 5.1 (a,b), the brown bands appear to be under compressive stresses, as seen by ■, while the colourless bands are under tensile stress. Stresses approaching 300 MPa appear to be achieved close to the interface between colourless and brown bands, with reduced stresses being found near the middle of the bands. The interface between the bands appear to be under zero stress, as expected of material between regions of compression and tension, although the gradient of stress will be quite high as evident by the increase in width of the Raman line. A cellular dislocation network can be seen in Figure 5.2 (c), evident from an increase in the width of the Raman line. These sub-grain boundaries are found in both the brown and colourless bands, and cross the interfaces between the bands. As discussed in Chapter 4, these sub-grain boundaries may play the role of the forest dislocations during plastic deformation giving rise to the brown colouration.

PL spectroscopy of a brown band, Figure 5.3, at the location marked X in Figure 5.1, indicates the presence of several point defects. As expected, for plastically deformed natural diamond, the zero-phonon line (ZPL) of both N3 (415.4 nm) and H3 (503.2 nm) are present. In addition to the N3 and H3 lines, the Raman line at 521 nm and a strong line at 535.9 nm can be seen, while weak lines can be

observed at 406.3 nm and 491.3 nm. Some finer features are potentially present between the sidebands of the N3 centre with a possible peak at 423 nm, Figure 5.3 (a) inset, although the intensity of these features is of the order of the noise and accurate determination of peak wavelengths through fitting is difficult. Mapping of the N3, H3 and 535.9 nm features over the same region as Figure 5.1 show how these defects are distributed throughout the sample. The results of fitting the N3, H3 and 535.9 nm lines with a single Voigt peak can be seen in Figure 5.4.

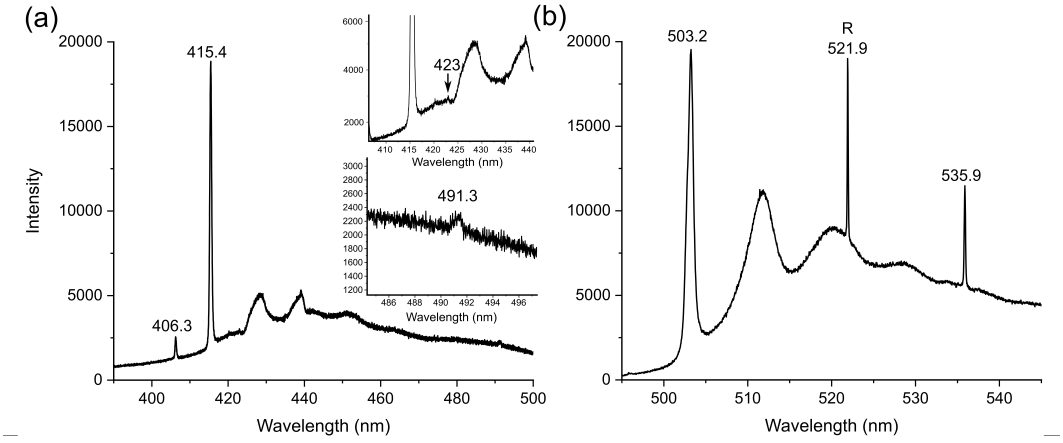

Figure 5.3: (a) PL spectrum of A628-09-07-a in the region 390 - 500 nm in the pristine sample A628-09-07-a. ZPL can be seen at 406 nm and 415 nm (N3). Spectrum obtained using 325 nm laser at LN temperatures. Inset, small features between N3 phonon sidebands and small peak at 491.3 nm. (b) PL spectrum in the region 495 - 545 nm. Raman line (R) observed at 521 nm. ZPL observed at 503 nm (H3) and 535 nm. Spectrum obtained using 488 nm laser at LN temperatures.

The distribution of the N3, H3 and the 535.9 nm centres appear to be correlated with the colouration, although the N3 centre appears to only be weakly correlated. Bands of higher N3 concentration can be seen however the resemblance of the bands to the optical image, Figure 5.1, is less obvious. Within the bands the distribution of N3 centres appears to vary, quenching from sub-grain boundaries is a possible reason for these variations, however from Figure 5.4 (b, c), the sub-grain boundaries observed do not completely match the decreases in intensity of N3 observed. The resolution of the N3 map is insufficent to resolve the sub-grain boundaries owing to the larger pixel size (of 7.5 μm), while pixel interpolation has been used to obtain a less pixelated image.

The H3 intensity map, Figure 5.4 (b), was obtained by plotting the integrated intensity between 500 - 506 nm, rather than the amplitude of single Voigt peak fit.

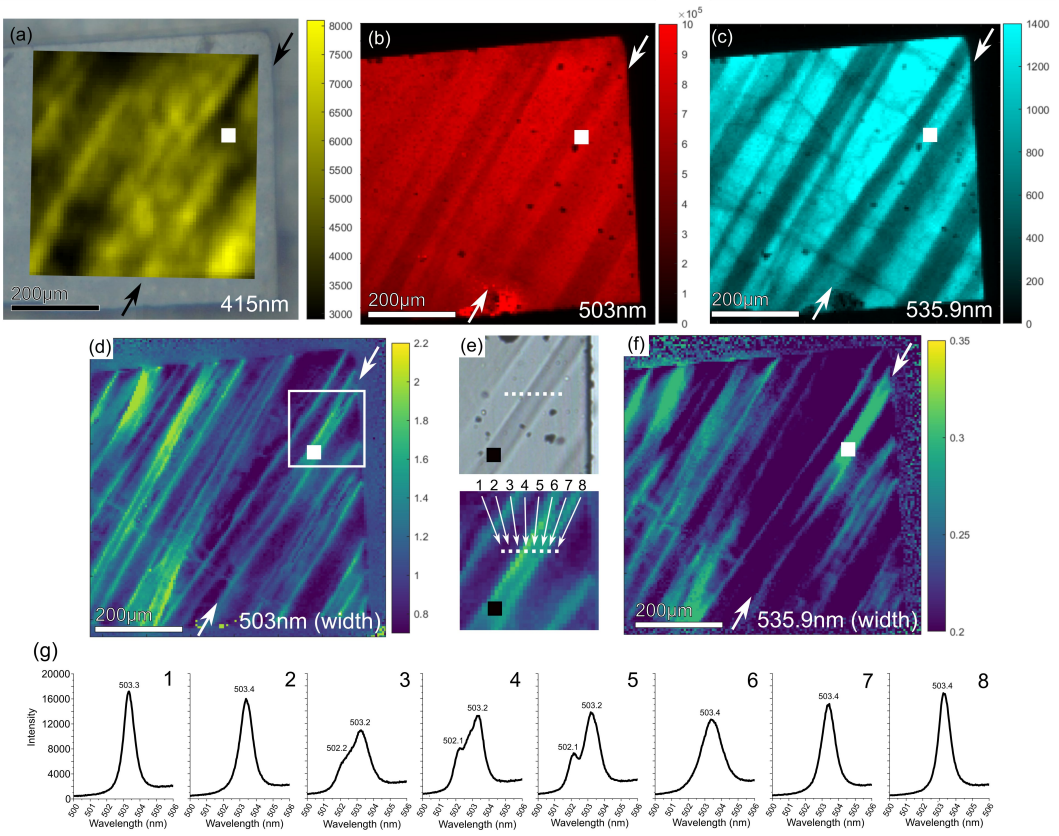

Figure 5.4: PL maps of the (a) N3, (b) H3 and (c) 535.9 nm line intensities in A628-09-07-a. (d) Example showing the splitting of the H3 line and (e) Locations of spectra shown in (g), which highlights the splitting of the H3 peak crossing the distinct brown band highlighted by ■. Upper - higher magnification optical image of region highlighted in (d). Lower - higher magnification H3 peak width map of region highlighted in (d). (f) Map of the width of the 535.9 nm line. (g) H3 line at various points across the thin brown band highlighted in (e), showing the splitting of the H3 line into two peaks.

This is because peak fitting was complicated by the splitting of the H3 peak at the interfaces between the bands. Regions where peak splitting of the H3 line occurred can clearly be seen from a plot of the width of the H3 peak (when fit with a single Voigt peak), Figure 5.4 (d). H3 peak splitting across the interface between bands can be seen in Figure 5.4 (e,g). Comparing the plot of integrated H3 intensity, Figure 5.4 (b), with the optical image, Figure 5.1 (a), the H3 defect is observed with larger concentration in the brown bands, with an intensity $\sim \times 2$ larger than in the colourless bands. Sub-grain boundaries are not seen in the H3 map, indicating that they do not appreciably quench the H3 emission.

The 535.9 nm centre, Figure 5.4 (c) is strongly correlated with the deformation lamellae, appearing with increased concentration in bands of brown colouration and being almost completely absent in the colourless bands. Sub-grain boundaries can be clearly seen, running from top-left to bottom-right in the image, indicating the defect responsible for this emission is quenched by the dislocations. Similar to the broadening of the Raman line, the H3 and 535.9 nm ZPL lines are broadened at the interfaces between the bands and at sub-grain boundaries, indicating that the broadening is due to stress. Broadening of the 535.9 nm line is much smaller ($\sim$ 0.15 nm) compared to that of the H3 line ($\sim$ 1.4 nm), although the H3 broadening measured, Figure 5.4 (d), is partly due to the splitting of the H3 peak rather than the width of a single H3 peak increasing.

In summary for the untreated sample, the brown bands have higher concentrations of the H3, N3 centres and the 535.9 nm defect. The correlation is low for the H3 centre and N3 is only slightly enhanced in brown bands. Both H3 and 535.9 nm show broadening/splitting near to boundaries indicating a sensitivity to stress and/or strain, but only the 535.9 nm defect appears to have its luminescence quenched by the sub-grain boundaries.

5.2.2 Optical Imaging and Spectroscopy of Treated Sample

Optical images of the treated stone A628-09-02-a shows a marked reduction in the brown colouration, Figure 5.5, although faint bands can still be seen. Birefringence imaging, Figure 5.5 (b), shows some shear strain remains present in the sample, primarily localised at the interface between the colourless and formerly brown bands.

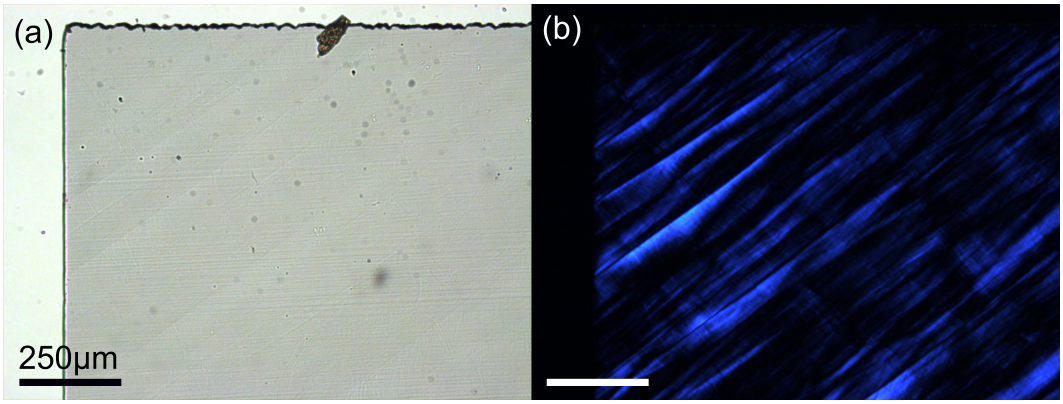

Figure 5.5: (a) Optical image of A628-09-02-a (treated) stone. Banding can still be observed although the colouration is substantially faded. (b) Birefringence image showing some strained regions remain after treatment.

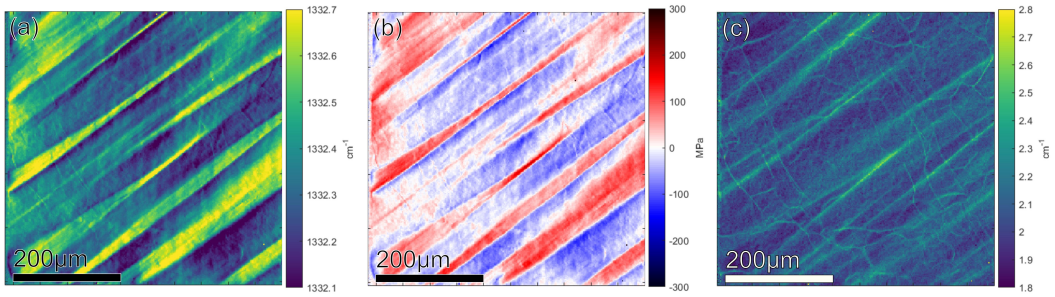

Figure 5.6: (a) Map of Raman peak position of area of A628-09-02-a (treated), different area from Figure 5 (a). (b) Map of hydrostatic stress calculated from shift in Raman peak position. (c) Map of Raman peak width.

Raman stress mapping shows that internal stresses are still present in the sample, Figure 5.6 (Raman stress mapping was carried out on a different location to Figure 5.5 however the orientation of the sample is still the same). Plotted over the same colour scales as Figure 5.2, the magnitude of the internal stresses is found to be much reduced post treatment, Figure 5.6 (a, b), as seen from the reduced contrast. This reduction in sample stress after treatment can be clearly seen from a histogram, Figure 5.7, of the stress values in Figures 5.2 (b) and 5.6 (b). Figure 5.7 shows both a reduction in higher magnitude stress values and a narrowing of the distribution measured. The standard deviation of the stress values decreases from a value of 92 MPa, in the untreated sample, to 52 MPa, in the HPHT treated sample. Compressive stresses are still seen in the formerly brown bands with tensile stresses in the colourless bands. The width of the Raman line is still observed with a larger value at the interfaces however the broadening is reduced ($\sim$ 2.4 - 2.5 cm^{-1}) compared to the untreated sample ($\sim$ 2.8 cm^{-1}), Figure 5.6 (c).

PL spectra from a formerly brown band show changes to the point defects now present, Figure 5.8. The 406.3 nm, 491 nm and 535.9 nm lines have been completely removed by the treatment, indicating that these point defect complexes are broken up at temperature below 2000 °C. Maps of the H3 and N3 ZPL intensities can be seen in Figure 5.9.

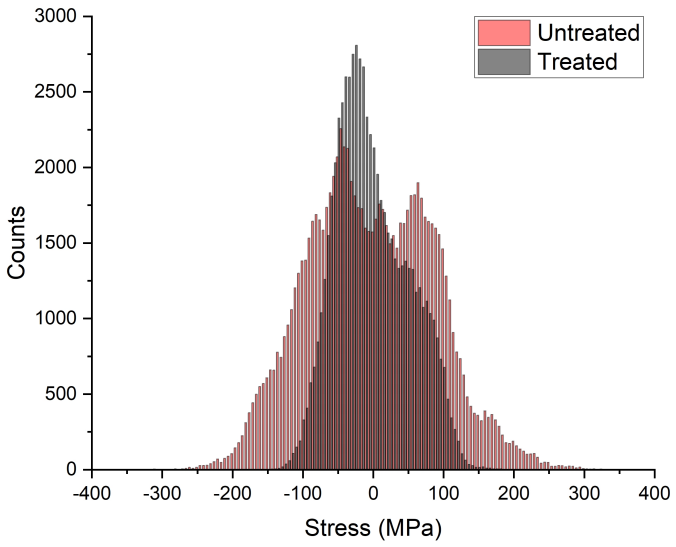

Figure 5.7: Histogram of Raman stress values for the untreated (red) and treated (black) samples. A reduction in the magnitude and spread in stress values can clearly be seen post treatment.

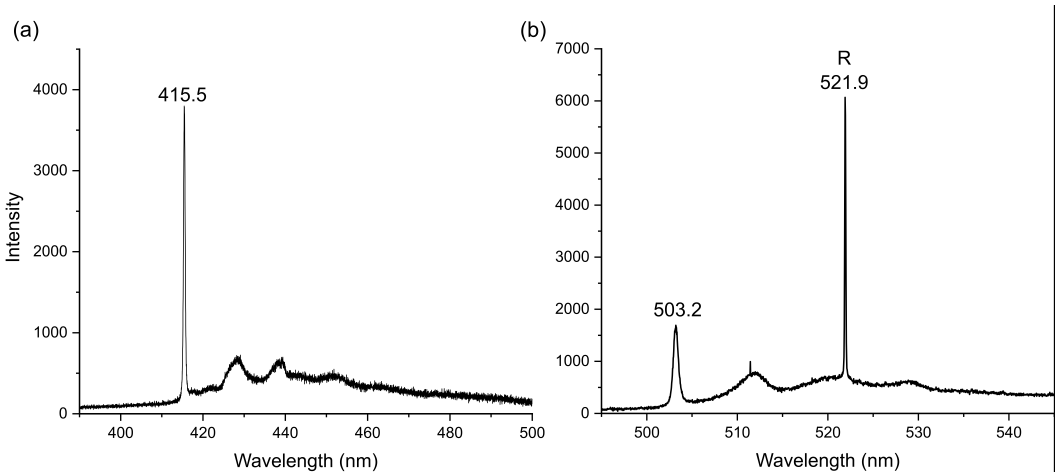

Figure 5.8: (a) PL spectrum in the region 390 - 500 nm in the treated sample A628-09-02-a. ZPL at 406 nm and 491 nm have been removed post treatment. Spectrum obtained using 325 nm laser at LN temp. (b) PL spectrum in the region 495 - 545 nm. Raman line observed at 521 nm. H3 present at lower concentration while 535 nm line completely removed. Spectrum obtained using 488 nm laser at LN temp. PL spectra are representative of entire mapped area.

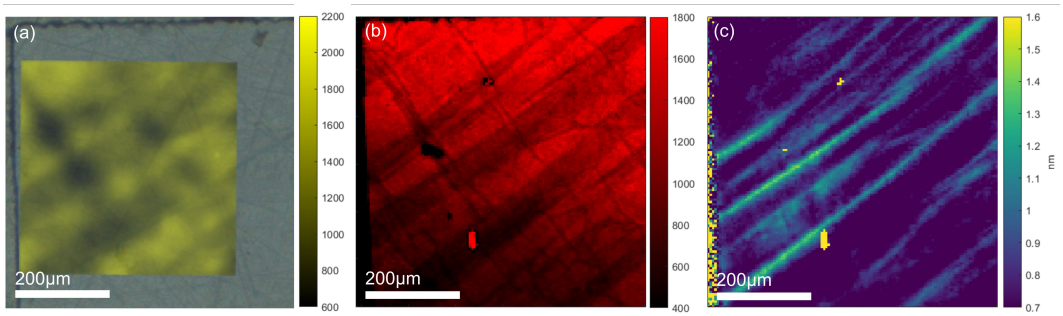

Figure 5.9: (a) N3 and (b) H3 peak intensity maps of A628-09-02-a. N3 concentrations appear to be larger in areas containing fewer H3 centres however dislocations also quench the emission.

The intensity of point defect lines is much reduced post-treatment however the distribution of remaining point defects is largely unchanged. The H3 centre can still be found with higher concentration in the formerly brown bands and the distribution of N3 centre with respect to the bands, Figure 5.9 (a), appears slightly clearer, with higher concentrations appearing in the formerly brown bands. Imaged at a slightly higher magnification than the untreated sample, Figure 5.4, Figure 5.9 clearly shows that the sub-grain boundaries quench both the H3 and N3 emission, and may be partly responsible for the varying distribution of the N3 centre within the bands. No splitting of the H3 peak was observed and the width of the H3 line was found to be substantially reduced, ~ 1.6 nm, compared to the untreated sample, ~ 2.2 nm. The reduction in the width of the H3 line is consistent with a reduction in the stress, as shown by the Raman line.

For the HPHT treated sample, the results show that, in addition to the loss of brown colouration, a significant reduction in internal stresses/strains and point defect concentrations occurs during the treatment. Several point defects have been removed by the treatment. The presence of vacancy clusters and point defect complexes will contribute to the internal stresses present so the reduction in point defects is also reflected in the stresses measured.

5.2.3 Cathodoluminescence Imaging and Spectroscopy

CL imaging was utilised to provide a link between the PL mapping and the TEM imaging carried out, able to provide similar information to PL but at a resolution limited mainly by the diffusion length of free carriers, injected into the diamond by the primary electron beam. Panchromatic CL images of A628-09-07-a and A628-

09-02-a are shown in Figure 5.10.

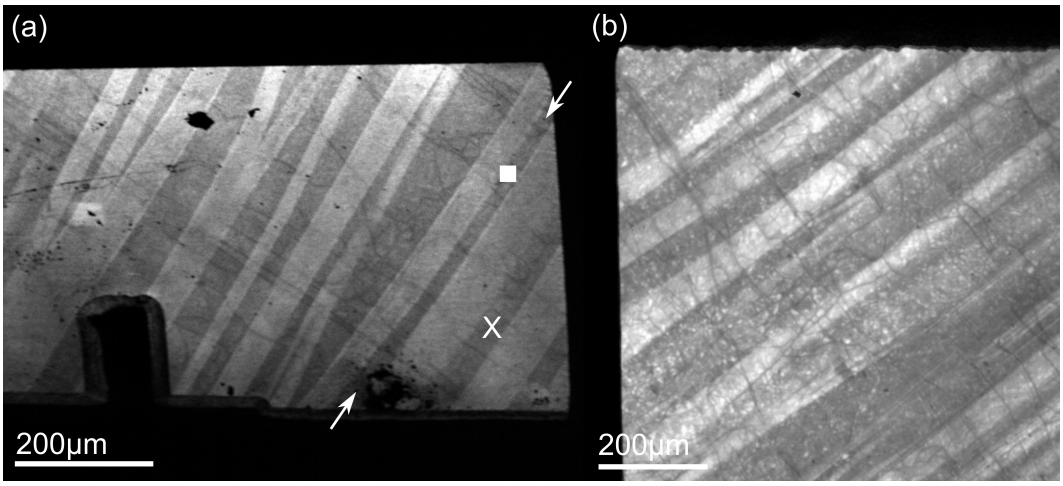

Figure 5.10: Panchromatic CL images of (a) A628-09-07-a untreated diamond and (b) A628-09-02-a treated diamond. PL mapping carried out in top left corner while Raman mapping was bottom left corner.

The appearance of the slip bands in CL, Figure 5.10 (a, b) is comparable to that seen optically and by PL mapping. Comparing the panchromatic CL images, Figure 5.10 (a, b), to the corresponding optical image of each sample, Fig. 5.1 (a) and 5.5 (a), the brown bands are found to correspond to areas of reduced CL intensity (dark CL bands) while the colourless bands correspond to increased CL intensity (bright CL bands). This contrast is opposite from that observed by PL, where the brown bands show higher defect luminescence, for H3, N3 and 535.9 nm defect centres. Despite the reduction of the brown coloration in the treated sample, Figure 5.5 (a), the contrast seen in panchromatic CL images appears unchanged compared to the untreated sample. Quenching of the emission is still seen at sub-grain boundaries, matching with those seen in PL. Looking at the CL spectra, it can be seen that most of the image intensity is due to the Band A emission, Figure 5.11. To allow for comparison of the spectra from both the brown and colourless band, both spectra were normalised to the value at 300 nm. This value was chosen to account for differences in the background level, as no defect or band gap emission is expected at this wavelength[25].

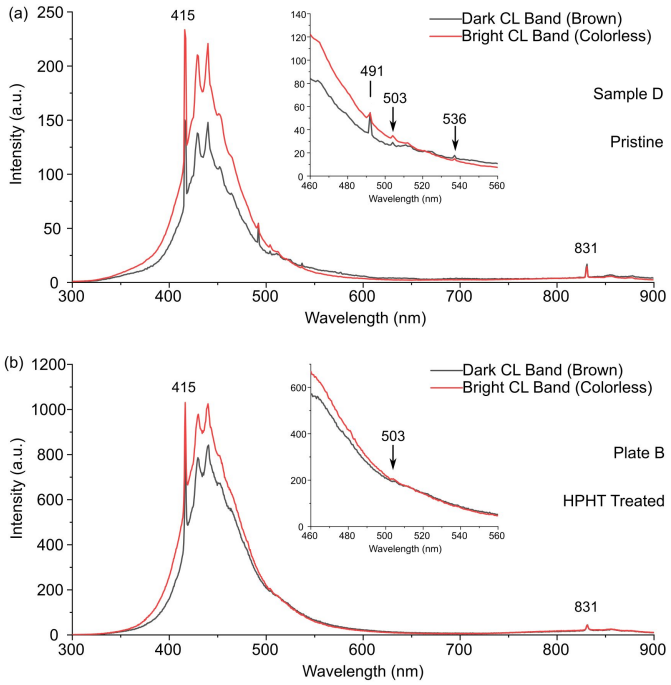

Figure 5.11: CL spectra of (a) A628-09-07-a (untreated) and (b) A628-09-02-b (treated) at LN temp (Normalised at 300 nm to allow comparison between spectra). Spectra reveal the presence of the N3 defect at 415 nm, overlaid on the broad peak of band A emission in both untreated and treated sample. Second order N3 ZPL can be seen at 831 nm. Untreated sample shows additional peaks at 491, 503 (H3) and 535.9 nm in agreement with PL spectra. A possible H3 peak is still observed after treatment but of reduced intensity.

In both samples, Figure 5.11, the N3 ZPL and phonon sidebands can clearly be seen on top of the Band A emission, centred at approx. 440 - 450 nm. Band A emission is $\sim \times 2$ stronger in the colourless band compared to the brown bands in the untreated sample. Additional peaks are seen in the untreated sample, with lines at 491 nm, 503 nm and 536 nm. While a 406 nm line is observed in PL for the untreated sample, it is not observed in the CL spectrum. The 491 nm line is much stronger in CL compared to PL, while the H3 and 535.9 nm lines, which were much stronger in PL, are considerably weaker in CL. Post HPHT treatment, the 491 nm and 535.9 nm lines are completely removed, with the H3 line becoming much weaker. The contrast between the colourless (bright) and brown (dark) bands in the panchromatic CL images appears to be mainly due to the intensity of the Band A emission, with a greater intensity of Band A being emitted from the colourless

bands, rather than the brown bands.

Band A emission remains stronger in the colourless bands after HPHT treatment, Figure 5.11 (b), although the difference in luminescence is reduced.

5.2.4 Transmission Electron Microscopy results

After thinning to electron transparency, panchromatic CL imaging of A628-09-06 (untreated) was used to locate the boundary between a brown and colourless band, Figure 5.12 (a), which could then be examined in detail in the TEM. The boundary located, Figure 5.12 (a), had a distintive sub-grain boundary crossing the brown-colourless interface, higher magnification image shown in Figure 5.12 (b), which was easily identified in the TEM. TEM imaging, using a $\mathbf{g}3\mathbf{g}$ $2\bar{2}0$ WBDF condition, across this boundary is shown in Figure 5.12 (c).

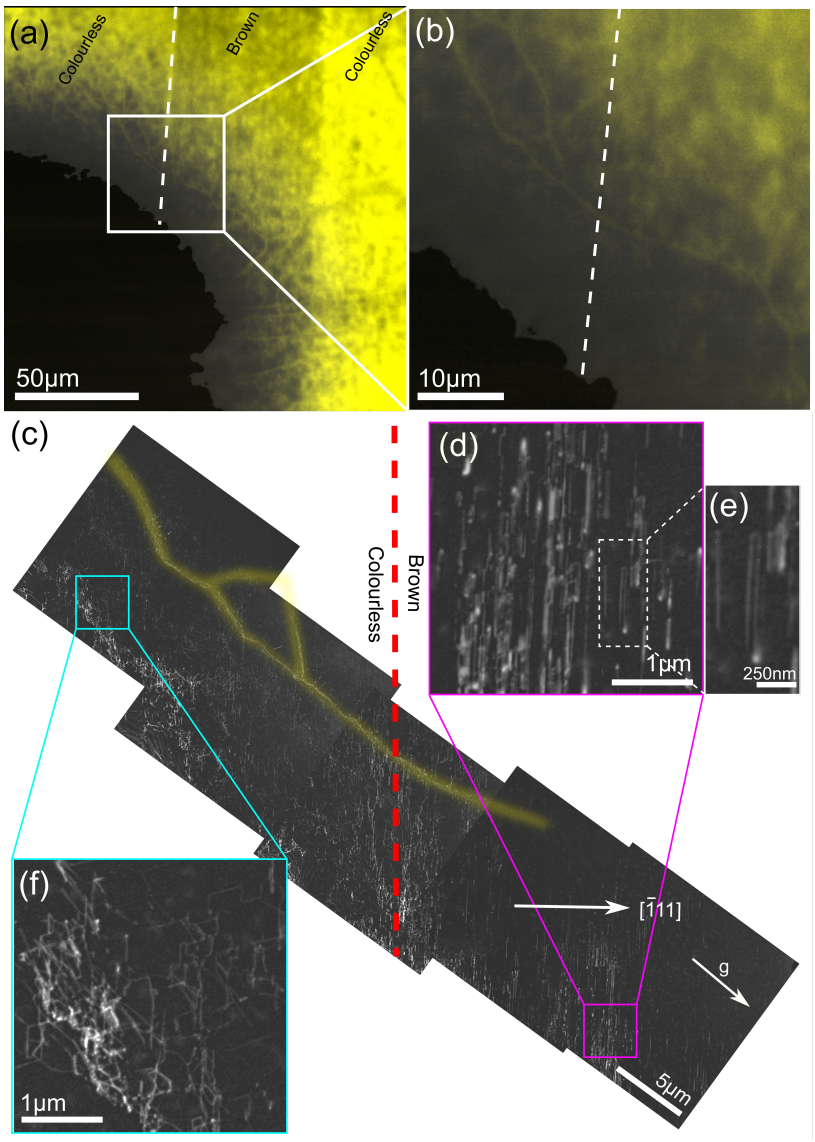

Figure 5.12: (a) Low magnification CL panchromatic image (yellow) overlaid on the secondary electron image (white). Brown and colourless bands labelled. Interface imaged in TEM has been highlighted. (b) Higher magnification CL image of interface region examined in TEM. (c) WBDF TEM image of dislocation microstructure across the boundary between a brown and colourless band, highlighted in (a,b) in A628-09-06, approximate location highlighted by dashed line. Image formed by stitching together multiple images. (d) Dislocation microstructure within the brown band showing the dislocations are predominantly straight dipoles. (e) Higher magnification image of area in (d) showing a dislocation dipole. (f) Dislocation microstructure within the colourless band showing the random, more tangled dislocation structure.

Clear differences in the dislocation microstructure between the two bands can be seen, Figure 5.12 (a). In the brown band, long straight dislocations and straight dislocation dipoles were observed in large numbers, lying parallel to the direction of the band, on the $(\bar{1}11)$ plane. In the colourless band, dislocations were predominantly found in a more random, tangled three dimensional arrangement, with lots of intersecting dislocations and curved sections. No significant differences in the dislocation densities are apparent from the WBDF images, only the structure appears to be different between the bands.

Higher magnification WBDF images of dislocation dipoles in the brown band are shown in Figure 5.13. A high density of long straight dislocations can be seen lying parallel to the axis of the band, on $(\bar{1}11)$ planes, running bottom left to top right. These long straight dislocations appear to be connected to dislocations which run roughly horizontal in the image, with line directions lying between $[1\bar{1}0]$ and $[2\bar{2}1]$. These horizontal dislocations closely resemble the expected structure obtained by the movement of a dislocation through forest dislocations, similar to Figure 4.2 (a,b,c). The continued movement of these dislocations through the forest dislocations will be responsible for the formation of the dipoles. Figures 5.13(b) and (c) show the interaction in more detail with a pair of bright field TEM images with opposite g-vectors. The reversal of contrast in these images show that many of the straight defects are dipoles. This contrast reversal is marked by black and white bars for a particularly widely-spaced dipole in Figures 5.13(b) and (c) but can also be seen for other defects.

After HPHT treatment the general dislocation structure appears unchanged as shown in Figure 5.14. Dislocation dipoles remain in the formerly brown bands and dislocations are still observed in tangles in the colourless band. On larger lengths scales the dislocation structure appears unchanged, however changes to the dislocation structures on small length scales may have occurred, requiring further AC-STEM imaging.

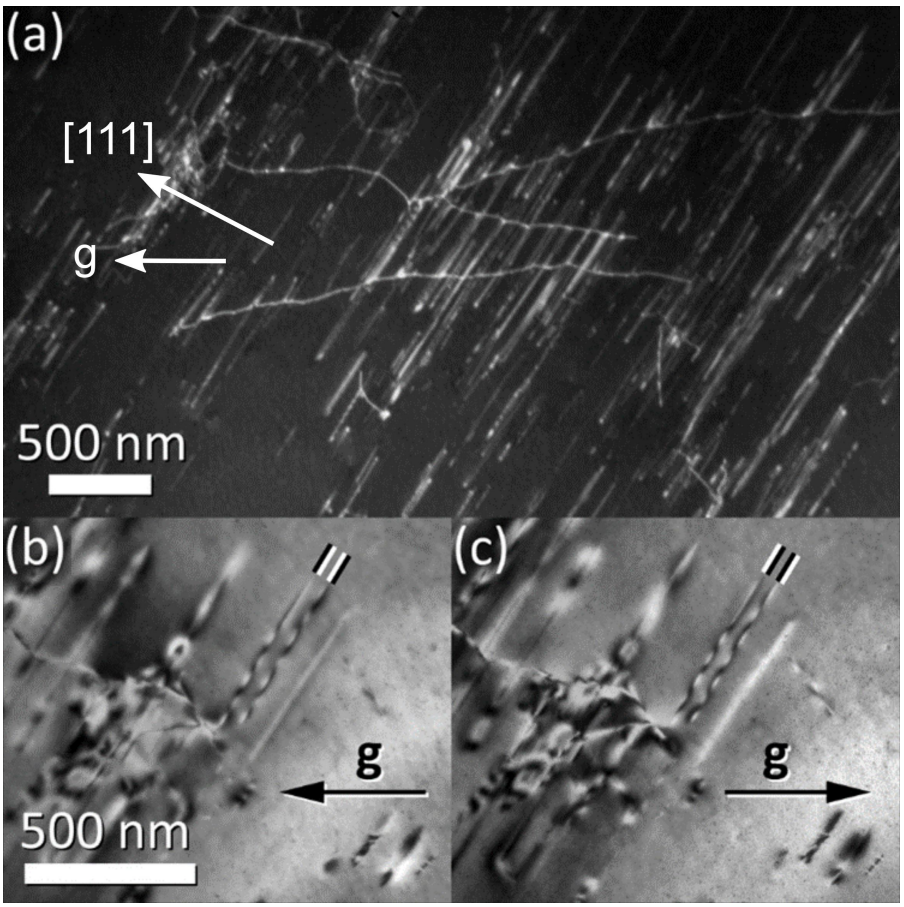

Figure 5.13: (a) WBDF TEM image of dislocation dipoles in A628-09-06. Movement of horizontal dislocations through dislocations lying on another glide planes have formed jogs, and upon further movement have produced dislocation dipoles lying along the bottom-left to top-right direction. This type of dislocation structure is only observed in the brown bands and indicates plastic deformation, and intrinsic point defect production, has occurred. (b, c) A pair of BF TEM images with reversed g-vector. For dipoles, reversing the g-vector causes the contrast to change from inside to outside, indicated by the black and white bands for one dipole with a wide spacing (∼30 nm) between the dislocations.

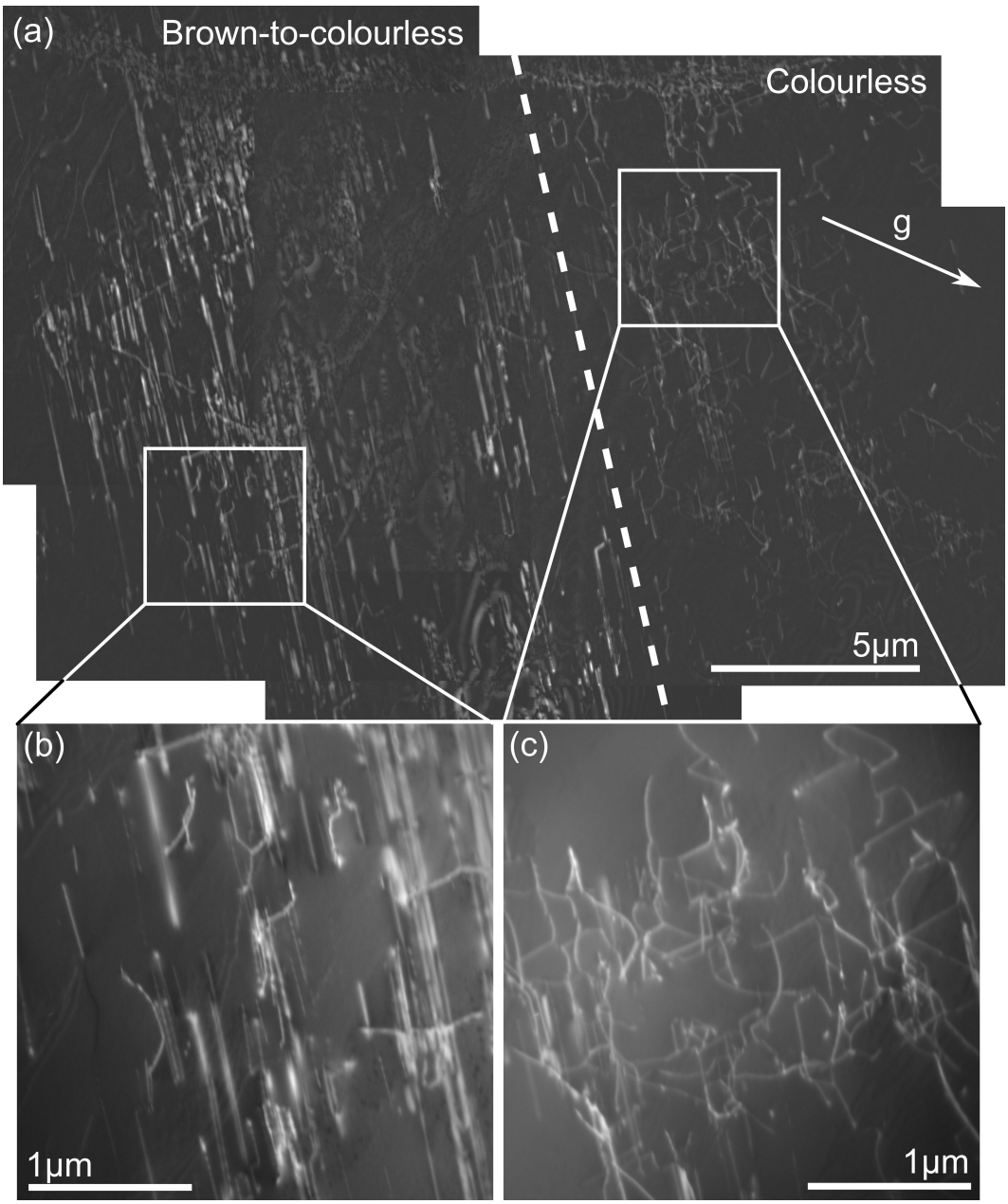

Figure 5.14: (a) DF TEM image of dislocation microstructure in A628-09-02-b across the boundary between a formerly brown and colourless band. Image formed by stitching together multiple images. Dislocation microstructure is unchanged by the treatment. (b) Higher magnification image of dislocation dipoles in the formerly brown band and (c) in the colourless band.

5.3 Discussion

5.3.1 Effects of Plastic Deformation

The optical properties and defect distributions observed in the zebra diamond are strongly affected by plastic deformation. Visually the most obvious sign plastic deformation has occurred are the appearance of deformation lamellae or slip bands, which take on a brown colouration and lie along a {111} plane. No twins are observed in the sample. The appearance of the brown bands is similar in appearance to those seen in other fcc materials which have undergone plastic deformation, and are consistent with a material that has gone into stage II deformation [127,128]. As discussed in Chapter 4, the observation of dislocation dipoles in the brown bands indicate that large concentrations of intrinsic point defects have been generated. At the high temperatures required for the plastic deformation of diamond, the interstitials and vacancies generated will be mobile, being trapped at impurities/dislocations or aggregating together to form clusters. The optical imaging, PL, and Raman mapping carried out produce results which agree with that assessment.

The brown colouration of the slip bands indicates the presence of vacancy clusters, formed from a supersaturation of vacancies, while the PL mapping, Figure 5.4, also shows these bands contain a larger concentration of H3 centres. An abundance of vacancies in these bands, which are able to migrate and be trapped at A-centres, is the likely cause of the increased H3 concentration. In metals which have been heavily irradiated, the generation of intrinsic point defects produces a volume expansion due to the formation of voids [175,176], which are simply large vacancy aggregates/clusters. This volume expansion has also been seen in irradiated diamond [157]. Raman stress mapping, Figures 5.2 and 5.6, shows the brown bands under compressive stresses, which is consistent with the diamond having undergone expansion, due to the presence of vacancy clusters, or "small voids". The compressive stresses of the brown bands induce the neighbouring colourless bands to be under tensile stress.

Chapter 4 shows that large concentrations of interstitials and vacancies are generated during the plastic deformation, with interstitials being absorbed onto the partial dislocations, and vacancies forming clusters. Both defects may also be trapped at impurities or caused enhanced migration of nitrogen. The alternating brown and colourless bands allows for these other processes to be probed.

In addition to the H3 and N3 centres, the untreated sample has PL lines at 406.3 nm and 535.6 nm, as well as a weak peak at 491.3 nm. Some weaker features within the N3 phonon sidebands are possibly observed however they are

too weak to confirm their presence, e.g , a weak PL line at 423 nm. These PL lines have been seen in other plastically deformed diamond and have been attributed to plastic deformation.

Collins & Woods[85] and Nadolinny et al.[177] have both observed a line at 490.7 nm in plastically deformed type I diamond. Collins & Woods[85] found the 490.7 nm line to be correlated with growth bands or slip bands in the diamond and always accompanied by a line at 423 nm. Similarly Nadolinny et al. found the 490.7 nm line to be associated with lines at 406 nm and 423 nm, and correlated with an EPR signal from dangling bonds within dislocation cores. A similar line at 491.3 nm was found in plastically deformed diamond by Graham and Buseck[88], who proposed that the defect is formed by the movement of a dislocation through an A-centre, causing its dissociation and forming a defect with structure, N-C-C-N[88]. In brown type Ia diamond, this 490.7 nm line can sometimes be the strongest emission line in CL[178].

The 406.3 nm line is close in wavelength to a ZPL at 405.5 nm line, which has been proposed as a strain modified N3 centre by Gaillou et al.[14]. Any phonon sideband structure of the 406.3 nm line is obscured by the N3 ZPL and accompanying structures so a comparison between the 406.3 nm defect observed here and the 405.5 nm defect observed by Gailllou et al.[14] cannot be made. Gaillou et al.[14] did not observe any line at 491 nm, which could indicate that their 405.5 nm defect and the 406.3 nm defect could be two different defects. The 490.7/491.3 nm line does appear to be weak in PL which may account for its lack of observation by Gaillou et al.[14].

Nevertheless, the 406.3 nm and 491.3 nm lines are almost certainly nitrogen containing defects which are products of plastic deformation. They are formed either by the movement of a dislocation through an existing point defect complex (A-centre), in the case of the 491.3 nm defect, or are located in highly strained regions, possibly surrounding a dislocation core in the case of the 406.3 nm defect. Mapping of these defects hasn't been carried out due to their weak signal, so their distribution remains inconclusive in these samples.

The 535.9 nm line was strongly correlated with the slip lamellae, appearing with a higher concentration in brown bands, and is either quenched or not present at the sub-grain boundaries. A line at 535.8 nm is commonly observed in Argyle diamonds and some brown diamonds, and has been attributed to the IaB character of the diamond[14,178,179], Section 1.6. The line has been observed around inclusions and deformation lamellae in milky type IaB diamonds indicating it is a product of plastic deformation[180]. Gu and Wang[180] found the 536 nm line was correlated

with a line at 496 nm (the H4 centre). The H4 centre is comprised of 4 nitrogen atoms and 2 vacancies and it was suggested that the 536 nm defect could be related in some way to this defect [180]. Uniaxial stress measurements of the 536 nm defect indicate it has monoclinic symmetry, while the small movement of the line in response to stresses mean that this defect is unlikely to contain a vacancy [181]. The sharpness of the ZPL, along with the evidence presented here and in previous studies indicate the defect is likely to be of interstitial origin, formed as a result of the plastic deformation. The observation of this defect is additional evidence of the generation of interstitials during the deformation.

In the untreated sample, the H3 peak was found to split near the interfaces between the bands, Figure 5.4 (d). Davies et al. [182] investigated the stress splitting of the H3 energy levels for stresses applied along various directions. In the untreated sample, the maximum difference found between the H3 peak and the split component is about 1 nm (or 5 meV) and the maximum stress values measured from the Raman mapping in these regions is $\sim$ 300 MPa. These values are consistent with those found by Davies et al. [182], for the splitting of the H3 line in response to stress applied along a $\langle 110 \rangle$ direction. Burgers vectors are $\langle 110 \rangle$ type for dislocations in diamond, the splitting may therefore be caused by the dislocations. The additional peak may also be caused by the presence of interstitials, generated in the brown bands. The 3H defect is an interstitial related defect [78] and produces a peak with ZPL at 503.2 nm. The 3H defect is stable up to temperatures of 800 °C so could remain stable under the conditions of plastic deformation [183]. Owing to the close match in the distribution of the H3 splitting and the regions of increased Raman line width, the stress-splitting hypothesis is favoured over the presence of the 3H defect.

Mapping of the integrated intensity between 500 - 506 nm suggest a slight increase in the concentration of the H3 centre in the brown bands due to vacancy generation, in agreement with other literature [85–87,184]. The contrast between the H3 intensity between the brown and colourless bands is low, likely a result of the diamond being of type IIa, with very little nitrogen being present to form H3 despite the vacancy generation occurring in the brown bands.

The distribution of N3 centres appears to be affected by the plastic deformation, although it is not entirely clear if the distributions observed are due to the plastic deformation or quenching due to dislocations. It has been suggested that plastic deformation can break-up B-centres, forming H3, N3 and single N defects [46], however the N3 defect is found with similar intensities within the brown and colourless bands suggesting this mechanism is not at play. The similar concentration between the brown and colourless bands of the N3 centre suggests the formation is

dependent on the presence and migration of nitrogen, rather than any interstitial or vacancy enhanced migration. Being type IIa diamonds, with low nitrogen content, any differences in N3 production caused by the plastic deformation may be much smaller, and less obvious, than that seen in type I diamond.

5.3.2 Band A Emission

Band A emission is commonly observed in both natural diamond and homoepitaxially grown single crystal and polycrystalline CVD diamond [25,86,185]. Although the exact origin of the emission is not known, it has been associated with sp^2 carbon from dislocations and grain boundaries [136,186]. Early theories of the Band A origin attributed the emission to an atmosphere of donor-acceptor pairs [187], or vacancies [188] around the dislocations. Figure 5.11 shows that colourless bands are roughly 50% more luminescent than brown bands in the untreated sample, and the difference reduces to only 10% in HPHT treated sample. Since the Band A emission is commonly associated with dislocations and grain boundaries, and no clear change in dislocation microstructure is observed after treatment, structural differences between the straight dislocation dipoles and curved dislocation tangles observed between the brown and colourless bands should be considered as a possible reason for the difference in Band A emission. The results here suggest that curved dislocations are stronger emitters of Band A emission than straight dislocations. This result is is contrast to Yamamoto et al. [187] who found that straight dislocations were stronger emitters than curved dislocations.

Dislocations viewed in similar type IIa diamond show that the dislocation cores are non-radiative recombination centres while the material surrounding dislocations luminescence [189], a point defect atmosphere around the dislocations may be an alternative explanation for the luminescence, with the curvature or straightness of the dislocation affecting the luminescence of the atmosphere.

5.3.3 Effect of HPHT treatment on the Microstructure

HPHT treatment produces several changes to the defect microstructures observed. Figure 5.5 shows a reduction in the intensity of the brown colouration and strain observed, although both the colour and strain is not completely removed under the treatment conditions. PL shows the removal of the 406.3, 491.3 and 535.9 nm lines, which had been attributed to the deformation, and a significant reduction in the H3 and N3 concentration. These 3 lines are removed by the heat treatment indicating their break-up at temperatures below 2000 °C. Raman mapping shows a reduction

in internal stresses after treatment, which is consistent with the break-up of vacancy clusters and point defect complexes, and the "healing" of some of the damage caused by the deformation.

Lower magnification TEM imaging shows that the dislocation microstructure is relatively unchanged by the HPHT treatment, however changes may be occurring on smaller length scales. The critical annihilation height, h_c of dipoles is temperature dependent, and the smaller dipoles may have annihilated during treatment. While HPHT treatment has been shown to remove the vacancy clusters [26], the results here do not fully explain how the vacancy clusters are broken up or what happens to the excess vacancies released. One suggestion proposed is Oswald ripening of the clusters until their eventual collapse into dislocation loops [18,31]. However, from Figure 5.14, it is not clear if a greater number of small dislocation loops or dipoles are observed post treatment.

Further detailed investigation into the nature of the dislocation dipoles both before and after treatment, as well as any changes occurring to the core structure of the defects, are required.

5.4 Chapter Summary

Correlative microscopy has been used to image the point defect distributions and dislocation microstructures in a "zebra" diamond containing both brown and colourless bands. Clear evidence of plastic deformation is observed visually, by the appearance of slip bands, while Raman mapping shows considerable internal stresses consistent with higher point defect concentrations. Large numbers of dislocation dipoles are observed in the brown bands, indicative of dislocation movement during plastic deformation and the generation of intrinsic point defects. Vacancies generated during the plastic deformation likely agglomerate into the vacancy clusters responsible for the colouration, while some are trapped at nitrogen impurities forming point defect complexes. H3 is one such defect found in larger concentrations in the brown bands. Lines at 406.3 nm and 491.3 nm are observed in the untreated sample and are likely to be the result of plastic deformation, however the exact origin of these lines is unknown. The intensity of these lines is too weak to map however they do appear to be present in other plastically deformed diamonds [14,85,88,177]. A strong line at 535.9 nm is strongly correlated with the brown bands. Based on the TEM microstructure and PL results obtained, it seems likely that the defect is of interstitial nature. After heat treatment these lines are annealed out. Further work is required to examine changes to the extended defect core structures.

Chapter 6

Electron Microscopy Study of BDD Surface Processing for Electrochemical Applications

6.1 Introduction

Diamond for non-mechanical technological applications is traditionally grown using chemical vapour deposition (CVD) in either a single crystal (grown homoepitaxially on diamond substrates) or polycrystalline form (grown heteroepitaxially on non-diamond supports). Polycrystalline diamond can be grown in both thin and thick film format [190,191], thick films can be removed from the support material and handled as free-standing material. Heteroepitaxial growth on non-diamond substrates allows for the possible production of large wafers of polycrystalline diamond that can be grown more cheaply.

Doping diamond with a large concentration of boron can change diamond from a wide band gap insulator to a material with metal-like conductivity [191]. Combined with diamond's extreme properties such as hardness and thermal conductivity, this has made boron doped diamond (BDD) an attractive material for use as an electrode material in electrochemical applications. Other favourable properties that make BDD ideal for use in electrochemical applications are a wide solvent window, low background current, reduced fouling, and the fact that it is non-corroding and bio-inert [23,192]. As such, BDD, grown heteroepitaxially, has found use in pH sensing, heavy metal detection and water purification, to name a few [23].

The presence of sp^2 carbon on the surface of BDD electrodes is generally detrimental to the properties of the electrode, leading to a reduced solvent window,

increased background currents and greater susceptibility to corrosion [192]. The introduction of small amounts of sp^2 carbon can however be advantageous for some applications. For example, sp^2 carbon can increase the sensitivity of the electrode to some important reactions such as oxygen reduction [193] and advanced oxidation processes [194]. sp^2 carbon can also facilitate a wider range of surface functional groups than the diamond surface. Quinones are one such functional group which is electroactive and can be used to facilitate electrochemical reactions, for example in pH sensing [195,196]. Quinones are a class of organic compound which are composed of benzene ring structures and contain an even number of C=O bonds, these double bonds allow electron transfer between the surface and the reactants to occur [197].

For BDD to see widespread use as an electrode material, the material must be able to be processed into structures appropriate for the intended use; the state of the surface under different processing conditions must also be understood so that reproducible electrodes can be manufactured. Additional control over the sp^2 carbon content of the surface would allow electrodes to be tailored for different applications. Nanosecond (ns)-laser micromachining [198–201] is a technique commonly used in the manufacture of BDD electrodes, able to cut and structure wafer scale diamond (and BDD) films into much smaller, useable geometries [202–205].

ns-laser micromachining has been shown to introduce non-diamond sp^2 carbon onto the laser cut diamond surface [192,195,202,205–212]. This is attributed to thermal damage by the laser beam, with a solid-to-solid conversion of diamond to graphite occurring at 700°C in air [202]. Sublimation of the resulting graphite is reported to occur at temperatures > 3650°C. This process repeats, on the timescale of the laser pulse. Transmission electron microscopy (TEM) of the ns-laser cut diamond surface reveals the surface has been converted into a highly ordered graphitic carbon layer [202,207], still attached to the bulk diamond, with the uppermost surface covered by a layer of porous, amorphous carbon/graphite [202,207,209]. More costly femtosecond (fs)-laser machining methods can be used instead of ns lasermachining with the advantage that less sp^2 carbon is produced on the surface, owing to the diamond ablation occurring without graphitization [213–215]. This is only true for low laser power levels, which subsequently leads to slower material removal rates. Many fs-laser studies actually demonstrate that sp^2 carbon can still be created after ablation [216–218] under high fluence conditions. Issues with sp^2 contamination also affect diamond nanoparticles (NPs) where the methods of production tend to leave the NPs covered in a layer of graphite-like carbon [219,220].

The ns-laser cutting of diamond can introduce unwanted sp^2 carbon onto the surface of the diamond, however it has also been used to intentionally create

arrays of microspots of sp^2 bonded carbon by patterned laser ablation of the BDD electrode in order to increase the electrochemical sensitivity of the electrode towards pH[195,196], dissolved oxygen[193] and hypochlorite[221].

For many applications of diamond and BDD however, the removal of any processing-created or growth-related forms of sp^2 bonded carbon at the surface is essential.

In this chapter, TEM imaging and EELS has been used to investigate a cross section of BDD surface after various processing stages to determine the effectiveness of two different oxidative treatments for the removal of surface sp^2 carbon. ns-laser micromachining process was used to deliberately introduce sp^2 onto the surface. The first treatment is a high temperature ($> 200°C$) acid oxidation of the BDD in sulphuric and nitric acids, a treatment which is commonly used as a cleaning procedure for diamond/BDD[222]. The second treatment is high temperature (up to 600°C) thermal oxidation of the diamond in air. Both treatments are cheaper and more accessible alternatives to the use of a hydrogen plasma system, which can and has been used previously for sp^2 carbon removal[223–225].

BDD has been used in this study to determine the overall effectiveness of the treatments, due to its conducting nature and use as an electrode material. The electrochemical signature of quinone groups provides a mechanism by which the overall sp^2 content of the surface can be examined, while TEM is used to determine the form and composition of the surface on small scales. The electrochemical data is provided alongside the TEM data to show the overall quality of the surface.

6.2 Materials and Methods

The electron microscopy techniques used in this chapter have already been described in Chapter 3, however several additional measures were implemented in the preparation of the samples examined here. This section will describe those additional measures, the surface processing treatments and BDD material used in this Chapter. Further details of the electrochemical measurements, The ns-laser ablation process, electrochemistry measurements and materials used can be found in Cobb et al. (2020)[226].

6.2.1 Diamond Electrode Material

The electrodes examined were prepared from electroanalysis grade BDD (grown using CVD by Element Six (E6) Ltd., Harwell, UK) which contains minimal sp^2 content. The BDD was provided as a freestanding (370 μm thick, 130 mm diam-

eter) wafer which was mechanically polished to $\sim$ nm growth face roughness and metallically doped with ca. 3×10^{20} boron atoms cm^{-3} [227]. ns-laser micromachining was used to cut out smaller electrodes and introduce sp^2 onto their surface before undergoing the various oxidation treatments.

6.2.2 Oxidative Acid Treatment

BDD laser machined electrodes were acid oxidised at $\sim$200°C, in concentrated H_2SO_4 (98%) saturated with KNO_3 for a time of 30 minutes; equating to exhaustion of all the KNO_3 in solution. For time dependant experiments, acid oxidation times of 15 minutes, 2 hours and 24 hours were also employed, using the same solution. Finally, measurements were also made using solutions which had the exhausted KNO_3 refreshed every 30 mins (up to n=4 treatments).

6.2.3 Thermal Oxidation Treatment

BDD laser machined electrodes were thermally oxidised in air, in a tube furnace oven, (Thermo, Lindberg Blue/M) at temperatures over the range 400°C to 600°C for 5 hours each. For a fixed temperature of 600°C, the thermal oxidation time was also varied between 15 minutes to 5 hours.

6.2.4 TEM Sample Preparation

TEM lamella were prepared using FIB lift-out procedures as described in Section 3.5.1. However several additional measures were implemented to protect the surface from any possible ion-beam induced damage of the surface that could be mistaken for laser ablated damage.

For each stage of the surface processing that was examined, FIB lamellae were prepared from a fresh electrode to ensure that any changes occurring were not as a result of contamination/damage from any prior FIB processing.

Before FIB milling commenced, a thin layer of e-beam Pt was deposited before a further 1 - 2 um protective layer of ion-beam deposited Pt. These layers were deposited in the FIB. For the oxidatively treated samples, an additional layer of Al (from 20 nm to several hundred nm's) was sputtered/evaporated onto the surface before the sample was put in the FIB - before any Pt layer deposition and any FIB milling had occurred. The purpose of the this Al layer was two-fold, firstly acting as an additional protective barrier to protect the surface and secondly as a barrier to separate the surface from the Pt protective layer deposited during the FIB process. Pt layers deposited in the FIB typically contain a high sp^2 carbon

content due to the breakdown of the organic-Pt precursor gas[228]. As such, the deposited Pt layer can contain a significant amount of carbon, sometimes up to 70% carbon. This carbon will likely contain a significant fraction of sp^2 bonding. If the Pt layer is not separated from the processed surface, differentiating between the sp^2 carbon generated from the laser micromachining with the sp^2 carbon from the Pt protective layer deposited during the FIB prep would be problematic and could lead to confusion in the analysis, increasing the potential for mistaking features of the Pt layer for damage caused by the processing.

A summary of the samples looked at and the points at which the samples were obtained from is given in Figure 6.1.

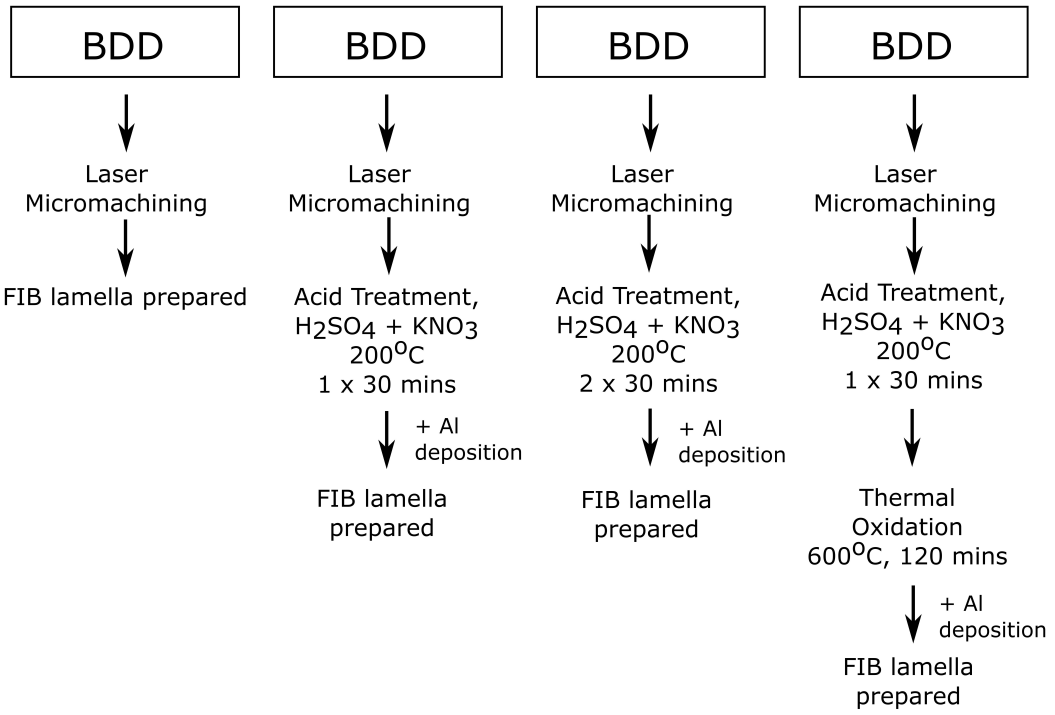

Figure 6.1: Schematic showing the laser machining processing steps and the points at which FIB sections were produced

6.3 Results

6.3.1 ns-Laser Machining on the BDD Surface

A HAADF image of a cross section of the laser micromachined BDD surface is shown in Figure 6.2 (a) and shows several layers of laser induced damage. The unaltered

BDD can be seen at the bottom of Figure 6.2 (a), on top of which are two layers of damage (I and II). The protective Pt layer from the FIB preparation process appears at the top of 6.2 (a), and appears bright due to HAADF imaging's sensitivity to atomic number. An Al layer was not deposited on this sample since the interfaces of interest, between the underlying BDD and layer I, and between layer I and II, are far from the Pt. Layer II is also thick enough that all EELS analysis can be carried out far from the Pt layer without having to worry about its carbon content.

The darker contrast of layers I and II in the HAADF image, Figure 6.2 (a), compared to the BDD, indicates that less electrons are being scattered to large angles. This suggests that layers I and II are either made up of material with smaller Z number (lighter atoms) or are composed of carbon in a form that is less dense than the diamond. Compared to the number of carbon atoms in the lattice, only a small amount of boron will be present, so the contrast of layers I and II is unlikely to be due to z-number contrast and instead is due to changes in the density of the material. Layers I and II are therefore less dense forms of carbon, such as graphite or amorphous carbon.

EELS SI was used to determine and map the composition of the BDD, layer I, and layer II. SI was carried out in the region shown in Figure 6.2 (a). Averaged EELS spectra taken from the BDD (green), layer I (blue) and layer II (red) can be seen in Figure 6.2 (b) and are found to be consistent with the EELS spectra of diamond, graphite (layer I) and amorphous carbon (layer II) respectively [122]. sp^2 carbon can be identified in the EELS spectrum from the 1s-π^* peak at approx. 285 eV [118,122,229], a transition which is only seen in sp^2 bonded carbon.

Mapping of the different phases of carbon was carried out by the use of Multi Linear Least Squares (MLLS) fitting within the Digital Micrograph software. For each pixel in the spectrum image, the spectrum is fitted using a linear combination of reference spectra. The magnitudes of the fitting coefficients for each reference spectra can then be used to map the distribution of each reference spectra. The MLLS fit process for the three phases of carbon present in Figure 6.2 (c) is given below in Equation 6.1.

$$F(E) = C_{BDD}S_{BDD}(E) + C_{graphite}S_{graphite}(E) + C_{ac}S_{ac}(E) \tag{6.1}$$

Where F(E) is the spectra at each pixel in the image, C_i is the fitting coefficient for phase i and S_i is the reference spectra for each phase i of carbon. Using the diamond, graphite and amorphous carbon spectra, seen in Figure 6.2 (b), as ref-

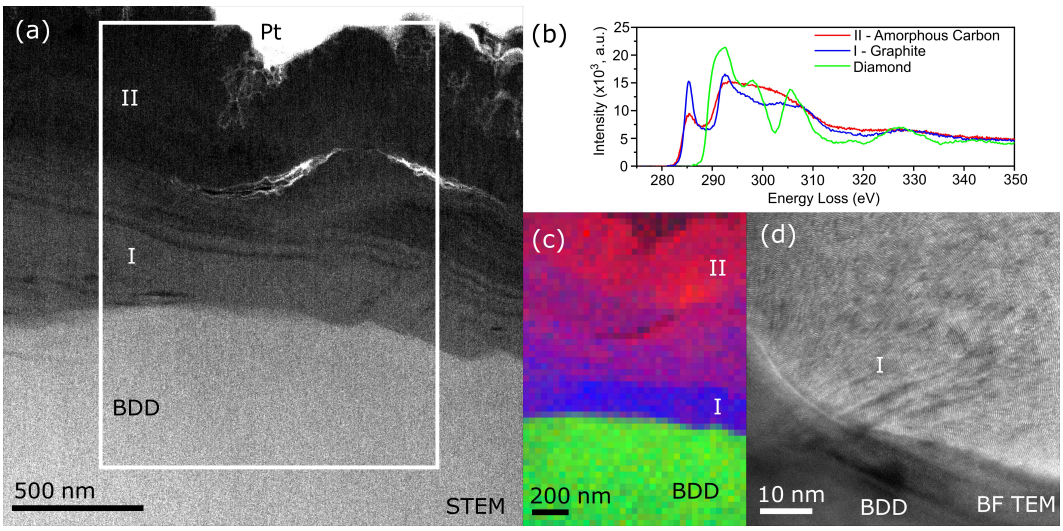

Figure 6.2: a) HAADF STEM image of laser ablated BDD surface, white rectangle indicates the EELS survey area. b) EELS spectra of BDD (green), graphite (blue) and amorphous carbon (red), obtained from the BDD substrate, layers I and II respectively. For comparison of the fine edge structure, the graphite and amorphous carbon spectra have been multiplied by a constant, to give them a similar intensity to the diamond spectrum. c) Map overlaying the coefficients of the Multi Linear Least Squares (MLLS) fitting of the 3 spectra in b), showing the distribution of BDD (green), graphite (blue) and amorphous carbon (red). d) High magnification BF TEM image of layer I showing highly orientated planes of graphite, with plane spacing 0.34 - 0.39 nm, in agreement with the EELS analysis.

erence spectra, the fit coefficients from the MLLS fit have been plotted as a colour map, Figure 6.2 (c), and show how each of the different carbon phases is distributed (crystalline BDD - green, crystalline graphite - blue, and amorphous carbon - red).

Figure 6.2 (c) shows that a $\sim$ 200 nm thick layer of almost pure graphite is formed directly on top of the BDD, attributed to the ns-laser induced solid-solid phase transition of BDD to graphite. Moving further up from the BDD towards Layer II, Figure 6.2 (c) indicates a gradual change from graphite to amorphous carbon over several hundred nm. The MLLS fit indicates that the upper section of layer II is primarily amorphous in nature.

Conventional Bright Field (BF) TEM imaging of layer I, Figure 6.2 (d), confirms the results from EELS, that layer I is composed of graphite. Along the BDD-layer I interface, the graphite can be found with its basal plane orientated either parallel and/or perpendicular to the BDD. FFT analysis gives the basal plane spacing to be between 0.34 - 0.39 nm, consistent with that of graphite[230]. Away

from the interface the graphite is orientated at predominantly $\sim 45^{\circ}$ to the BDD over large areas (100s nm) suggesting that crystallization occurs over relatively long timescales, much longer than individual ns laser pulses. No preferential crystallographic orientation for the BDD is seen.

6.3.2 Single Acid Oxidation Treatment on the BDD Surface

Electrochemically, the surface after a single acid treatment was found to still contain sp^2 carbon. Figure 6.3 (a) shows an ADF STEM image of a cross-section of the BDD material after an acid oxidation of 30 minutes. The surface now shows a continuous dark layer of varying thickness between the BDD and Al layer, again indicating the presence of a less dense form of carbon. This dark layer was composed of clusters of thicker material (up to 40nm thick) connected by thin layers (a few nm) on the BDD surface. MLLS fitting, using the same spectra as seen in Figure 6.2 (b), indicates that the thick dark clusters are comprised primarily of graphite; with the averaged EELS spectra obtained from these clusters being similar to that found for the graphite in layer I, Figure 6.3 (b). TEM imaging shows the clusters to be made of graphite, in agreement with the the EELS analysis, Figure 6.3 (c, d). In all of the observed clusters in this sample, the graphite was found to be bonded directly with the BDD, with its basal plane perpendicular to the BDD surface, Figure 6.3 (c, d), suggesting the survivability of these clusters to acid oxidation may be linked with the graphites orientation with the BDD.

From comparison with the ns-machined only sample, the amorphous carbon layer (layer II) has been completely removed and it appears that the clusters are remnants of graphite (layer I) that have survived the oxidative acid treatment. Closer inspection of these perpendicularly orientated graphite clusters appear to show to them encapsulated by an amorphous carbon shell, approximately 5 nm in thickness (Figure 6.3 (c), inset). This shell can also be seen in the EELS MLLS fit (Figure 6.3 (a) inset) as an increase in the fit coefficient of the amorphous carbon signal directly adjacent to the graphite signal. The averaged EELS spectrum from the area of the amorphous shell also appears to be similar to that of amorphous carbon, Figure 6.3 (b) (red).

From the EELS spectrum it is possible to calculate the sp^2 fraction of the different carbon phases. The sp^2 fraction is defined as the fraction of the total number of carbon atoms, within the column of material the electron beam travels through, that are sp^2 bonded. The sp^2 fraction is calculated from the ratio of two windows of the carbon K-edge, one centred on the sp^2 peak (3 eV in width) and the other encompassing the rest of the K-edge (30 eV in width). The formula to

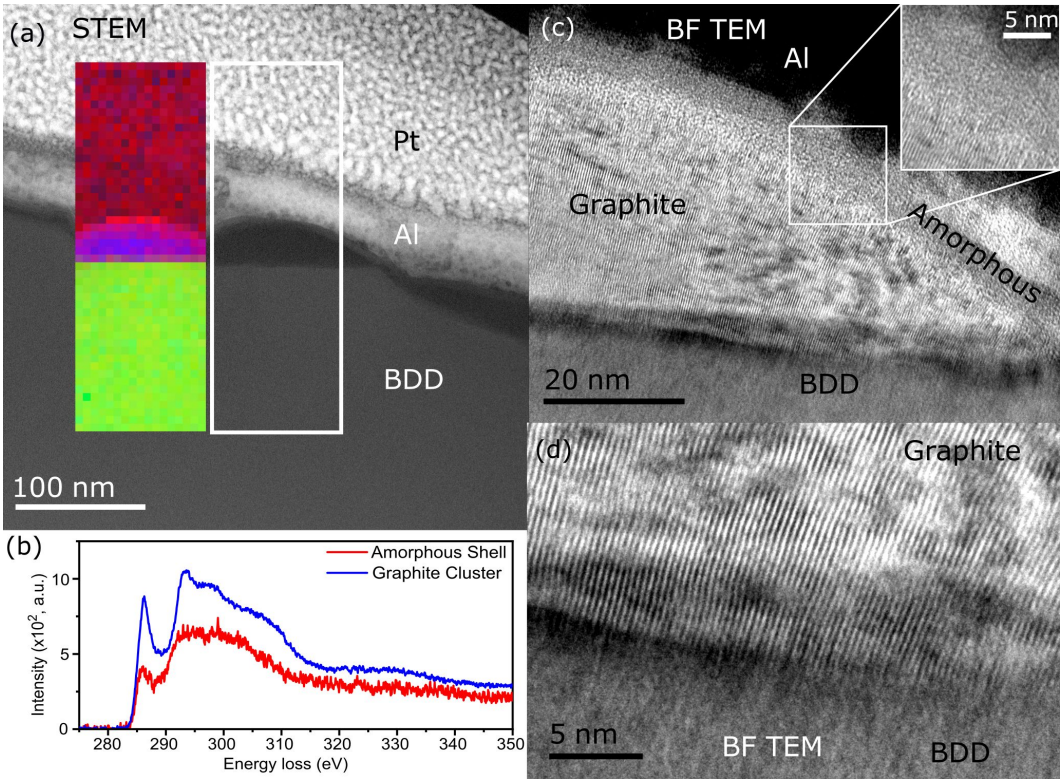

Figure 6.3: a) HAADF STEM image of ns laser micromachined BDD after acid cleaning, Inset: shows the MLLS fit using the diamond, graphite and amorphous carbon spectrum. b) EELS spectrum obtained from the graphite cluster (blue) and the spectrum from the amorphous shell (red). Amorphous carbon spectrum has been multiplied by a constant to an intensity similar to the graphite spectrum, to allow comparison of the fine edge structure. c) High resolution TEM image showing the graphite cluster with basal planes perpendicular to BDD interface and a thin amorphous top layer. Inset shows the amorphous shell-graphite interface. d) BF-TEM image showing the graphite-BDD interface.

calculate the sp^2 is given by [231]:

$$\frac{I_\pi(\Delta E_1)}{I_\sigma(\Delta E_2)} = k\frac{X}{4-X} \tag{6.2}$$

where$X$ is the sp^2 fraction and k is a ratio between the intensity of EELS signal in the windows and the sp^2. The ratio k must be normalised by using a 100% sp^2 carbon material. The graphite layer (I) from the ns laser micromachined sample (Figure 6.2) was used as a 100% sp^2 reference material. The normalised ratio is given by setting X to 1.

$$R = \frac{3X}{4 - X} \tag{6.3}$$

So that,

$$\frac{I_\pi(\Delta E_1)}{I_\sigma(\Delta E_2)} = \frac{3X}{4 - X} \frac{I_\pi^{ref100\%}(\Delta E_1)}{I_\sigma^{ref100\%}(\Delta E_2)} \tag{6.4}$$

The sp^2 bonded carbon fraction of this encapsulating amorphous shell was found to be $\sim 70\%$ sp^2 bonded carbon, while that of the amorphous carbon layer in Figure 6.2 (layer II) was $\sim 80\%$. TEM imaging and EELS analysis of the thin layers between the clusters was not able to resolve any planes of graphite or determine the nature of this material. This thin connecting layer between the clusters is speculated to be composed of the same amorphous carbon that makes up the encapsulating shell, and is similarly formed by the conversion of the graphite by the acid.

6.3.3 Double Acid Oxidation Treatment on the BDD Surface

Electrochemical measurements of the quinone surface coverage, Γ, indicate that sp^2 carbon still remains on the surface regardless of the length or number of acid treatments carried out, Figure 6.4. TEM and EELS mapping was therefore carried out on a sample which had undergone two acid treatments, with the solution being replenished after the first 30-minute treatment, to investigate if the graphite clusters underwent any change with repeated treatment. Figure 6.5 shows the results of TEM imaging and EELS mapping on the surface of a laser ablated BDD surface after two acid treatments.

STEM imaging of the surface found dark clusters on the surface after a second acid treatment, Figure 6.5 (a), like that seen in the previous sample. These clusters were confirmed to be graphite by EELS, Figure 6.5 (a) overlay and top inset, and TEM imaging, Figure 6.5 (a) bottom inset, showing their continued resistance to removal by acid oxidation. The size of the observed clusters is the same as that found for the singly acid treated sample indicating that no further changes are induced by further treatment. Similar to the singly acid treated sample, the graphite was orientated with its basal plane perpendicular to the surface, Figure 6.5 (a) bottom inset, strengthening the argument that the orientation is a factor in the survivability of the graphite to acid oxidation. An amorphous capping layer could not be seen by either TEM imaging or EELS, however the shape of the cluster may have obscured this layer. Although the diamond-graphite interface appears to have been imaged edge-on, the graphite-amorphous interface may not have, due to the shape of the

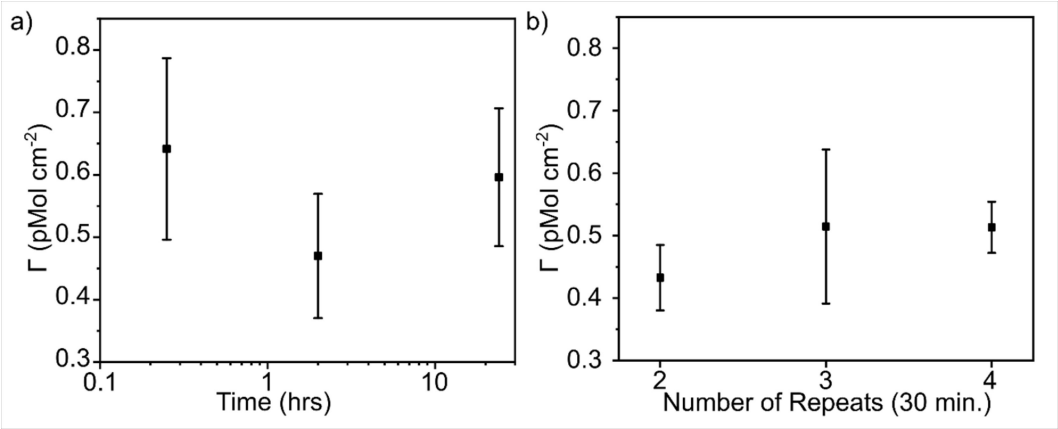

Figure 6.4: (a) Effect of different acid cleaning times on the quinone surface coverage, Γ, demonstrating no effect from a longer acid clean and (b) the effect of repeated 30 minute acid treatments on Γ, with no statistically significant difference on repeated cleaning.

cluster.

In addition to the clusters, small cracks in the diamond were also observed in this sample, Figure 6.5 (b), the dark contrast of the STEM images suggested these cracks were filled with lower density carbon material. The EELS spectrum of the region, Figure 6.5 (b) bottom inset, shows a spectrum that looks close to that of diamond with the addition of a large sp^2 peak. Since the EELS spectrum obtained at each pixel is from a column of material through the lamella, if the beam is not aligned parallel to the crack walls, or the crack doesn't propagate through the entire lamella, energy losses will be measured from both the diamond (around the crack) and sp^2 material within the crack. MLLS fitting using the diamond and graphite reference spectra indicates that the crack is filled with graphite, Figure 6.5 (c).

It is difficult to deconvolve the spectrum into component spectra, so TEM imaging was used to identify the material within the crack. Figure 6.5 (b) top inset shows that the crack is filled with graphite, its basal plane orientated along the direction of the crack. This difference between the EELS analysis and TEM imaging show the importance of combining multiple techniques (where applicable).

A thin bright layer can be observed in the STEM images at the interface between the deposited Al and the BDD, Figures 6.5 (a,b). EDX mapping away from a graphite cluster, identified this bright layer as Au, Figure 6.6. The Au layer is believed to originate from the Al sputterer/evaporator, the equipment is used to deposit both Au and Al, and it appears only to be deposited in the initial stages of

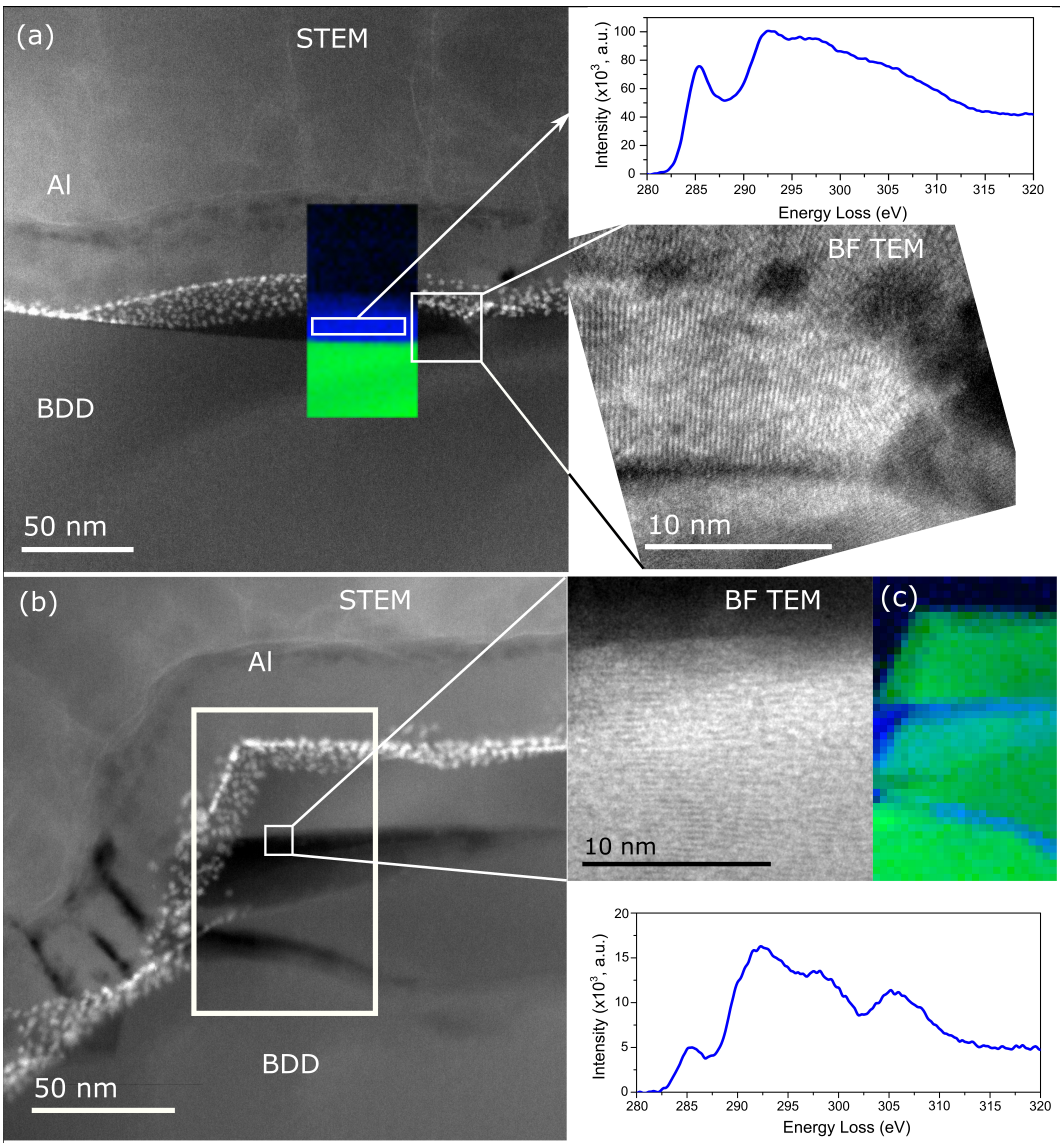

Figure 6.5: a) HAADF STEM image of a graphite clusters after a second acid cleaning, Inset (top): shows the EELS spectrum obtained from the cluster. Inset (bottom): BF TEM image showing the graphite planes (b) HAADF STEM image of a crack in the BDD surface. Inset (top) EELS spectrum from the crack. Inset (bottom) EELS spectrum from the crack. (c) MLLS fit of the crack region using the graphite EELS spectrum from the laser ablated surface.

the Al deposition before either the residual Au in the chamber is used up or the Al deposition fixes the Au to the walls of the chamber. The Au layer has an unexpected advantage in that it closely follows the morphology of the surface so provides limited

3 dimensional information about the shape of the cluster. The arrangement of the Au on top of the graphite clusters suggests that the graphite clusters are dome shaped. The Au can easily be differentiated from the Al and carbon in HAADF imaging due to its higher atomic number however this does prevent the interface between the Al and BDD from being observed clearly in ADF and HAADF imaging.

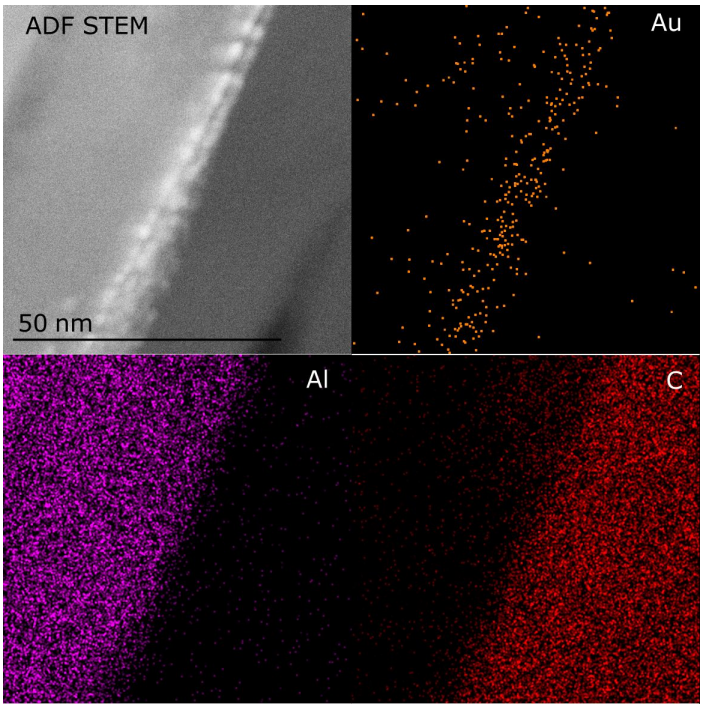

Figure 6.6: EDX maps showing the presence of Au contamination at the interface between the BDD and Al layer

6.3.4 Thermal Oxidation on the BDD Surface

Thermal oxidation was carried out on the singly acid cleaned BDD surface to investigate its effectiveness at removing the remaining, stable graphite clusters from the surface. Electrochemical quinone Γ measurements indicated that the optimal parameters for the complete removal of all remaining sp^2 carbon was a temperature of 600°C and a duration of 2 hours. In air, temperatures of 700°C have been shown to result in rapid graphitisation of the diamond [232], so temperatures above 600°C were investigated. The electrochemical measurement showing the optical parameters are summarised in Figure 6.7, which shows the Γ, after different treatment temperatures at a fixed time of 5 hours, and Figure 6.8, which shows Γ after different durations of treatment for a fixed temperature of 600°C.

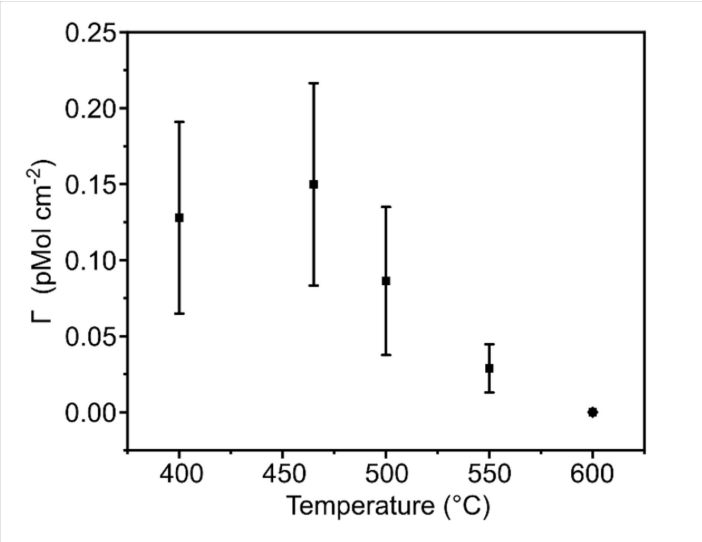

Figure 6.7: Γ measurements after 5 hours at different thermal oxidation temperatures. At 600°C the level of quinone surface coverage, Γ, is below the detection sensitivity of the measuring techniques.

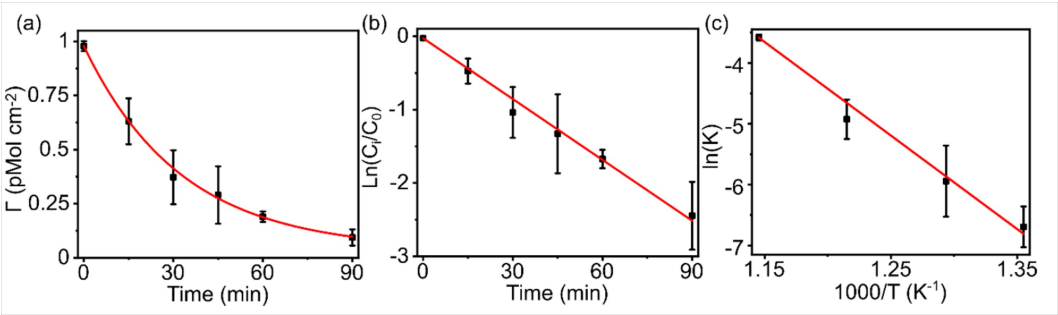

Figure 6.8: (a) Exponential decay of Γ upon thermal oxidation at 600°C, which can be used to infer on the removal of surface sp^2 bonded carbon (b) first order dependence of Γ on time (c) Arrhenius plot.

Figure 6.9 (a) shows an ADF image of the cross section of the BDD surface after 2 hours of thermal oxidation at 600°C in air. An Al layer was deposited on the surface prior to FIB milling and, similar to the double acid cleaned sample, a thin layer of Au contamination was observed at the interface. No clusters of graphite or cracks were observed after the thermal oxidation process.

EELS SI was carried out over a region of the surface to measure the sp^2 fraction leading up the surface. EELS spectra were averaged parallel to the surface and the sp^2 fraction calculated for the material within 32 nm of the surface, starting

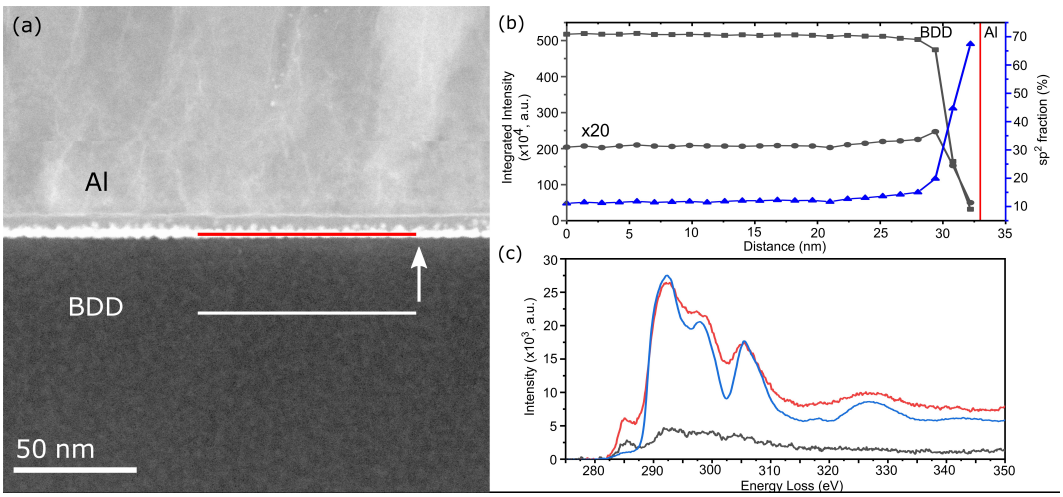

Figure 6.9: (a) ADF STEM image of the interface between thermally oxidized BDD and the Al protecting layer. The BDD was first ns laser micromachined then subject to an acid oxidative treatment. The bright layer is Au contamination from the Al protection process. No large clusters of graphite are observed on the BDD surface. Depth at which the sp^2 fraction of the material was calculated is indicated by white and red horizontal lines. (b) Plot showing the sp^2 fraction (triangles) of the material, integrated sp^2 signal (284-289 eV, circles) and the integrated carbon K-edge signal (280-340 eV, squares) approaching the interface with Al (indicated by the vertical red line). Approaching the surface (BDD - Al interface), both the carbon K-edge signal and sp^2 signal decrease, however the fraction the carbon at the surface that is sp^2 bonded increases. (c) EELS spectra from distances of 1.4 nm (black), 2.8 nm (red) and 28 nm (blue) from the diamond-Al interface (solid vertical red line in (b)). Spectra have been obtained by integrating several spectra from the same depth in the sample and multiplied by a constant to allow comparison of the fine edge structure.

from within the BDD and running perpendicularly up to the Al layer, depth indicated in Figure 6.9 (a). The integrated carbon K-edge signal, integrated sp^2 signal and sp^2 is plotted in Figure 6.9 (b), the interface between the BDD and Al layer is denoted by the solid red vertical line.

An sp^2 bonded carbon fraction (of approx. 10%) was measured within the bulk BDD material (Figure 6.9 (b)) which is most likely to be FIB-induced damage at the surface of the lamella during TEM specimen preparation. Similar values were measured in the bulk BDD in the previous samples. As shown in Figure 6.9 (b), the carbon K-edge (squares) signal and sp^2 (circles) signal both decrease approaching the surface (BDD-Al interface, red vertical line), as expected, while the sp^2 fraction (blue triangles) is shown to increase within 2 - 3 nm of the surface. Both

observations could be indicative of a thin layer (< 3 nm) of surface contaminants as regardless of surface termination, hydrocarbons, water, etc. are readily absorbed onto the diamond surface upon exposure to atmosphere[233,234]. The sp^2 fraction of this surface contaminants layer lies between 20 - 70%.

The solid red vertical line in Figure 6.9 (b) denotes the edge of the Al layer, where the carbon K-edge signal decreases to zero, i.e. no C is detected. Averaged EELS spectra were recorded across lines containing twenty-six pixels running parallel to the edge of this layer at three different separation distances, 1.4 nm, 2.8 nm and 28 nm (Figure 6.9 (c)). At 28 nm the averaged spectra from the BDD are, as expected, characteristic of diamond, (blue line). The integrated EELS spectra 2.8 nm from the surface retains many of the features seen in the diamond spectrum, Figure 6.9 (c) (red), with the addition of the pre-edge 1s $\rightarrow \pi^*$ transition (284 - 289 eV) indicative of sp^2 bonded carbon. At this distance, an sp^2 bonded carbon fraction of 45% is measured, however the pixel size may be larger than the surface roughness meaning energy losses from both the BDD and surface contaminants are being detected. 1.4 nm from the line, the spectrum is close to that of amorphous carbon, Figure 6.9 (c) (black), with an sp^2 fraction of 70% measured. The thickness over which this sp^2 bonded carbon signal can be seen at the interface may be an effect of the tilt being slightly off-parallel to the interface, and the contamination layer may occur over a depth less than 3 nm from the surface.

6.4 Discussion

TEM and electrochemical results show good agreement as to the state of the diamond surface following each surface treatment step. The results of sections 6.3.1, 6.3.2, 6.3.3 and 6.3.4 are summarised in Figure 6.10, which shows the changes occurring to the surface after each processing stage.

Laser ablation of the starting BDD material results in a solid-solid transition of the diamond into highly ordered graphite. Sublimated carbon is redeposited on top of the graphite with a porous amorphous structure. The transition from diamond to graphite occurs as described by Butler-Smith et al. (2013)[202]. The measured plane spacing shows slight variations between 0.34 - 0.39 nm. Expansion of the plane spacing of graphite has been observed after hydrogen irradiation, with the expansion being caused by the hydrogen forming sp^3 C-H bonds with carbon atoms in the plane[230]. CVD growth of BDD uses hydrogen gas to stop any sp^2 from growing and ensuring only sp^3 carbon adds to the diamond lattice. This process may lock up lots of hydrogen in the lattice.

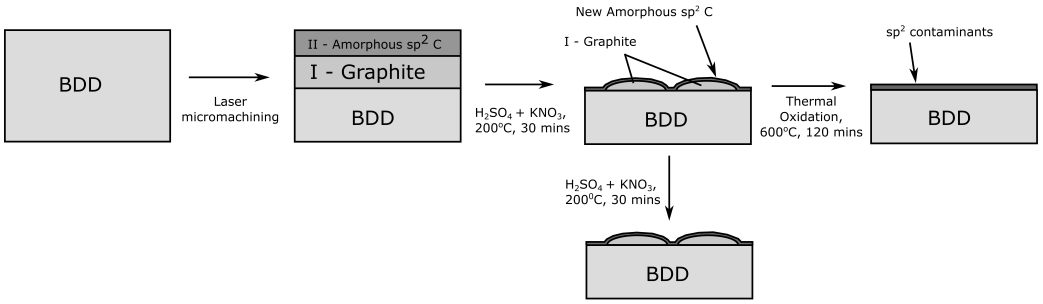

Figure 6.10: Schematic showing the BDD processing and layers identified from TEM imaging of FIB lamellae produced at each stage. Not to scale

The amorphous carbon which makes up layer II is likely the result of re-deposition of carbon from the plasma phase, due to sublimation or vaporization of the graphitic material[202,207]. The composition of the damage layers formed on highly doped BDD observed here are very similar to those produced in non-boron doped diamond subject to ns-laser micromachining, suggesting the mechanism is independent of boron concentration[202,207].

Upon acid treatment the vast majority of the amorphous carbon and graphite is removed leaving behind clusters of graphite that are encapsulated with an amorphous sp^2 carbon shell. For electrochemical purposes, whilst the majority of the remnant clusters are composed of perpendicular-orientated graphite, it is the encapsulating amorphous shell, and not the graphite itself, which interfaces with the electrolyte solution. The oxygen terminated sp^2 bonded carbon surface can play host to a variety of different functional groups including quinones. The electrochemical signal from quinones has been used to measure the surface sp^2 bonded carbon content[192], effectively quantifying the quality of the surface on large scales.

These graphitic clusters are tough and are not removed or altered by any further acid oxidative treatment. TEM imaging and EELS analysis has illuminated several possible reasons for the survivability of the graphite clusters to further acid treatments, which could not be answered by electrochemistry. Firstly, all graphite clusters observed have their planes orientated perpendicularly to the BDD surface. This would allow the graphite planes to form strong C-C bonds and may be prevent the acid from infiltrating between the layers and lifting the planes from the surface. The presence of an amorphous shell around the clusters, which has been termed "denatured graphite", may also protect the graphite planes from exposure to the acid, by preventing the acid from etching the exposed ends of the graphite planes. The sp^2 fraction of this amorphous shell of $\sim 70\%$ and the presence of hydrogen,

from the CVD growth, means this amorphous shells may be a form of diamond-like carbon[235]. This may explain the resistance of the shell to acid.

Cracks observed in the double acid treated sample were filled with graphite suggesting they are a direct result of the laser ablation process, which has caused fracture of the diamond. Cracks are therefore likely to be present in all BDD samples observed, however due to only sampling/imaging a very small area of the surface for each sample the chance of observing a crack is low. It is speculated that an amorphous layer above the graphite crack material has prevented the graphite within the crack being removed during the acid oxidation, similar to the clusters. The presence of these cracks, which propagate to the surface, likely contribute to the sp^2 signal on the surface.

Thermal oxidation at 600°C removes the clusters leaving behind a surface with improved electrochemical performance, associated with minimal sp^2 surface content. The temperatures used are below the threshold for graphitisation so damage to the BDD surface should be minimal.

The TEM and electrochemical data together suggest removal of electrocatalytically active sp^2 carbon, important for any electrochemical application which requires a sp^2 carbon free electrode. While the electrochemical results have been used as a metric of the overall quality of the film, the TEM imaging and EELS results have been able to explain the form of the sp^2 and why it is so resistant to removal. This gives greater confidence that the surface processing stages used will produce reliable and reproducible electrodes. Laser ablation, followed by acid oxidation treatment, produces extremely robust sp^2 clusters, meaning sp^2 surface coverage should be easily tunable for different applications.

Although the effectiveness of acid and thermal oxidation treatments for removing sp^2 carbon was only investigated for BDD, the treatments should apply equally as well to other types of diamond.

6.5 Chapter Summary

TEM imaging and EELS has been used to investigate methods of removing sp^2 bonded carbon from the surface of BDD, in conjunction with electrochemical techniques. ns laser micromachining of BDD, commonly used to cut and structure diamond/BDD, is shown to result in surface damage, and the formation of a $\sim$ micron thick coating of sp^2 bonded carbon. These damaged layers consist of a layer of highly ordered graphite intimately attached to the BDD, on top of which lies a layer of fissured amorphous carbon. Similar structures have been seen on ns laser

micromachined diamond [202]. Oxidative acid treatment (sulfuric acid and potassium nitrate) at elevated temperature, a common cleaning recipe for diamond/BDD, is shown to be ineffective at removing all the sp^2 bonded carbon. Whilst the fissured amorphous layer and parallel-orientated graphite regions are removed completely, the perpendicular orientated graphitic regions ($\sim$ 10s nm in diameter) remain. These are considerably thinner in size and capped with a $\sim$ 5 nm thick layer of amorphous carbon. These clusters are resistant to further oxidative acid treatments. The perpendicular orientation of the graphite and the formation of an amorphous cap layer during the first acid etch are speculated to be the reason for their stability. Removal of the graphite clusters is possible via thermal oxidation in air at 600 °C. TEM detects a very thin ($\sim$ nm) layer of sp^2 bonded carbon at the interface, but this is likely to be due to surface contamination. The electrochemical response (solvent window, double layer capacitance, quinone coverage) of this surface closely resembles that of a minimal sp^2 bonded carbon content BDD electrode.

Both acid and thermal oxidation treatments can be performed with equipment available in the majority of laboratories. As such it offers convenient methods for users to improve the material properties of intrinsic and doped diamond materials after growth or processing for a wide range of applications and materials where the presence of sp^2 carbon is detrimental to material performance.

Chapter 7

Conclusions

The main aim of this research has been the use of electron microscopy techniques, which have been coupled with both correlative microscopy and electrochemistry, to reveal insights into dislocation behaviour in natural plastically deformed diamond and surface processing techniques of synthetic boron doped diamond for electrochemical applications.

In Chapter 4, the generation of point defects by plastic deformation was discussed and a selection of type IIa diamonds with an almost uniform brown colouration were selected for examination. The overall dislocation micro-structure in these samples were indicative of large scale point defect generation caused by plastic deformation, as seen by the presence of dislocation dipoles. Sub-grain boundaries within the material appear to act as forest dislocations through which dislocations move during plastic deformation. Jogs formed during the deformation are dragged with the moving dislocation producing intrinsic point defects, Superjogs can also be produced by the deformation, formed from a combination of several unit jogs, and are completely immobile. As the dislocation containing the superjog continues to move a dislocation dipole will be formed, with the superjog pinned in place at one end of the dipole. The presence of dipoles are clear evidence of point defect generation, being the remnants of the same plastic deformation process that produces the point defects. They are left behind in the crystal because they haven't been dragged or annihilated to form intrinsic point defects.

Both interstitials and vacancies are generated by jog dragging and the formation of either is dependent on the properties of the interacting dislocations, the Burgers vector, line direction and glide plane of each. Although no direct evidence of vacancy generation is observed in this work, atomic resolution imaging of dissociated dislocations and faulted dipoles shows that a large concentration of interstitials

have been absorbed onto the 90° partial dislocations. Estimates of the number of interstitials absorbed onto the 90° partials puts this value at 10^{17} - 10^{19}cm^{-3}, close to the vacancy concentrations measured in brown diamond by PAS, approx. 10^{18}cm^{-3}. Almost equal numbers of interstitials and vacancies appear to have been generated during plastic deformation, and while the interstitials are rapidly absorbed onto the partial dislocations due to the dislocation bias, forming a perfect crystal plane, the vacancies likely aggregate into the vacancy clusters responsible for the brown colouration.

The plastic deformation processes occurring in diamond are the same as those seen in simple fcc metals and semiconductors, suggesting that diamond is not special in this regard. Plastic deformation processes have been studied in other fcc metals such as Cu and Al, which are easily plastically deformed. The results of deformation of other fcc materials can therefore be applied to diamond.

Chapter 5 builds on the results of Chapter 4 by examining the dislocation and point defect distributions in "zebra" diamonds, which show clearly defined bands of brown and colourless material. Observations of the dislocation structures in the two bands showed clear differences. The dislocations in the colourless material were found in a tangled arrangement, with far more curved dislocations, while the dislocations in the brown bands were found predominantly as straight dislocation dipoles. As discussed in Chapter 4, the presence of dipoles is clear evidence of intrinsic point defect generation.

PL point defect mapping provided more evidence of point defect generation. In brown bands, larger concentrations of the H3 centre are found due to a higher concentration of vacancies. The H3 centre is formed by the capture of vacancies at A-centres. A line at 535.9 nm is strongly correlated with the brown bands and the results presented here, and in previous studies, suggest this line is interstitial in nature. As well as being absorbed onto the partial dislocations, the interstitials generated appear to influence the point defects present, being trapped at impurity atoms and forming new point defect complexes. Additional lines at 406.3 and 491.3 nm are also observed which previous studies have attributed to plastic deformation. Their weak PL intensity prevented them from being studied further. The Raman stress mapping corroborates the PL and TEM imaging here. The brown bands are found under compressive stresses, consistent with an expansion of the material, resulting from a higher point defect density and the formation of the vacancy clusters. Similar expansion is observed in irradiated metals due to the formation of large voids. HPHT treatment reduces internal stresses within the material and correlates with the removal of point defects and vacancy clusters, apparent from the removal

of the brown colouration.

CL panchromatic imaging and spectroscopy also raises some interesting observations. The colourless bands appear to be stronger emitters of Band A emission. Although the origin of the Band A emission is not known, the brown bands might have been expected to emit more strongly, as the PL mapping indicates they have higher defect concentrations. HPHT treatment reduces the difference in Band A luminescence between the bands but does not completely remove the emission. Since the dislocation microstructure is one of the most obvious differences between the bands, and also doesn't appreciably change after HPHT treatment, differences in the atomic structure of the dislocations should be considered as a possible origin for the Band A emission.

In Chapter 6, TEM and EELS was used to investigate the BDD electrode surface after different processing stages. For diamond to effectively be used as an electrode material the surface must be well understood and the sp^2 content must be controlled. After laser ablation of the surface using a ns laser, a solid-solid phase transition of the diamond surface occurred leaving behind a thick layer of graphite. This graphite was topped by a porous layer of amorphous carbon, likely redeposition of the sublimated carbon. Acid oxidation treatments were effective in removing the majority of the graphite and amorphous carbon layers, however, clusters of graphite were left behind on the surface. These graphite clusters were found with their basal planes perpendicular to the diamond surface and were capped by a thin layer of amorphous carbon, which we have termed "denatured graphite". It is this denatured graphite which is responsible for the continued sp^2 response of the surface after acid treatment. These graphite clusters are found to be very resilient to prolonged and multiple acid treatments. In some applications an increase in sp^2 carbon can be beneficial and the resilient nature of these clusters mean this surface is likely to remain stable, even working in harsh conditions. Thermal oxidation at 600°C for 2 hours was found to be sufficient to remove all electrochemically detectable sp^2 carbon from the surface. A thin layer of sp^2 carbon was detected by EELS, however this layer is thought to be contamination picked up from the atmosphere and is likely to be loosely bound to the surface. Removal of sp^2 carbon by thermal oxidation was found to work for both a laser ablated BDD surface and BDD surfaces with sp^2 carbon grown-in. These results provide a better understanding about the BDD surface and surface preparation processes for electrochemical applications. Both acid and thermal oxidation can be used to tailor the sp^2 properties of the BDD surface for the application required, whether that is an sp^2 containing or a minimal/zero sp^2 containing surface.

7.1 Future Work

It is clear that in terms of plastic deformation, diamond behaves in the same way as other fcc materials, although under more extreme conditions. However, the work presented here does raise some interesting questions that require further work to answer.

The atomic resolution images of the climbed 90° partial structure does not inform as to the exact structure of the climbed section. Whether individual loops have been nucleated or the climb occurs over the entire length of the dislocation is not known. The size of the climbed section is too small to be observed or investigated using WBDF imaging, so detailed computational modelling of the structure may be the best way to determine its structure. Knowing the atomic structure would reveal if any sp^2 carbon is present, which could introduce states into the band gap. EELS mapping, similar to that seen in chapter 6, at atomic resolutions could also be employed to investigate this. Atomic resolution imaging of these structures would also benefit from thinner samples. Thinner samples would produce better images of the climbed section, better able to resolve the atomic structure of the climbed section, as the chance of finding variations through the thickness of the sample would be reduced. Atomic resolution imaging was only used on FIB produced samples, where it was difficult to achieved thickness's below 100 nm, due to sample warping, and a smooth, clean surface. Argon ion milling was found to be far superior in producing thinner samples, $\approx$ 30 - 50 nm, with a much smoother and cleaner surface. Examination of argon ion thinned samples using ac-STEM would produce the better images of the climbed structures, and better EELS data.

The origin of Band-A emission is a question that has remained unanswered for decades but has been attributed to donor-acceptor recombination, or sp^2 carbon in dislocations and grain-boundaries. The CL imaging and spectroscopy in chapter 5 suggest that differences in the atomic structure of straight and curved dislocations may be a possible origin for the Band A emission, while CL imaging in chapter 4 instead shows that the dislocations are non-radiative recombination centres, with emission originating from an atmosphere around the dislocations. Correlating the CL emission with diffraction contrast TEM imaging may assist in narrowing down the possible origin. Time-resolved CL and PL spectroscopy are other techniques that should be considered in the study of Band A emission. The Band A peak is broad and it is possible that it is made up of many components that emit on different time scales. With more information about the emission, computational modelling could be used to investigate possible defects that produce the band A emission.

On larger length scales the HPHT treatment does not appear to change the dislocation microstructures observed, however changes occurring on smaller length scales have not been examined in detail. As the temperature increases, so does the critical annihilation height of dipoles; dipoles of larger height remain in the crystal while smaller dipoles annihilate. Further ac-STEM imaging of the dipoles both before and after HPHT treatment will help to elucidate changes to the atomic structure of these extended defects. What happens to the vacancies/ vacancy clusters during HPHT treatment is also not answered by the work presented here. From PAS, the vacancy clusters are broken up by the treatment but where those excess vacancies emitted go is unclear. Chapter 5 showed the benefits of using correlative microscopy to examine both the dislocations and point defects in the sample. Further investigation of more plastically deformed samples, including type I diamond, and using other techniques such as FTIR and EPR may assist in answering this question. Not all defects emit in PL or CL[25], so a wider range of techniques may need to be used to "illuminate" these invisible defects. For example, the A and B centres are not visible in PL or CL spectroscopy, but are visible in FTIR spectroscopy. Information provided by defects that were invisible to the techniques used here would provide a more complete picture on the distribution and migration of point defects, and the effects of HPHT treatment.

Bibliography

[1] A.J. Gwinnett and L. Gorelick. Bead Manufacture at Hajar Ar-Rayhani, Yemen. *The Biblical Archaeologist*, 54(4):187–196, 1991. ISSN 0006-0895. doi: 10.2307/3210280.

[2] A.J. Gwinnett and L. Gorelick. Beads, Scarabs, and Amulets: Methods of Manufacture in Ancient Egypt. *Journal of the American Research Center in Egypt*, 30:125, 1993. ISSN 00659991. doi: 10.2307/40000232.

[3] J.M. Kenoyer and M. Vidale. A New Look at Stone Drills of the Indus Valley Tradition. *MRS Proceedings*, 267(Figure 2):495–518, 1992. ISSN 0272-9172. doi: 10.1557/proc-267-495.

[4] M.N. Dutt. *The Garuda Purana*. ALPHA ED, 1908. ISBN 9788183150736.

[5] J. Ogden. *Diamonds: An Early History of the King of Gems*. Yale University Press, 2018. ISBN 9780300215663.

[6] GIA. 4Cs of Diamond Quality, 2020. URL `https://4cs.gia.edu/en-us/4cs-diamond-quality/`.

[7] 'Largest ever auctioned' purple-pink diamond sells for $26.6m (£20.1m), 2020. URL `https://www.bbc.co.uk/news/world-europe-54901982`.

[8] Flawless 102-carat diamond a 'bargain' at $16m, 2020. URL `https://www.bbc.co.uk/news/world-asia-54424327`.

[9] S. Eaton-Magaña, C.M. Breeding, and J.E. Shigley. Natural-Color Blue, Gray, and Violet Diamonds: Allure of the Deep. *Gems & Gemology*, 54(2):112–131, 2018.

[10] S. Eaton-Magaña, T Ardon, K.V. Smit, C.M. Breeding, and J.E. Shigley. Natural-Color Pink, Purple, Red, and Brown Diamonds: Band of Many Colors. *Gems and Gemology*, 54(4):352–377, 2017. ISSN 0016626X.

[11] R.M. Mineeva, S.V. Titkov, and A.V. Speransky. Structural defects in natural plastically deformed diamonds: Evidence from EPR spectroscopy. *Geology of Ore Deposits*, 51(3):233–242, 2009. ISSN 15556476. doi: 10.1134/S1075701509030052.

[12] B. Deljanin, D. Simic, A.M. Zaitsev, J. Chapman, I. Dobrinets, A. Widemann, N. Del Re, T. Middleton, E. Deljanin, and A. De Stefano. Characterization of pink diamonds of different origin: Natural (Argyle, non-Argyle), irradiated and annealed, treated with multi-process, coated and synthetic. *Diamond and Related Materials*, 17(7-10):1169–1178, 2008. ISSN 09259635. doi: 10.1016/j.diamond.2008.03.014.

[13] J.E. Shigley and E. Fritsch. A notable red-brown diamond. *Journal of Gemmology*, 23(5):259 – 266, 1993.

[14] E. Gaillou, J.E. Post, N.D. Bassim, A.M. Zaitsev, T. Rose, M.D. Fries, R.M. Stroud, A. Steele, and J.E. Butler. Spectroscopic and microscopic characterizations of color lamellae in natural pink diamonds. *Diamond and Related Materials*, 19(10):1207–1220, 2010. ISSN 09259635. doi: 10.1016/j.diamond.2010.06.015. URL `http://dx.doi.org/10.1016/j.diamond.2010.06.015`.

[15] W. Saslow, T.K. Bergstresser, and M.L. Cohen. Band structure and optical properties of diamond. *Physical Review Letters*, 16(9):354–356, 1966. ISSN 00319007. doi: 10.1103/PhysRevLett.16.354.

[16] C.J.H. Wort and R.S. Balmer. Diamond as an electronic material. *Materials Today*, 11(1-2):22–28, 2008. ISSN 1369-7021. doi: 10.1016/S1369-7021(07)70349-8. URL `http://dx.doi.org/10.1016/S1369-7021(07)70349-8`.

[17] C.M. Breeding, S. Eaton-Magaña, and J.E. Shigley. Natural-Color Green Diamonds: A Beautiful Conundrum. *Gems & Gemology*, 54(1):2–27, 2018.

[18] B. Willems. *Structural Defects and Colour-Treated Diamond: A Transmission Electron Microscopy Study*. PhD thesis, Antwerp, 2006.

[19] R.G. Farrer. On the substitutional nitrogen donor in diamond. *Solid State Communications*, 7(9):685–688, 1969. ISSN 00381098. doi: 10.1016/0038-1098(69)90593-6.

[20] T. Hainschwang, E. Fritsch, F. Notari, B. Rondeau, and A. Katrusha. The origin of color in natural C center bearing diamonds. *Diamond and Related*

Materials, 39:27–40, 2013. ISSN 09259635. doi: 10.1016/j.diamond.2013.07.007. URL http://dx.doi.org/10.1016/j.diamond.2013.07.007.

[21] C.M. Breeding, S. Eaton-Magaña, and J.E Shigley. Naturally Colored Yellow and Orange Gem Diamonds: The Nitrogen Factor. *Gems & Gemology*, Summer:194–219, 2020.

[22] T.W. Overton and J.E. Shigley. A History of Diamond Treatments. *Gems & Gemology*, 44(1):32 – 35, 2008. doi: 10.1057/9781137537614_9.

[23] J.V. Macpherson. A practical guide to using boron doped diamond in electrochemical research. *Physical chemistry chemical physics : PCCP*, 17(5): 2935–2949, 2015. doi: 10.1039/c4cp04022h.

[24] W. Wang, C.P. Smith, M.S. Hall, C.M. Breeding, and T.M. Moses. Treated-color pink-to-red diamonds from Lucent Diamonds Inc. *Gems & Gemology*, 41(1):6–19, 2005.

[25] A.M. Zaitsev. *Optical Properties of Diamond A Data Handbook*. Springer-Verlag Berlin Heidelberg, 1st edition, 2001. ISBN 978-3-642-08585-7. doi: https://doi.org/10.1007/978-3-662-04548-0.

[26] D. Fisher. Brown diamonds and high pressure high temperature treatment. *Lithos*, 112:619–624, 2009. ISSN 00244937. doi: 10.1016/j.lithos.2009.03.005. URL http://dx.doi.org/10.1016/j.lithos.2009.03.005.

[27] C.P. Smith, G. Bosshart, J. Ponahlo, V.M.F. Hammer, H. Klapper, and K. Schmetzer. GE POL Diamonds: Before and After. *Gems & Gemology*, 3:192–215, 2000.

[28] L.S. Hounsome, R. Jones, P.M. Martineau, D. Fisher, M.J. Shaw, P.R. Briddon, and S. Öberg. Origin of brown coloration in diamond. *Physical Review B - Condensed Matter and Materials Physics*, 73(12):1–8, 2006. ISSN 10980121. doi: 10.1103/PhysRevB.73.125203.

[29] R. Jones. Dislocations, vacancies and the brown colour of CVD and natural diamond. *Diamond and Related Materials*, 18(5-8):820–826, 2009. ISSN 09259635. doi: 10.1016/j.diamond.2008.11.027. URL http://dx.doi.org/10.1016/j.diamond.2008.11.027.

[30] V. Avalos and S. Dannefaer. Vacancy-type defects in brown diamonds investigated by positron annihilation. *Physica B: Condensed Matter*, 340-342:76–79, 2003. ISSN 09214526. doi: 10.1016/j.physb.2003.09.006.

[31] B. Willems, P.M. Martineau, D. Fisher, J. Van Royen, and G. Van Tendeloo. Dislocation distributions in brown diamond. *Physica Status Solidi (A) Applications and Materials Science*, 203(12):3076–3080, 2006. ISSN 18626300. doi: 10.1002/pssa.200671129.

[32] I.S. Godfrey. *What Causes the Colour of Diamonds ?* PhD thesis, University of Manchester, 2013.

[33] U. Bangert, A.J. Harvey, R. Jones, C.J. Fall, A.T. Blumenau, R. Briddon, M. Schreck, and F. Hörmann. Dislocation-induced electronic states and point-defect atmospheres evidenced by electron energy loss imaging. *New Journal of Physics*, 6:1–10, 2004. ISSN 13672630. doi: 10.1088/1367-2630/6/1/184.

[34] J.M. Mäki, F. Tuomisto, C.J. Kelly, D. Fisher, and P.M. Martineau. Properties of optically active vacancy clusters in type IIa diamond. *Journal of Physics Condensed Matter*, 21(36), 2009. ISSN 09538984. doi: 10.1088/0953-8984/21/36/364216.

[35] J.M. Mäki, F. Tuomisto, A. Varpula, D. Fisher, R.U.A. Khan, and P.M. Martineau. Time dependence of charge transfer processes in diamond studied with positrons. *Physical Review Letters*, 107(21), 2011. ISSN 00319007. doi: 10.1103/PhysRevLett.107.217403.

[36] J. M. Mäki, T. Kuittinen, E. Korhonen, and F. Tuomisto. Positron lifetime spectroscopy with optical excitation: A case study of natural diamond. *New Journal of Physics*, 14, 2012. ISSN 13672630. doi: 10.1088/1367-2630/14/3/035023.

[37] R. Barnes, U. Bangert, P. Martineau, D. Fisher, R. Jones, and L.S. Hounsome. Combined TEM and STEM study of the brown colouration of natural diamonds. *Journal of Physics: Conference Series*, 26(1):157–160, 2006. ISSN 17426596. doi: 10.1088/1742-6596/26/1/037.

[38] D. Fisher, D.J.F. Evans, C. Glover, C. J. Kelly, M.J. Sheehy, and G.C. Summerton. The vacancy as a probe of the strain in type IIa diamonds. *Diamond and Related Materials*, 15(10):1636–1642, 2006. ISSN 09259635. doi: 10.1016/j.diamond.2006.01.020.

[39] C.J. Fall, A.T. Blumenau, R. Jones, P.R. Briddon, T. Frauenheim, A. Gutiérrez-Sosa, U. Bangert, A. E. Mora, J.W. Steeds, and J.E. Butler. Dislocations in diamond: Electron energy-loss spectroscopy. *Physical Review*

B - Condensed Matter and Materials Physics, 65(20):2052061–2052067, 2002. ISSN 01631829. doi: 10.1103/PhysRevB.65.205206.

[40] N. Fujita, R. Jones, S. Öberg, and P.R. Briddon. Large spherical vacancy clusters in diamond - Origin of the brown colouration? *Diamond and Related Materials*, 18(5-8):843–845, 2009. ISSN 09259635. doi: 10.1016/j.diamond.2008.10.061. URL `http://dx.doi.org/10.1016/j.diamond.2008.10.061`.

[41] U. Bangert, R. Barnes, M.H. Gass, A.L. Bleloch, and I.S. Godfrey. Vacancy clusters, dislocations and brown colouration in diamond. *Journal of Physics Condensed Matter*, 21(36), 2009. ISSN 09538984. doi: 10.1088/0953-8984/21/36/364208.

[42] I.S. Godfrey and U. Bangert. Atomic structure-colour relationship in natural diamonds. *Journal of Physics: Conference Series*, 241, 2010. ISSN 17426596. doi: 10.1088/1742-6596/241/1/012053.

[43] I.S. Godfrey and U. Bangert. An analysis of vacancy clusters and sp^2 bonding in natural type IIa diamond using aberration corrected STEM and EELS. *Journal of Physics: Conference Series*, 281(1), 2011. ISSN 17426588. doi: 10.1088/1742-6596/281/1/012024.

[44] I.S. Godfrey and U. Bangert. A study of the relationship between brown colour and extended defects in diamond using core-loss electron energy loss spectroscopy. *Journal of Physics: Conference Series*, 371, 2012. ISSN 17426596. doi: 10.1088/1742-6596/371/1/012016.

[45] K.S. Byrne, J.D. Anstie, J.G. Chapman, and A.N. Luiten. Optically reversible photochromism in natural pink diamond. *Diamond and Related Materials*, 30:31–36, 2012. ISSN 09259635. doi: 10.1016/j.diamond.2012.09.005. URL `http://dx.doi.org/10.1016/j.diamond.2012.09.005`.

[46] K.S. Byrne, J.D. Anstie, J. Chapman, and A.N. Luiten. Infrared microspectroscopy of natural Argyle pink diamond. *Diamond and Related Materials*, 23:125–129, 2012. ISSN 09259635. doi: 10.1016/j.diamond.2012.01.032. URL `http://dx.doi.org/10.1016/j.diamond.2012.01.032`.

[47] K.S. Byrne, J.G. Chapman, and A.N. Luiten. Erratum: Photochromic charge transfer processes in natural pink and brown diamonds (Journal of Physics Condensed Matter (2014) 26 (035501)). *Journal of Physics Condensed Matter*, 26(23), 2014. ISSN 1361648X. doi: 10.1088/0953-8984/26/23/239502.

[48] D. Fisher, S.J. Sibley, and C.J. Kelly. Brown colour in natural diamond and interaction between the brown related and other colour-inducing defects. *Journal of Physics Condensed Matter*, 21(36), 2009. ISSN 09538984. doi: 10.1088/0953-8984/21/36/364213.

[49] G.P. Bulanova. The formation of diamond. *Journal of Geochemical Exploration*, 53:1–23, 1995.

[50] T. Stachel and J.W. Harris. The origin of cratonic diamonds - Constraints from mineral inclusions. *Ore Geology Reviews*, 34(1-2):5–32, 2008. ISSN 01691368. doi: 10.1016/j.oregeorev.2007.05.002.

[51] P. Cartigny. Stable Isotopes and the Origin of Diamond. *Elements*, 1:79–84, 2005.

[52] R.S.J. Sparks, L. Baker, R.J. Brown, M. Field, J. Schumacher, G. Stripp, and A. Walters. Dynamical constraints on kimberlite volcanism. *Journal of Volcanology and Geothermal Research*, 155(1-2):18–48, 2006. ISSN 03770273. doi: 10.1016/j.jvolgeores.2006.02.010.

[53] M.V. Patterson and D. Francis. Kimberlite eruptions as triggers for early Cenozoic hyperthermals. *Geochemistry, Geophysics, Geosystems*, 14(2):448–456, 2013. ISSN 15252027. doi: 10.1002/ggge.20054.

[54] L. Wilson and J.W. Head. An integrated model of kimberlite ascent and eruption. *Nature*, 447(7140):53–57, 2007. ISSN 14764687. doi: 10.1038/nature05692.

[55] A.T. Collins, H. Kanda, and H. Kitawaki. Colour changes produced in natural brown diamonds by high-pressure, high-temperature treatment. *Diamond and Related Materials*, 9(2):113–122, 2000. ISSN 09259635. doi: 10.1016/S0925-9635(00)00249-1. URL `http://linkinghub.elsevier.com/retrieve/pii/S0925963500002491`.

[56] E.M. Smith, H.H. Helmstaedt, and R.L. Flemming. Survival of the brown color in diamond during storage in the subcontinental lithospheric mantle. *Canadian Mineralogist*, 48(3):571–582, 2010. ISSN 00084476. doi: 10.3749/canmin.48.3.571.

[57] R.C. DeVries. Plastic deformation and "work-hardening" of diamond. *Materials Research Bulletin*, 10(11):1193–1199, 1975. ISSN 00255408. doi: 10.1016/0025-5408(75)90026-4.

[58] E.J. Brookes, P. Greenwood, and G. Xing. The plastic deformation and strain-induced fracture of natural and synthetic diamond. *Diamond and Related Materials*, 8(8-9):1536–1539, 1999. ISSN 09259635.

[59] P. Humble and R.H.J. Hannink. Plastic deformation of diamond at room temperature. *Nature*, 273(5657):37–39, 1978. ISSN 00280836. doi: 10.1038/273037a0.

[60] T. Evans and R.K. Wild. Plastic bending of diamond plates. *Philosophical Magazine*, 12(117):479–489, 1965. ISSN 00318086. doi: 10.1080/14786436508218894.

[61] J.P. Goss, B.J. Coomer, R. Jones, C.J. Fall, P.R. Briddon, and S. Öberg. Extended defects in diamond: The interstitial platelet. *Physical Review B - Condensed Matter and Materials Physics*, 67(16):1–15, 2003. ISSN 1550235X. doi: 10.1103/PhysRevB.67.165208.

[62] E.J. Olivier, J.H. Neethling, R.E. Kroon, S.R. Naidoo, C.S. Allen, H. Sawada, P.A. van Aken, and A.I. Kirkland. Imaging the atomic structure and local chemistry of platelets in natural type Ia diamond. *Nature Materials*, 17(3):243–248, 2018. ISSN 1476-1122. doi: 10.1038/s41563-018-0024-6. URL `http://www.nature.com/articles/s41563-018-0024-6`.

[63] D. Howell, S. Piazolo, D.P. Dobson, I.G. Wood, A.P. Jones, N. Walte, D.J. Frost, D. Fisher, and W.L. Griffin. Quantitative characterization of plastic deformation of single diamond crystals: A high pressure high temperature (HPHT) experimental deformation study combined with electron backscatter diffraction (EBSD). *Diamond and Related Materials*, 30:20–30, 2012. ISSN 09259635. doi: 10.1016/j.diamond.2012.09.003.

[64] C. Breeding and J.E. Shigley. The "type" classification system of diamonds and its importance in gemology. *Gems and Gemology*, 45(2):96–111, 2009. ISSN 0016626X. doi: 10.5741/GEMS.45.2.96.

[65] T. Hainschwang, F. Notari, E. Fritsch, and L. Massi. Natural, untreated diamonds showing the A, B and C infrared absorptions ("ABC diamonds"), and the H2 absorption. *Diamond and Related Materials*, 15(10):1555–1564, 2006. ISSN 09259635. doi: 10.1016/j.diamond.2005.12.029.

[66] J.P. Hirth and J. Loethe. *Theory of Dislocations*. Krieger Publishing Company, Malabar, Florida 32950, 2nd edition, 1982.

[67] M.W. Dale. *Colour centres on demand in diamond*. PhD thesis, University of Warwick, 2015. URL `http://wrap.warwick.ac.uk/80044/`.

[68] C.D. Clark and J. Walker. The neutral vacancy in diamond. *Proceedings of the Royal Society of London. A. Mathematical and Physical Sciences*, 334: 241–257, 1973. ISSN 2053-9169. doi: 10.1098/rspa.1973.0090.

[69] J.P. Goss, R. Jones, and P.R. Briddon. Stress tensors and dilatation of interstitial defects in diamond. *Physical Review B*, 65 (035203):1–8, 2001. ISSN 1550235X. doi: 10.1103/PhysRevB.65.035203. URL `https://0-journals-aps-org.pugwash.lib.warwick.ac.uk/prb/pdf/10.1103/PhysRevB.65.035203`.

[70] B. Slepetz and M. Kertesz. Divacancies in diamond: A stepwise formation mechanism. *Physical Chemistry Chemical Physics*, 16(4):1515–1521, 2014. ISSN 14639076. doi: 10.1039/c3cp53384k.

[71] M.I.J. Probert and M.C. Payne. Improving the convergence of defect calculations in supercells: An ab initio study of the neutral silicon vacancy. *Physical Review B - Condensed Matter and Materials Physics*, 67(7):1–11, 2003. ISSN 1550235X. doi: 10.1103/PhysRevB.67.075204.

[72] J. Lento and R.M. Nieminen. Non-local screened-exchange calculations for defects in semiconductors: Vacancy in silicon. *Journal of Physics Condensed Matter*, 15(25):4387–4395, 2003. ISSN 09538984. doi: 10.1088/0953-8984/15/25/309.

[73] J. Bernholc, A. Antonelli, T.M. Del Sole, Y. Bar-Yam, and S.T. Pantelides. Mechanism of self-diffusion in diamond. *Physical Review Letters*, 61(23):2689–2692, 1988. ISSN 00319007. doi: 10.1103/PhysRevLett.61.2689.

[74] S. Lawson, G. Davies, A.T. Collins, and A. Mainwood. Migration energy of the neutral vacancy in diamond. *Journal of Physics: Condensed Matter*, 4(9), 1992. ISSN 09538984. doi: 10.1088/0953-8984/4/9/001.

[75] G. Davies. Charge states of the vacancy in diamond. *Nature*, 269:498–500, 1977.

[76] P.L. Diggle. *Single point defect imaging studies in diamond*. PhD thesis, University of Warwick, 2019.

[77] G. Davies, S.C. Lawson, A.T. Collins, A. Mainwood, and S.J. Sharp. Vacancy-related centers in diamond. *Physical Review B*, 46(20):13157–13170, 1992. ISSN 01631829. doi: 10.1103/PhysRevB.46.13157.

[78] J.P. Goss, B.J. Coomer, T.D. Shaw, P.R. Briddon, M. Rayson, and S. Öberg. Self-interstitial aggregation in diamond. *Physical Review B - Condensed Matter and Materials Physics*, 63(19), 2001. ISSN 1550235X. doi: 10.1103/PhysRevB.63.195208.

[79] D.C. Hunt, D.J. Twitchen, M.E. Newton, and J.M. Baker. Identification of the neutral carbon < 100> -split interstitial in diamond. *Physical Review B*, 61(6):3863–3876, 2000.

[80] H.L. Li and E.J. Lowther. Plane-wave pseudopotential calculations defects in diamond. *Journal of Physical Chemistry Solids*, 58(10):1607–1610, 1997.

[81] M.E. Newton, B.A. Campbell, D.J. Twitchen, J.M. Baker, and T.R. Anthony. Recombination-enhanced diffusion of self-interstitial atoms and vacancy-interstitial recombination in diamond. *Diamond and Related Materials*, 11 (3-6):618–622, 2002. ISSN 09259635. doi: 10.1016/S0925-9635(01)00623-9.

[82] A. Mainwood. Nitrogen and nitrogen-vacancy complexes and their formation in diamond. 49(12):7934–7941, 1994.

[83] T. Evans and Z. Qi. The kinetics of the aggregation of nitrogen atoms in diamond. *Proc R Soc London Ser A*, 381:159–178, 1982.

[84] S.C. Lawson, G. Davies, A.T. Collins, and A. Mainwood. The 'H2' optical transition in diamond: The effects of uniaxial stress perturbations, temperature and isotopic substitution. *Journal of Physics: Condensed Matter*, 4(13): 3439–3452, 1992. ISSN 09538984. doi: 10.1088/0953-8984/4/13/008.

[85] A.T. Collins and G.S. Woods. Cathodoluminescence from "giant" platelets, and of the 2.526 eV vibronic system, in type Ia diamonds. *Philosophical Magazine B: Physics of Condensed Matter; Statistical Mechanics, Electronic, Optical and Magnetic Properties*, 45(4):385–397, 1982. doi: 10.1080/01418638208227446.

[86] P.L. Hanley, I. Kiflawi, and A.R. Lang. On topographically identifiable sources of cathodoluminescence in natural diamonds. *Philosophical Transactions of the Royal Society of London. Series A, Mathemathical and Physical Sciences*, 284 (1324):329–368, 1977.

[87] S.T. Davey, T. Evans, and S.H. Robertson. An investigation of plastic deformation in sintered diamond compacts using photoluminescence spectroscopy. *Journal of Materials Science Letters*, 3(12):1090–1092, 1984. ISSN 02618028. doi: 10.1007/BF00719773.

[88] R.J. Graham and P.R. Buseck. Cathodoluminescence of brown diamonds as observed by transmission electron microscopy. *Philosophical Magazine B: Physics of Condensed Matter; Statistical Mechanics, Electronic, Optical and Magnetic Properties*, 70(6):1177–1185, 1994. ISSN 13642812. doi: 10.1080/01418639408240282.

[89] H. Kanda and K. Watanabe. Distribution of the cobalt-related luminescence center in HPHT diamond. *Diamond and Related Materials*, 6(5-7):708–711, 1997. ISSN 09259635. doi: 10.1016/s0925-9635(96)00666-8.

[90] M.N.R. Ashfold, J.P. Goss, B.L. Green, P.W. May, M.E. Newton, and C.V. Peaker. Nitrogen in Diamond. *Chemical Reviews*, 120:5745 – 5794, 2020. doi: 10.1021/acs.chemrev.9b00518.

[91] I. Kiflawi and J. Bruley. The nitrogen aggregation sequence and the formation of voidites in diamond. *Diamond and Related Materials*, 9(1):87–93, 2000. ISSN 09259635. doi: 10.1016/S0925-9635(99)00265-4.

[92] G.S. Woods. Platelets and the infrared absorption of type Ia diamonds. *Proceedings of the Physical Society. Section A*, 407:219–238, 1986.

[93] L. Speich, S.C. Kohn, G.P. Bulanova, and C.B. Smith. The behaviour of platelets in natural diamonds and the development of a new mantle thermometer. *Contributions to Mineralogy and Petrology*, 173(5):1–21, 2018. ISSN 00107999. doi: 10.1007/s00410-018-1463-4. URL `http://dx.doi.org/10.1007/s00410-018-1463-4`.

[94] P. Humble. The structure and mechanism of formation of platelets in natural type Ia diamond. *Proceedings of the Royal Society of London. A. Mathematical and Physical Sciences*, 381:65–81, 1982. ISSN 2053-9169. doi: 10.1098/rspa.1982.0059.

[95] J.M. Cowley, M.A. Osman, and P. Humble. Nanodiffraction from platelet defects in diamond. *Ultramicroscopy*, 15:311–318, 1984.

[96] A.T. Blumenau, T.A.G. Eberlein, R. Jones, and T. Frauenheim. The Modelling of Dislocations in Semiconductor Crystals. *Euromat 2005*, 2002.

[97] P. Pirouz, D.J.H. Cockayne, N. Sumida, P. Hirsch, and A.R. Lang. Dissociation of dislocations in diamond. *Proceedings of the Royal Society of London. A. Mathematical and Physical Sciences*, 386(1791):241 LP – 249, apr 1983.

[98] J.P. Hirth. On dislocation interactions in the fcc lattice. *Journal of Applied Physics*, 32(4):700–706, 1961. ISSN 00218979. doi: 10.1063/1.1736074.

[99] A. Nanakoudis. SEM: Types of Electrons and the Information They Provide. URL `https://www.thermofisher.com/blog/microscopy/sem-types-electrons-and-the-information-they-provide/`.

[100] J.I. Goldstein, D.E. Newbury, J.R. Michael, N.W.M. Ritchie, J.H.J. Scott, and D.C. Joy. *Scanning Electron Microscopy and X-Ray Microanalysis*. 2018. ISBN 9781493966745. doi: 10.1007/978-1-4939-6676-9.

[101] D.B. Williams and C.B. Carter. *Transmission Electron Microscopy A Textbook for Materials Science*. 2nd editio edition, 1996. ISBN 978-0-387-76500-6. doi: https://doi.org/10.1007/978-0-387-76501-3.

[102] S. Vespucci, A. Winkelmann, G. Naresh-Kumar, K.P. Mingard, D. Maneuski, P.R. Edwards, A.P. Day, V. O'Shea, and C. Trager-Cowan. Digital direct electron imaging of energy-filtered electron backscatter diffraction patterns. *Physical Review B - Condensed Matter and Materials Physics*, 92(20):8–14, 2015. ISSN 1550235X. doi: 10.1103/PhysRevB.92.205301.

[103] A.J. Schwartz, M. Kumar, B.L. Adams, and D.P. Field. *Electron Backscatter Diffraction in Materials Science*, volume 86. Springer, Boston, 2nd editio edition, 2000. ISBN 978-0-387-88135-5. doi: 10.1017/CBO9781107415324.004. URL `https://doi.org/10.1007/978-0-387-88136-2`.

[104] T. Coenen and N.M. Haegel. Cathodoluminescence for the 21st century: Learning more from light. *Applied Physics Reviews*, 4(3), 2017. ISSN 19319401. doi: 10.1063/1.4985767.

[105] B.G. Yacobi and D.B. Holt. Cathodoluminescence scanning electron microscopy of semiconductor. *Applied Physics Letters*, 59(4):R1–R24, 1986.

[106] Z. Mahfoud, A.T. Dijksman, C. Javaux, P. Bassoul, A.L. Baudrion, J. Plain, B. Dubertret, and M. Kociak. Cathodoluminescence in a scanning transmission electron microscope: A nanometer-scale counterpart of photoluminescence for the study of II-VI quantum dots. *Journal of Physical Chemistry Letters*, 4(23):4090–4094, 2013. ISSN 19487185. doi: 10.1021/jz402233x.

[107] V.I. Petrov and R.S. Gvozdover. Spatial resolution of cathodoluminescence scanning electron microscopy of semiconductors. *Scanning*, 13(6):410–414, 1991. ISSN 19328745. doi: 10.1002/sca.4950130605.

[108] P. Hovington, D. Drouin, R. Gauvin, D.C. Joy, and N. Evans. CASINO: A new Monte Carlo code in C language for electron beam interactions - Part III: Stopping power at low energies. *Scanning*, 19(1):29–35, 1997. ISSN 01610457. doi: 10.1002/sca.4950190104.

[109] D. Drouin, A.R. Couture, D. Joly, X. Tastet, V. Aimez, and R. Gauvin. CASINO V2.42 - A fast and easy-to-use modeling tool for scanning electron microscopy and microanalysis users. *Scanning*, 29(3):92–101, 2007. ISSN 01610457. doi: 10.1002/sca.20000.

[110] K. Fleischer, M. Toth, M.R. Phillips, J. Zou, G. Li, and S.J. Chua. Depth profiling of GaN by cathodoluminescence microanalysis. *Applied Physics Letters*, 74(8):1114–1116, 1999. ISSN 00036951. doi: 10.1063/1.123460.

[111] J.D. Ye, H. Zhao, W. Liu, S.L. Gu, R. Zhang, Y.D. Zheng, S.T. Tan, X.W. Sun, G. Q. Lo, and K. L. Teo. Theoretical and experimental depth-resolved cathodoluminescence microanalysis of excitonic emission from ZnO epilayers. *Applied Physics Letters*, 92(13), 2008. ISSN 00036951. doi: 10.1063/1.2907249.

[112] M. Toth, C. Zachreson, and I. Aharonovich. Role of recombination pathway competition in spatially resolved cathodoluminescence spectroscopy. *Applied Physics Letters*, 105(24), 2014. ISSN 00036951. doi: 10.1063/1.4904809. URL `http://dx.doi.org/10.1063/1.4904809`.

[113] J. Yuan, S.D. Berger, and L.M. Brown. Thickness dependence of cathodoluminescence in thin films. *Journal of Physics: Condensed Matter*, 1(20): 3253–3265, 1989. ISSN 09538984. doi: 10.1088/0953-8984/1/20/006.

[114] G.D. Gilliland. *Photoluminescence spectroscopy of crystalline semiconductors*, volume 18. 1997. ISBN 0000000000. doi: 10.1016/s0927-796x(97)80003-4.

[115] S.C. Eaton-Magaña and K.S. Moe. Temperature effects on radiation stains in natural diamonds. *Diamond and Related Materials*, 64:130–142, 2016. ISSN 09259635. doi: 10.1016/j.diamond.2016.02.009. URL `http://dx.doi.org/10.1016/j.diamond.2016.02.009`.

[116] J. Jimenez and J.W. Tomm. *Spectroscopic Analysis of Optoelectronic Semiconductors*, volume 202. 2016. ISBN 978-3-319-42349-4. URL http://link.springer.com/10.1007/978-3-319-42349-4.

[117] Lothar Schermelleh, Alexia Ferrand, Thomas Huser, Christian Eggeling, Markus Sauer, Oliver Biehlmaier, and Gregor P.C. Drummen. Super-resolution microscopy demystified. *Nature Cell Biology*, 21(1):72–84, 2019. ISSN 14764679. doi: 10.1038/s41556-018-0251-8. URL http://dx.doi.org/10.1038/s41556-018-0251-8.

[118] R.F. Egerton. *Electron Energy Loss Spectroscopy in the Electron Microscope*. Springer, 3rd edition, 2011. ISBN 978-1-4419-9582-7. doi: 10.1007/978-1-4419-9583-4.

[119] Gatan. Gatan Image Filter (GIF). URL https://eels.info/products/gatan-imaging-filter-gif.

[120] F.S. Hage, D.M. Kepaptsoglou, Q.M. Ramasse, and L.J. Allen. Phonon Spectroscopy at Atomic Resolution. *Physical Review Letters*, 122(1):16103, 2019. ISSN 10797114. doi: 10.1103/PhysRevLett.122.016103. URL https://doi.org/10.1103/PhysRevLett.122.016103.

[121] O.L. Krivanek, T.C. Lovejoy, N. Dellby, T. Aoki, R.W. Carpenter, P. Rez, E. Soignard, J. Zhu, P.E. Batson, M.J. Lagos, R.F. Egerton, and P.A. Crozier. Vibrational spectroscopy in the electron microscope. *Nature*, 514(7521):209–212, 2014. ISSN 14764687. doi: 10.1038/nature13870.

[122] Y. Sato, M. Bugnet, M. Terauchi, G.A. Botton, and A. Yoshiasa. Heterogeneous diamond phases in compressed graphite studied by electron energy-loss spectroscopy. *Diamond and Related Materials*, 64:190–196, 2016. ISSN 09259635. doi: 10.1016/j.diamond.2016.02.010. URL http://dx.doi.org/10.1016/j.diamond.2016.02.010.

[123] K. Wang, J.W. Steeds, Z. Li, and H. Wang. Annealing and lateral migration of defects in IIa diamond created by near-threshold electron irradiation. *Applied Physics Letters*, 110(15), 2017. ISSN 00036951. doi: 10.1063/1.4980017. URL http://dx.doi.org/10.1063/1.4980017.

[124] F. Seitz. On the generation of vacancies by moving dislocations. *Advances in Physics*, 1(1):43–90, 1952. ISSN 14606976. doi: 10.1080/00018735200101161.

[125] A. Seeger. CXXXII. The generation of lattice defects by moving dislocations, and its application to the temperature dependence of the flow-stress of F.C.C. crystals. *The London, Edinburgh, and Dublin Philosophical Magazine and Journal of Science*, 46(382):1194–1217, 1955. ISSN 1941-5982. doi: 10.1080/14786441108520632.

[126] S. Amelinckx. *Dislocations in Solids Vol. 2 Chapter 6 (edited by F.R.N Nabarro)*. North-Holland Publishing Co., Amsterdam, 1979.

[127] L.M. Brown. Constant intermittent flow of dislocations: Central problems in plasticity. *Materials Science and Technology (United Kingdom)*, 28(11): 1209–1232, 2012. ISSN 02670836. doi: 10.1179/174328412X13409726212768.

[128] M. Niewczas. Intermittent plastic flow of single crystals: Central problems in plasticity: A review. *Materials Science and Technology (United Kingdom)*, 30 (7):739–757, 2014. ISSN 17432847. doi: 10.1179/1743284713Y.0000000492.

[129] C. Dauwe, M. Dorikens, L. Dorikens-Vanpraet, and D. Segers. Positron Lifetimes and Lineshape Factors in Deformed Copper. *Applied Physics*, 5:117–120, 1974. ISSN 00218979. doi: 10.1063/1.1710271.

[130] Alfred. Seeger. Hyperfine interaction evidence for the existence of two distinct types of self-interstitials in face-centred cubic metals. *Physics Letters A*, 89 (5):241–244, 1982. ISSN 03759601. doi: 10.1016/0375-9601(82)90890-8.

[131] C.B. Carter. The formation and properties of faulted dipoles. *Philosophical Magazine*, 36(1):147–167, 1977. ISSN 00318086. doi: 10.1080/00318087708244454.

[132] J. Hornstra. On the type of point defects formed after crossing of dislocations. *Acta Metallurgica*, 10:987 – 988, 1962. doi: https://doi.org/10.1016/0001-6160(62)90160-8.

[133] M. Niewczas. Transmission electron microscopy observations of debris structure in deformed copper single crystals. *Philosophical Magazine A: Physics of Condensed Matter, Structure, Defects and Mechanical Properties*, 82(2): 393–414, 2002. ISSN 01418610. doi: 10.1080/01418610208239607.

[134] L.M. Brown. A dipole model for the cross-slip of screw dislocations in fee metals. *Philosophical Magazine A: Physics of Condensed Matter, Structure, Defects and Mechanical Properties*, 82(9):1691–1711, 2002. ISSN 01418610. doi: 10.1080/01418610208235684.

[135] B.C. De Cooman and C.B. Carter. The Formation of Faulted Dipoles in Plastically Deformed GaAs. *Physica Status Solidi (a)*, 112(1):41–54, 1989. ISSN 1521396X. doi: 10.1002/pssa.2211120105.

[136] D. Takeuchi, H. Watanabe, S. Yamanaka, H. Okushi, H. Sawada, H. Ichinose, T. Sekiguchi, and K. Kajimura. Origin of band-A emission in diamond thin films. *Physical Review B - Condensed Matter and Materials Physics*, 63(24): 1–7, 2001. ISSN 1550235X. doi: 10.1103/PhysRevB.63.245328.

[137] A.T. Collins. Intrinsic and extrinsic absorption and luminescence in diamond. *Physica B: Physics of Condensed Matter*, 185(1-4):284–296, 1993. ISSN 09214526. doi: 10.1016/0921-4526(93)90250-A.

[138] A.M. Sanchez, J.A Gott, H.A. Fonseka, Y. Zhang, H. Liu, and R. Beanland. Stable Defects in Semiconductor Nanowires. *Nano Letters*, page acs.nanolett.8b00620, 2018. ISSN 1530-6984. doi: 10.1021/acs.nanolett.8b00620. URL `http://pubs.acs.org/doi/10.1021/acs.nanolett.8b00620`.

[139] J. Thibault-Desseaux, H.O.K. Kirchner, and J.L. Putaux. Climb of dissociated dislocations in silicon. *Philosophical Magazine A: Physics of Condensed Matter, Structure, Defects and Mechanical Properties*, 60(3):385–400, 1989. ISSN 01418610. doi: 10.1080/01418618908213868.

[140] S. Takeda, M. Kohyama, and K. Ibe. Interstitial defects on (113) in Si and Ge Line defect configuration incorporated with a self-interstitial atom chain. *Philosophical Magazine A: Physics of Condensed Matter, Structure, Defects and Mechanical Properties*, 70(2):287–312, 1994. ISSN 01418610. doi: 10.1080/01418619408243186.

[141] A. Parisini and A. Bourret. Diamond hexagonal silicon phase and (113) defects energy calculations and new defect models. *Philosophical Magazine A: Physics of Condensed Matter, Structure, Defects and Mechanical Properties*, 67(3): 605–625, 1993. ISSN 01418610. doi: 10.1080/01418619308207180.

[142] J.W. Steeds. The formation and configurations of faulted dipoles in F.C.C. metals. *Philosophical Magazine*, 16(142):771–784, 1967. ISSN 00318086. doi: 10.1080/14786436708222776.

[143] S.W. Chiang, C.B. Carter, and D.L. Kohlstedt. Faulted dipoles in germanium A high-resolution transmission electron microscopy study. *Philosophi-*

cal Magazine A: Physics of Condensed Matter, Structure, Defects and Mechanical Properties, 42(1):103–121, 1980. ISSN 01418610. doi: 10.1080/01418618008239358.

[144] B.C. De Cooman and C.B. Carter. Faulted dipoles in GaAs. *Applied Physics Letters*, 50(1):40–42, 1987. ISSN 00036951. doi: 10.1063/1.98120.

[145] C.B. Carter and S.M. Holmes. The study of faulted dipoles in copper using weak-beam electron microscopy. *Philosophical Magazine*, 32(3):599–614, 1975. ISSN 00318086. doi: 10.1080/14786437508220883.

[146] P. Veyssière. The weak-beam technique applied to the analysis of materials properties. *Journal of Materials Science*, 41(9):2691–2702, 2006. ISSN 00222461. doi: 10.1007/s10853-006-7872-1.

[147] M.H. Grimsditch and A.K. Ramdas. Brillouin scattering in diamond. *Physical Review B*, 11(8):3139 – 3148, 1975.

[148] D. Cherns and G. Feuillet. The mechanism of dislocation climb in GaAs under electron irradiation. *Philosophical Magazine A*, 51(5):661–674, 1985. ISSN 0141-8610. doi: 10.1080/01418618508245280. URL `http://www.tandfonline.com/doi/abs/10.1080/01418618508245280`.

[149] B. Décamps, D. Cherns, and M. Condat. The climb of dissociated dislocations in a quenched Cu-13·43 at.% Al alloy. *Philosophical Magazine A: Physics of Condensed Matter, Structure, Defects and Mechanical Properties*, 48(1):123–137, 1983. ISSN 01418610. doi: 10.1080/01418618308234891.

[150] A. Pu, T. Bretagnon, D. Kerr, and S. Dannefaer. Positron annihilation investigation of vacancies in as-grown and electron-irradiated diamonds. *Diamond and Related Materials*, 9(8):1450–1463, 2000. ISSN 09259635. doi: 10.1016/S0925-9635(00)00264-8.

[151] D. Cherns, P.B. Hirsch, and H. Saka. Mechanism of climb of dissociated dislocations. *Proceedings of the Royal Society of London. A. Mathematical and Physical Sciences*, 371:213–234, 1980.

[152] S. Eaton-Magaña. Comparison of luminescence lifetimes from natural and laboratory irradiated diamonds. *Diamond and Related Materials*, 58:94–102, 2015. ISSN 09259635. doi: 10.1016/j.diamond.2015.06.007. URL `http://dx.doi.org/10.1016/j.diamond.2015.06.007`.

[153] J. Koike, D.M. Parkin, and T.E. Mitchell. Displacement threshold energy for type IIa diamond. *Applied Physics Letters*, 60(12):1450–1452, 1992. ISSN 00036951. doi: 10.1063/1.107267.

[154] J. Schwartz, S. Aloni, D.F. Ogletree, and T. Schenkel. Effects of low-energy electron irradiation on formation of nitrogen-vacancy centers in single-crystal diamond. *New Journal of Physics*, 14, 2012. ISSN 13672630. doi: 10.1088/1367-2630/14/4/043024.

[155] C.A. McLellan, B.A. Myers, S. Kraemer, K. Ohno, D.D. Awschalom, and A.C. Bleszynski Jayich. Patterned Formation of Highly Coherent Nitrogen-Vacancy Centers Using a Focused Electron Irradiation Technique. *Nano Letters*, 16(4):2450–2454, 2016. ISSN 15306992. doi: 10.1021/acs.nanolett.5b05304.

[156] P.T. Heald. The preferential trapping of interstitials at dislocations II. The effect of competition between neighbouring dislocations. *Philosophical Magazine*, 34(4):647–652, 1976. ISSN 00318086. doi: 10.1080/14786437608223802.

[157] J.F. Prins, T.E. Derry, and J.P.F. Sellschop. Volume expansion of diamond during ion implantation. *Physical Review B*, 34(12):8870 – 8874, 1986.

[158] F. Häussermann and M. Wilkens. Bestimmung des Stapelfehlerenergiekubisch-flächensentrierter Meatlle aus der Analyse des elektronenemikroskopischen Beugungskontrastes von Stapelfehlerdipolen. *Physica Status Solidi*, 18:609–624, 1966.

[159] E. Wintner and H.P. Karnthaler. The Geometry and Formation of Faulted Dipoles in Cu-Al Alloys. *Acta Metallurgica*, 26:941–949, 1978.

[160] A. Seeger and G. Wobser. Stapelfehlerdipole in kubish-fläschenzentrierten Metallen. *Physica Status Solidi*, 18:189–206, 1966.

[161] Z. Yan and Y. Lin. Faulted dipoles in a nanostructured 7075 Al alloy produced via high-pressure torsion. *Materials Science and Engineering A*, 754 (February):232–237, 2019. ISSN 09215093. doi: 10.1016/j.msea.2019.03.081. URL `https://doi.org/10.1016/j.msea.2019.03.081`.

[162] A.T. Winter, S. Mahajan, and D. Brasen. Weak-beam electron microscopy of faulted dipoles in deformed silicon. *Philosophical Magazine A: Physics of Condensed Matter, Structure, Defects and Mechanical Properties*, 37(3):315–326, 1978. ISSN 01418610. doi: 10.1080/01418617808239170.

[163] J.C.H. Spence and H. Kolar. Lattice imaging of faulted dipoles in silicon. *Philosophical Magazine A: Physics of Condensed Matter, Structure, Defects and Mechanical Properties*, 39(1):59–63, 1979. ISSN 01418610. doi: 10.1080/01418617908239275.

[164] Y. Nishino and T. Imura. Dislocation configurations induced by cyclic deformation in silicon crystals. *Physica Status Solidi (a)*, 78(2):655–663, 1983. ISSN 1521396X. doi: 10.1002/pssa.2210780233.

[165] Y. Nishino, H. Saka, and T. Imura. Dislocation Configurations Characteristic of Deformed Czochralski-Grown Silicon Crystals. *Physica Status Solidi (a)*, 70(729):729–737, 1982.

[166] I. Yonenaga, S.H. Lim, D. Shindo, P.D. Brown, and C. . Humphreys. Structure and climb of faulted dipoles in GaAs. *Physica Status Solidi (A) Applied Research*, 171(1):53–57, 1999. ISSN 00318965. doi: 10.1002/(SICI)1521-396X(199901)171:1⟨53::AID-PSSA53⟩3.0.CO;2-I.

[167] S.H. Lim, D. Shindo, I. Yonenaga, P.D. Brown, and C.J. Humphreys. Atomic arrangement of a Z-shape faulted dipole within deformed GaAs. *Physical Review Letters*, 81(24):5350–5353, 1998. ISSN 10797114. doi: 10.1103/PhysRevLett.81.5350.

[168] A. Mussi, D. Eyidi, A. Shiryaev, and J. Rabier. TEM observations of dislocations in plastically deformed diamond. *Physica Status Solidi (A) Applications and Materials Science*, 210(1):191–194, 2013. ISSN 18626300. doi: 10.1002/pssa.201200483.

[169] S. Eaton-Magaña, G. McElhenny, C.M. Breeding, and T. Ardon. Comparison of gemological and spectroscopic features in type IIa and Ia natural pink diamonds. *Diamond and Related Materials*, 105(October 2019):107784, 2020. ISSN 09259635. doi: 10.1016/j.diamond.2020.107784. URL `https://doi.org/10.1016/j.diamond.2020.107784`.

[170] D. Howell, D. Fisher, S. Piazolo, W.L. Grifin, and S.J. Sibley. Pink color in Type I diamonds : Is deformation twinning the cause? *American Mineralogist*, 100:1518–1527, 2015.

[171] M. Schoor, J.C. Boulliard, E. Gaillou, O. Hardouin Duparc, I. Estève, B. Baptiste, B. Rondeau, and E. Fritsch. Plastic deformation in natural diamonds:

Rose channels associated to mechanical twinning. *Diamond and Related Materials*, 66:102–106, 2016. ISSN 09259635. doi: 10.1016/j.diamond.2016.04.004. URL http://dx.doi.org/10.1016/j.diamond.2016.04.004.

[172] N. Hansen and C.Y. Barlow. *Plastic Deformation of Metals and Alloys*. Elsevier, fifth edit edition, 2014. ISBN 9780444537706. doi: 10.1016/B978-0-444-53770-6.00017-4. URL http://dx.doi.org/10.1016/B978-0-444-53770-6.00017-4.

[173] L. Massi, E. Fritsch, A.T. Collins, T. Hainschwang, and F. Notari. The "amber centres" and their relation to the brown colour in diamond. *Diamond and Related Materials*, 14(10):1623–1629, 2005. ISSN 09259635. doi: 10.1016/j.diamond.2005.05.003.

[174] D. Schiferl, Ma. Nicol, J.M. Zaug, S.K. Sharma, T.F. Cooney, S.Y. Wang, T.R. Anthony, and J.F. Fleischer. The diamond $^{13}C/^{12}C$ isotope Raman pressure sensor system for high-temperature/pressure diamond-anvil cells with reactive samples. *Journal of Applied Physics*, 82(7):3256–3265, 1997. ISSN 00218979. doi: 10.1063/1.366268.

[175] A.D. Brailsford and R. Bullough. The rate theory of swelling due to void growth in irradiated metals. *Journal of Nuclear Materials*, 44(2):121–135, 1972. ISSN 00223115. doi: 10.1016/0022-3115(72)90091-8.

[176] H. Wiedersich. On the theory of void formation during irradiation. *Radiation Effects*, 12(1-2):111–125, 1972. ISSN 0033-7579. doi: 10.1080/00337577208231128.

[177] V.A. Nadolinny, O.P. Yurjeva, and N.P. Pokhilenko. EPR and luminescence data on the nitrogen aggregation in diamonds from Snap Lake dyke system. *Lithos*, 112:865–869, 2009. ISSN 00244937. doi: 10.1016/j.lithos.2009.05.045. URL http://dx.doi.org/10.1016/j.lithos.2009.05.045.

[178] A.T. Collins, A. Connor, C. Ly, A. Shareef, and P.M. Spear. High-temperature annealing of optical centers in type-I diamond. *Journal of Applied Physics*, 97, 2005. doi: 10.1063/1.1866501.

[179] D. Fisher and R.A. Spits. Spectroscopic Evidence of Ge Pol HPHT-Treated Natural Type IIa Diamonds. *Gems & Gemology*, 36:42 – 49, 2000.

[180] T. Gu and W. Wang. Optical defects in milky type IaB diamonds. *Diamond and Related Materials*, 89(September):322–329, 2018. ISSN 09259635. doi: 10.

1016/j.diamond.2018.09.010. URL https://doi.org/10.1016/j.diamond.2018.09.010.

[181] A. Shareef, A.T. Collins, and D. Fisher. The 536 and 576 nm centres in diamond. In *56th Diamond Conference Abstract*, 2005. ISBN 9783642253874.

[182] G. Davies, M.H. Nazare, and M.F. Hamer. H3 (2.463 eV) Vibronic Band in diamond: Uniaxial Stress Effects and the Breakdown of Mirror Symmetry. *Proc R Soc London Ser A*, 351(1665):245–265, 1976. doi: 10.1098/rspa.1976.0140.

[183] K. Iakoubovskii, I. Kiflawi, K. Johnston, A. Collins, G. Davies, and A. Stesmans. Annealing of vacancies and interstitials in diamond. *Physica B: Condensed Matter*, 340-342:67–75, 2003. ISSN 09214526. doi: 10.1016/j.physb.2003.09.005.

[184] K.V. Smit, U.F.S. D'Haenens-Johansson, D. Howell, Lorne C. Loudin, and W. Wang. Deformation-related spectroscopic features in natural Type Ib-IaA diamonds from Zimmi (West African craton). *Mineralogy and Petrology*, 112:243–257, 2018. ISSN 09300708. doi: 10.1007/s00710-018-0587-6.

[185] S.J. Pennycook, L.M. Brown, and A.J. Craven. Observation of cathodoluminescence at single dislocations by STEM. *Philosophical Magazine A: Physics of Condensed Matter, Structure, Defects and Mechanical Properties*, 41(4):589–600, 1980. ISSN 01418610. doi: 10.1080/01418618008239335.

[186] D. Takeuchi, H. Watanabe, H. Sawada, S. Yamanaka, H. Ichinose, T. Sekiguchi, and H. Okushi. Origin of band-A emission in homoepitaxial diamond films. *Diamond and Related Materials*, 10(3-7):526–530, 2001. ISSN 09259635. doi: 10.1016/S0925-9635(00)00491-X.

[187] N. Yamamoto, J.C.H. Spence, and D. Fathy. Cathodoluminescence and polarization studies from individual dislocations in diamond. *Philosophical Magazine B: Physics of Condensed Matter; Statistical Mechanics, Electronic, Optical and Magnetic Properties*, 49(6):609–629, 1984. ISSN 13642812. doi: 10.1080/13642818408227648.

[188] J.F. Prins. Increased band A cathodoluminescence after carbon ion implantation and annealing of diamond. *Diamond and Related Materials*, 5(9):907–913, 1996. ISSN 09259635. doi: 10.1016/0925-9635(95)00508-0.

[189] F.H.J. Laidlaw, R. Beanland, D. Fisher, and P.L. Diggle. Point defects and interstitial climb of 90° partial dislocations in brown type IIa natural diamond. *Acta Materialia*, 201:494–503, 2020. ISSN 13596454. doi: 10.1016/j.actamat.2020.10.033. URL https://doi.org/10.1016/j.actamat.2020.10.033.

[190] S.J. Cobb, Z.J. Ayres, and J.V. Macpherson. Boron Doped Diamond: A Designer Electrode Material for the Twenty-First Century. *Annual Review of Analytical Chemistry*, 11(1):463–484, 2018. ISSN 1936-1327. doi: 10.1146/annurev-anchem-061417-010107.

[191] N. Yang, S. Yu, J.V. Macpherson, Y. Einaga, H. Zhao, G. Zhao, G.M. Swain, and X. Jiang. Conductive diamond: synthesis, properties, and electrochemical applications. *Chemical Society Reviews*, 48(1):157–204, 2019. doi: 10.1039/c7cs00757d.

[192] Z.J. Ayres, S.J. Cobb, M.E. Newton, and J.V. Macpherson. Quinone electrochemistry for the comparative assessment of sp^2 surface content of boron doped diamond electrodes. *Electrochemistry Communications*, 72:59–63, 2016. ISSN 1388-2481. doi: 10.1016/j.elecom.2016.08.024.

[193] T.L. Read, S.J. Cobb, and J.V. Macpherson. An sp^2 Patterned Boron Doped Diamond Electrode for the Simultaneous Detection of Dissolved Oxygen and pH. *ACS Sensors*, 4:756–763, 2019. ISSN 23793694. doi: 10.1021/acssensors.9b00137.

[194] S. Garcia-Segura, E. Vieira dos Santos, and C.A. Martínez-Huitle. Role of sp^3/sp^2 ratio on the electrocatalytic properties of boron-doped diamond electrodes : A mini review. *Electrochemistry Communications*, 59:52–55, 2015. ISSN 1388-2481. doi: 10.1016/j.elecom.2015.07.002. URL http://dx.doi.org/10.1016/j.elecom.2015.07.002.

[195] Z.J. Ayres, A.J. Borrill, J.C. Newland, M.E. Newton, and J.V. Macpherson. Controlled sp^2 Functionalization of Boron Doped Diamond as a Route for the Fabrication of Robust and Nernstian pH Electrodes. *Analytical Chemistry*, 88 (1):974–980, 2016. ISSN 15206882. doi: 10.1021/acs.analchem.5b03732.

[196] S.J Cobb, Z.J Ayres, M.E Newton, and J.V Macpherson. Deconvoluting Surface-Bound Quinone Proton Coupled Electron Transfer in Unbuffered Solutions: Toward a Universal Voltammmetric pH Electrode. *Journal of the American Chemical Society*, 141:1035–1044, 2019. doi: 10.1021/jacs.8b11518.

[197] N. El-Najjar, H. Gali-Muhtasib, R.A. Ketola, P. Vuorela, A. Urtti, and H. Vuorela. The chemical and biological activities of quinones: Overview and implications in analytical detection. *Phytochemistry Reviews*, 10(3):353–370, 2011. ISSN 1572980X. doi: 10.1007/s11101-011-9209-1.

[198] L.A. Hutton, M.E. Newton, P.R.. Unwin, and J.V. Macpherson. Factors Controlling Stripping Voltammetry of Lead at Polycrystalline Boron Doped Diamond Electrodes: New Insights from High-Resolution Microscopy. *Analytical Chemistry*, 83(3):735–745, 2011. ISSN 0003-2700. doi: 10.1021/ac101626s.

[199] L. Hutton, M.E. Newton, P.R. Unwin, and J.V. Macpherson. Amperometric oxygen sensor based on a platinum nanoparticle-modified polycrystalline boron doped diamond disk electrode. *Analytical Chemistry*, 81(3):1023–1032, 2009. ISSN 00032700. doi: 10.1021/ac8020906.

[200] M. Pagels, C.E. Hall, N.S. Lawrence, A. Meredith, T.G.J. Jones, H.P. Godfried, C.S.J. Pickles, J. Wilman, C.E. Banks, R.G. Compton, and L. Jiang. All-diamond microelectrode array device. *Analytical Chemistry*, 77(11):3705–3708, 2005. ISSN 0003-2700. doi: 10.1021/ac0502100.

[201] C. Batchelor-McAuley, C.E. Banks, A.O. Simm, T.G.J. Jones, and R.G. Compton. The electroanalytical detection of hydrazine: A comparison of the use of palladium nanoparticles supported on boron-doped diamond and palladium plated BDD microdisc array. *The Analyst*, 131(1):106–110, 2006. ISSN 0003-2654. doi: 10.1039/B513751A.

[202] P.W. Butler-Smith, D.A. Axinte, M. Pacella, and M.W. Fay. Micro/nanometric investigations of the effects of laser ablation in the generation of micro-tools from solid CVD diamond structures. *Journal of Materials Processing Technology*, 213(2):194–200, 2013. ISSN 09240136. doi: 10.1016/j.jmatprotec.2012.08.010.

[203] K. Arihara, C. Terashima, and A. Fujishima. Electrochemical Production of High-Concentration Ozone-Water Using Freestanding Perforated Diamond Electrodes. *Journal of The Electrochemical Society*, 154(4):E71, 2007. ISSN 00134651. doi: 10.1149/1.2509385.

[204] R. Hoffmann, A. Kriele, H. Obloh, J. Hees, M. Wolfer, W. Smirnov, N. Yang, and C.E. Nebel. Electrochemical hydrogen termination of boron-doped diamond. *Applied Physics Letters*, 97(5), 2010. ISSN 0003-6951. doi: 10.1063/1.3476346.

[205] S. Odake, H. Ohfuji, T. Okuchi, H. Kagi, H. Sumiya, and T. Irifune. Pulsed laser processing of nano-polycrystalline diamond: A comparative study with single crystal diamond. *Diamond and Related Materials*, 18(5-8):877–880, 2009. ISSN 09259635. doi: 10.1016/j.diamond.2008.10.066. URL `http://dx.doi.org/10.1016/j.diamond.2008.10.066`.

[206] T. Okuchi, H. Ohfuji, S. Odake, H. Kagi, S. Nagatomo, M. Sugata, and H. Sumiya. Micromachining and surface processing of the super-hard nano-polycrystalline diamond by three types of pulsed lasers. *Applied Physics a-Materials Science & Processing*, 96(4):833–842, 2009. ISSN 0947-8396. doi: 10.1007/s00339-009-5326-8.

[207] H. Ohfuji, T. Okuchi, S. Odake, H. Kagi, H. Sumiya, and T. Irifune. Micro- / nanostructural investigation of laser-cut surfaces of single- and polycrystalline diamonds. *Diamond & Related Materials*, 19(7-9):1040–1051, 2010. ISSN 0925-9635. doi: 10.1016/j.diamond.2010.02.015. URL `http://dx.doi.org/10.1016/j.diamond.2010.02.015`.

[208] S.K. Sudheer, B. Kakadia, V.P. Mahadevan Pillai, G.A. Shafeev, and A.V. Simakin. Processing of natural diamond using nanosecond and picosecond lasers : relative merits and demerits. *Conference on Commercial and Biomedical Applications of Ultrafast Lasers VIII*, 6881, 2008. doi: 10.1117/12.786994.

[209] T.V. Kononenko, V.G. Ralchenko, I.I. Vlasov, S.V. Garnov, V.I. Konov, and I.I. Vlasov. Ablation of CVD diamond with nanosecond laser pulses of UV-IR range. *Diamond and Related Materials*, 7(11-12):1623–1627, 1998. ISSN 0925-9635. doi: 10.1016/s0925-9635(98)00198-8.

[210] S. Gloor, W. Luthy, H.P. Weber, S.M. Pimenov, V.G. Ralchenko, V.I. Konov, and A.V. Khomich. UV laser polishing of thick diamond films for IR windows. *Applied Surface Science*, 138:135–139, 1999. ISSN 0169-4332. doi: 10.1016/s0169-4332(98)00493-0.

[211] E. Cappelli, G. Mattei, S. Orlando, F. Pinzari, and P. Ascarelli. Pulsed laser surface modifications of diamond thin films. *Diamond and Related Materials*, 8(2-5):257–261, 1999. ISSN 0925-9635. doi: 10.1016/s0925-9635(98)00401-4.

[212] J. Li, C.L. Bentley, S. Tan, V.S.S. Mosali, A. Rahman, S.J. Cobb, S. Guo, J.V. Macpherson, P.R. Unwin, A.M. Bond, and J. Zhang. Impact of sp^2 Carbon Edge Effects on the Electron-Transfer Kinetics of the Ferrocene/Ferricenium

Process at a Boron-Doped Diamond Electrode in an Ionic Liquid. *Journal of Physical Chemistry C*, 123:17397–17406, 2019. doi: 10.1021/acs.jpcc.9b04519.

[213] S. Preuss and M. Stuke. Subpicosecond Ultraviolet-Laser Ablation of Diamond - Nonlinear Properties at 248 Nm and Time-Resolved Characterization of Ablation Dynamics. *Applied Physics Letters*, 67(3):338–340, 1995. ISSN 00036951. doi: Doi10.1063/1.115437.

[214] D. Ramanathan and P.a. Molian. Micro- and sub-micromachining of type IIa single crystal diamond using a Ti : Sapphire femtosecond laser. *Journal of Manufacturing Science and Engineering-Transactions of the Asme*, 124(2): 389–396, 2002. ISSN 10871357. doi: 10.1115/1.1459083.

[215] M. Shinoda, R.R. Gattass, and E. Mazur. Femtosecond laser-induced formation of nanometer-width grooves on synthetic single-crystal diamond surfaces. *Journal of Applied Physics*, 105(5):053102, 2009. ISSN 00218979. doi: 10.1063/1.3079512.

[216] S. Su, J. Li, G.C.B. Lee, K. Sugden, D. Webb, and H. Ye. Femtosecond laser-induced microstructures on diamond for microfluidic sensing device applications sensing device applications. *Applied Physics Letters*, 102(23):231913, 2013. doi: 10.1063/1.4811170.

[217] V.V. Kononenko, T.V. Kononenko, S.M. Pimenov, M.N. Sinyavskii, V.I. Konov, and F. Dausinger. Effect of the pulse duration on graphitisation of diamond during laser ablation Effect of the pulse duration on graphitisation of diamond during laser ablation. *Quantum Electronics*, 35(3):252–256, 2005. doi: 10.1070/QE2005v035n03ABEH002900.

[218] M. Wu, B. Guo, Q. Zhao, P. He, Z. Zeng, and J. Zang. The influence of the ionization regime on femtosecond laser beam machining mono-crystalline diamond. *Optics and Laser Technology*, 106:34–39, 2018. ISSN 00303992. doi: 10.1016/j.optlastec.2018.03.031.

[219] S. Osswald, G. Yushin, V. Mochalin, S.O. Kucheyev, and Y. Gogotsi. Control of sp^2/sp^3 carbon ratio and surface chemistry of nanodiamond powders by selective oxidation in air. *Journal of the American Chemical Society*, 128(35): 11635–11642, 2006. ISSN 0002-7863. doi: 10.1021/ja063303n.

[220] A. Krueger and D. Lang. Functionality is key: Recent progress in the surface modification of nanodiamond. *Advanced Functional Materials*, 22(5):890–906, 2012. ISSN 1616301X. doi: 10.1002/adfm.201102670.

[221] A.J. Lucio, R.E.P. Meyler, M.A. Edwards, and J.V. Macpherson. Investigation of sp^2 Carbon Pattern Geometry in Boron-Doped Diamond Electrodes for the Electrochemical Quantification of Hypochlorite at High Concentrations. *ACS Sensors*, 5(3):789 – 797, 2020. doi: 10.1021/acssensors.9b02444.

[222] H. Kozak, A. Kromka, E. Ukraintsev, J. Houdkova, M. Ledinsky, M. Vaněček, and B. Rezek. Detecting sp^2 phase on diamond surfaces by atomic force microscopy phase imaging and its effects on surface conductivity. *Diamond and Related Materials*, 18(5-8):722–725, 2009. ISSN 09259635. doi: 10.1016/j.diamond.2009.02.010.

[223] A. Stacey, V.S. Drumm, B.A. Fairchild, K. Ganesan, S. Rubanov, R. Kalish, B.C.C. Cowie, S. Prawer, and A. Hoffman. Improved diamond surfaces following lift-off and plasma treatments as observed by X-ray absorption spectroscopy. *Applied Physics Letters*, 98(18):1–4, 2011. ISSN 00036951. doi: 10.1063/1.3585106.

[224] J.Y. Shim and H.K. Baik. Effect of non-diamond carbon etching on the field emission property of highly sp^2 nanocrystalline diamond films. *Diamond and Related Materials*, 10(3-7):847–851, 2001. ISSN 09259635. doi: 10.1016/S0925-9635(01)00378-8.

[225] A. Stacey, N. Dontschuk, J.P. Chou, D.A. Broadway, A.K. Schenk, M.J. Sear, J.P. Tetienne, A. Hoffman, S. Prawer, C.I. Pakes, A. Tadich, N.P. de Leon, A. Gali, and L.C.L. Hollenberg. Evidence for Primal sp^2 Defects at the Diamond Surface: Candidates for Electron Trapping and Noise Sources. *Advanced Materials Interfaces*, 6(3):1–8, 2019. ISSN 21967350. doi: 10.1002/admi.201801449.

[226] S.J. Cobb, F.H.J. Laidlaw, G. West, G. Wood, M.E. Newton, R. Beanland, and J.V. Macpherson. Assessment of acid and thermal oxidation treatments for removing sp^2 bonded carbon from the surface of boron doped diamond. *Carbon*, 167:1–10, 2020. ISSN 0008-6223. doi: 10.1016/j.carbon.2020.04.095. URL `https://doi.org/10.1016/j.carbon.2020.04.095`.

[227] L.A. Hutton, J.G. Iacobini, E. Bitziou, R.B. Channon, M.E. Newton, and J.V. Macpherson. Examination of the factors affecting the electrochemical performance of oxygen-terminated polycrystalline boron-doped diamond electrodes. *Analytical Chemistry*, 85(15):7230–7240, 2013. ISSN 00032700. doi: 10.1021/ac401042t.

[228] R.M. Langford, T.X. Wang, and D. Ozkaya. Reducing the resistivity of electron and ion beam assisted deposited Pt. *Microelectronic Engineering*, 84(5-8): 784–788, 2007. ISSN 01679317. doi: 10.1016/j.mee.2007.01.055.

[229] A.J. Papworth, C.J. Kiely, A.P. Burden, S.R.P. Silva, and G.A.J. Amaratunga. Electron-energy-loss spectroscopy characterization of the sp^2 bonding fraction within carbon thin films. *Physical Review B - Condensed Matter and Materials Physics*, 62(19):12628–12631, 2000. ISSN 01631829. doi: 10.1103/PhysRevB.62.12628.

[230] Y. Gotoh. Interlayer structure changes of graphite after hydrogen ion irradiation. *Journal of Nuclear Materials*, 248:46–51, 1997. ISSN 00223115. doi: 10.1016/S0022-3115(97)00115-3.

[231] J. Bruley, D.B. Williams, J.J. Cuomo, and D.P. Pappas. Quantitative nearedge structure analysis of diamondlike carbon in the electron microscope using a twowindow method. *Journal of Microscopy*, 180(1):22–32, 1995. ISSN 13652818. doi: 10.1111/j.1365-2818.1995.tb03653.x.

[232] W. Zhu, X.H. Wang, D.J. Pickrell, A.R. Badzian, and R. Messier. The Oxidation of CVD Dlamond Films. *Carbon*, 28(6):796, 1990. doi: https://doi.org/10.1016/0008-6223(90)90302-F.

[233] A.A. Zavitsas. The relation between bond lengths and dissociation energies of carbon-carbon bonds. *Journal of Physical Chemistry A*, 107(6):897–898, 2003. ISSN 10895639. doi: 10.1021/jp0269367.

[234] Sh. Michaelson, R. Akhvlediani, and A. Hoffman. Hydrogen bonding configuration and thermal stability of ambient exposed and in situ hydrogenated polycrystalline diamond surfaces studied by high resolution electron energy loss spectroscopy. *Physical Chemistry Chemical Physics*, 13(24):11471–11480, 2011. ISSN 14639076. doi: 10.1039/c1cp00019e.

[235] K.A.H. Al Mahmud, M.A. Kalam, H.H. Masjuki, H.M. Mobarak, and N.W.M. Zulkifli. An updated overview of diamond-like carbon coating in tribology. *Critical Reviews in Solid State and Materials Sciences*, 40(2):90–118, 2015. ISSN 15476561. doi: 10.1080/10408436.2014.940441.